

BOSTON UNIVERSITY  
COLLEGE OF ENGINEERING

Dissertation

**WIDE-FIELD OPTICAL IMAGING OF NEUROVASCULAR COUPLING  
DURING STROKE RECOVERY**

by

**SMRITHI SUNIL**

B.S., Case Western Reserve University, 2015  
M.S., Boston University, 2018

Submitted in partial fulfillment of the  
requirements for the degree of  
Doctor of philosophy

2021

© 2021 by  
SMRITHI SUNIL  
All rights reserved

Approved by

First Reader

---

David A. Boas, Ph.D.  
Professor of Biomedical Engineering  
Professor of Electrical and Computer Engineering

Second Reader

---

Anna Devor, Ph.D.  
Associate Professor of Biomedical Engineering

Third Reader

---

Xue Han, Ph.D.  
Associate Professor of Biomedical Engineering

Fourth Reader

---

Darren Roblyer, Ph.D.  
Associate Professor of Biomedical Engineering  
Associate Professor of Electrical and Computer Engineering

Fifth Reader

---

Cenk Ayata, M.D.  
Professor of Neurology  
Massachusetts General Hospital

## **DEDICATION**

I dedicate this work to my husband, Gavin Brown, for his unwavering support,  
and to my parents for their love and encouragement.

## **ACKNOWLEDGMENTS**

My time spent working on this dissertation has been some of the best years of my life that were filled with intellectual and personal growth. It is with great pleasure that I acknowledge all the people that made this exciting journey possible and enjoyable.

First, I would like to thank my family for their constant encouragement and belief in my ability to accomplish anything I set my mind to. Thank you to my incredible husband Gavin Brown for his constant support through my academic journey and well beyond, and for always knowing how to make me laugh. To my parents, Sheetal Bachegowda and Sunil Subbiah, for instilling in me at an early age the importance of education and always encouraging me to pursue my independent ambitions. Thank you to my sister Srishti Sunil for always having my back and reminding me that no accomplishment is too small. To my uncles, Sharath Bachegowda and Arjun Narayan for paving the way and showing me that there is nothing beyond my reach. Thank you to all my family, near and far, for all their love that continues to inspire me every day.

Next, I would like to thank my PhD advisor David Boas who gave me the opportunity to work on a project that I truly loved and one that continually fueled my scientific curiosity. His critical thinking, questioning, and eloquent ability to state complex problems with ease, constantly inspires me. David's confidence in my abilities has gone a long way in shaping my scientific growth, and I have no doubt that the knowledge I have learned from him will stay with me through my scientific career. I would like to thank my dissertation committee member Anna Devor, for the wonderful discussions and the unique

excitement she brought to the table, my other committee members, Cenk Ayata, Xue Han, and Darren Roblyer, for their time, guidance, and encouragement throughout the PhD. I would also like to thank my first PhD advisor Jason Ritt for constantly challenging my thought process and developing my scientific framework upon which everything else has been built. Thank you to the entire BME department faculty and administration for making the six years I spent at BU enjoyable.

I would also like to thank the members of the BOAS Lab, from whom I have learned a great deal about neuroscience, imaging, and life in general. Specifically, Evren Erdener, Jianbo Tang, Dmitry Postnov, Xiaojun Cheng, Anderson Chen, Kivilcim Kilic, Parya Farzam, and Bernhard Zimmermann who were always there to help with advice, guidance, training, and troubleshooting. My undergraduate mentees, Shashwat Shah and Lesbeth Roque, who worked with me patiently on experiments and data analysis. John Jiang for all the animal surgeries, without which this dissertation would not have been possible. My fellow PhD mates Jack Giblin, Antonio Ortega, Jiarui Yang, Sharvari Zilpelwar, Stephan Chang, and Bingxue Liu for all the wonderful times spent in the lab. Finally, I would like to thank Sreekanth Kura and Blaire Lee for not only being incredible lab mates and a constant source of support but also for forming true friendships that I will cherish forever.

I would like to thank all the members of my PhD starting cohort with whom spending a year in the same room during this important time led to lifetime friendships. I thank you all for expressing your love for science, which reminded me every day why I love science, and for all your support through important milestones, both academic and personal.

I would also like to take this time to thank a few other people who have played an important role in my academic journey. My undergraduate research advisor Jeffrey Capadona and mentor Madhumitha Ravikumar, who allowed me to explore my early research interests. It was because of them that I fell in love with the brain and hope to spend my life exploring its marvels. My high school Physics teacher Mr. Ram and math teacher Mrs. Shivaram for sparking my interest in science. To them and all my other teachers, mentors, and cheerleaders throughout life who not only had confidence in my abilities but also showed it, I owe my career to you all.

**WIDE-FIELD OPTICAL IMAGING OF NEUROVASCULAR COUPLING  
DURING STROKE RECOVERY**

**SMRITHI SUNIL**

Boston University College of Engineering, 2021

Major Professor: David A. Boas, Ph.D., Professor of Biomedical Engineering,  
Professor of Electrical and Computer Engineering

**ABSTRACT**

Functional neuroimaging, which measure vascular responses to brain activity, are invaluable tools for monitoring and treating stroke patients both in the acute and chronic phases of recovery. However, vascular responses after stroke are almost always altered relative to vascular responses in healthy subjects and it is still unclear if these alterations reflect the underlying brain physiology or if the alterations are purely due to vascular injury. In other words, we do not know the effect of stroke on neurovascular coupling and are therefore limited in our ability to use functional neuroimaging to accurately interpret stroke pathophysiology. There is a need for animal models to investigate the effect of stroke on neurovascular coupling to aid in better interpreting the results from functional neuroimaging.

To that end, we first implemented a mouse photothrombotic stroke model that mimics the physiology of a human stroke and therefore has high clinical relevance. Mice were implanted with bilateral cranial windows to allow long term multimodal optical access. The occlusion procedure was performed in awake animals while simultaneously monitoring changes to cerebral blood flow. Our optimized photothrombotic stroke to the somatosensory forelimb region produced a sustained behavioral deficit in the contralateral

forelimb that could be monitored longitudinally. Next, we implemented simultaneous imaging of neuronal activity, through fluorescent calcium imaging, and hemodynamics, through intrinsic optical signal imaging, to investigate neurovascular coupling during stroke recovery. Additionally, we identified a novel use for spatial frequency domain imaging to quantify the spatial extent of the stroke core.

Finally, we combined the mouse stroke model and imaging platforms to investigate the effect of stroke on neurovascular coupling. We found that acute stroke led to the abolishment of both calcium and hemodynamic responses to sensory stimulation. This elimination of response was associated with a loss of correlation between calcium and hemodynamic activity in the acute phase. To quantify neurovascular coupling, we modeled spatiotemporal hemodynamics by convolving neural activity and hemodynamic response functions obtained from deconvolution. Hemodynamic response functions from healthy animals were unable to model hemodynamics in the acute phase, suggesting neurovascular uncoupling. However, hemodynamics could be modeled in the chronic phase, indicating chronic recoupling. Acute stroke also resulted in increased global brain oscillations, which showed distinct patterns in calcium and hemodynamics, and the increase in contralesional calcium activity was associated with increased functional connectivity. We also show that early return of responses, neurovascular recoupling, and global oscillations were predictors of improved behavioral outcomes.

## TABLE OF CONTENTS

DEDICATION .....	iv
ACKNOWLEDGMENTS .....	v
ABSTRACT .....	viii
TABLE OF CONTENTS.....	x
LIST OF TABLES .....	xiv
LIST OF FIGURES .....	xv
LIST OF ABBREVIATIONS.....	xviii
CHAPTER ONE – BACKGROUND .....	1
1.1    Importance of studying neurovascular recovery following stroke .....	2
1.2    Cortical reorganization after stroke .....	4
1.3    Neurovascular coupling mechanisms .....	7
1.4    Preclinical stroke models .....	11
1.5    Research overview .....	13
CHAPTER TWO – AWAKE CHRONIC MOUSE MODEL OF TARGETED PIAL VESSEL OCCLUSION VIA PHOTOTHROMBOSIS .....	15
2.1    Abstract .....	15
2.2    Introduction.....	16
2.3    Methods.....	18
2.4    Results.....	29
2.4.1    A 6 $\mu$ m spot is superior to a 30 $\mu$ m spot in preventing capillary damage as shown by Monte Carlo simulations .....	29

2.4.2	Optimized and non-optimized methods produce an ischemic stroke .....	32
2.4.3	The optimized method prevents capillary thrombosis .....	35
2.4.4	Formation of a stable infarct was confirmed using blood flow changes, histological validation, and behavioral analysis .....	39
2.4.5	The chronic use of our model was validated using longitudinal imaging of vasculature .....	40
2.5	Discussion .....	42
2.6	Supplementary material .....	46
<b>CHAPTER THREE – STROKE CORE REVEALED BY TISSUE SCATTERING</b>		
<b>USING SPATIAL FREQUENCY DOMAIN IMAGING.....</b>		<b>49</b>
3.1	Abstract .....	49
3.2	Introduction .....	50
3.3	Methods.....	53
3.4	Results.....	64
3.4.1	Increased OCT signal attenuation in a mouse photothrombosis stroke model is a reliable predictor of the stroke core .....	64
3.4.2	Reduced scattering coefficient obtained from SFDI reliably predicts increased signal attenuation seen with OCT following stroke.....	65
3.4.3	Scattering increase as determined from SFDI following photothrombotic stroke is a reliable predictor of the stroke core .....	67
3.5	Discussion .....	68

CHAPTER FOUR – SIMULTANEOUS WIDE-FIELD OPTICAL IMAGING OF NEURAL ACTIVITY AND HEMODYNAMICS DURING STROKE RECOVERY ...	74
4.1 Abstract .....	74
4.2 Introduction.....	75
4.3 Methods.....	78
4.4 Results.....	84
4.4.1 Fluorescence correction for hemodynamic crosstalk is needed for accurate estimation of GCaMP dynamics .....	84
4.4.2 Fluorescence correction for hemodynamic crosstalk with the ratiometric method underestimates the correction .....	87
4.4.3 Attenuation estimation correction more accurately corrects for hemodynamic crosstalk when appropriate pathlength factors are considered .....	89
4.4.4 Stroke leads to changes in tissue optical properties that can be accounted for in the correction algorithm.....	93
4.5 Discussion .....	95
CHAPTER 5 – TARGETED PHOTOTHROMBOTIC STROKE DISRUPTS NEUROVASCULAR COUPLING .....	100
5.1 Abstract .....	100
5.2 Introduction.....	101
5.3 Methods.....	103
5.4 Results.....	113

5.4.1	Wide-field fluorescence and intrinsic signal imaging can follow changes to calcium and hemodynamic activity after stroke .....	113
5.4.2	Acute stroke alters the correlation between evoked calcium and hemodynamic responses .....	117
5.4.3	Acute stroke leads to neurovascular uncoupling within the peri-infarct that is restored in the chronic phase.....	120
5.4.4	Acute stroke leads to increases in global brain oscillation power .....	127
5.4.5	Photothrombotic stroke disrupts resting state interhemispheric functional connectivity only in the early acute phase .....	131
5.4.6	Correlating cortical metrics to long-term behavior outcomes .....	135
5.5	Discussion .....	138
5.6	Supplementary material .....	146
	CHAPTER SIX – CONCLUSIONS AND FUTURE DIRECTIONS .....	153
6.1	Summary of dissertation .....	153
6.2	Significance for pre-clinical research and clinical translation .....	155
6.3	Future directions .....	159
	BIBLIOGRAPHY .....	162
	CURRICULUM VITAE .....	180

## **LIST OF TABLES**

Table 2. 1: Supplementary table with list of parts for IOSI, LSCI, and photothrombosis system .....	47
---	----

## LIST OF FIGURES

Figure 1. 1: Cortical reorganization after stroke .....	7
Figure 1. 2: Summary of the proposed mechanisms involved in regulation of cortical microvessels by excitatory pyramidal cells, inhibitory interneurons, and astrocytes .	9
Figure 2. 1: Photothrombosis instrumentation and animal preparation.....	20
Figure 2. 2: Tissue damage with a 30 $\mu\text{m}$ and 6 $\mu\text{m}$ spot size .....	31
Figure 2. 3: Relative cerebral blood flow maps during photothrombosis.....	35
Figure 2. 4: Capillary damage with non-optimized and optimized photothrombosis.....	37
Figure 2. 5: Vessel segmentation and quantification of capillary damage .....	38
Figure 2. 6: Validation of stable infarct obtained with optimized photothrombosis .....	40
Figure 2. 7: Longitudinal multi-modal optical imaging after stroke .....	41
Figure 2. 8: Rose Bengal decay imaged using two-photon microscopy.....	46
Figure 3. 1: Schematic of the imaging setup with combined photothrombosis, laser speckle contrast imaging, and spatial frequency domain imaging.....	55
Figure 3. 2: OCT analysis for signal attenuation .....	58
Figure 3. 3: SFDI instrumentation schematic and analysis pipeline.....	61
Figure 3. 4: Spatial overlap of OCT attenuation and TTC staining .....	64
Figure 3. 5: Signal attenuation comparison between SFDI and OCT.....	66
Figure 3. 6: Dice similarity coefficient workflow and calculation for stroke overlap.....	67
Figure 3. 7: SFDI spatial overlap with TTC staining.....	68

Figure 4. 1: Hemodynamic contamination of fluorescence data .....	86
Figure 4. 2: Fluorescence correction for hemodynamic crosstalk with ratiometric method .....	88
Figure 4. 3: Effect of pathlength on attenuation correction .....	91
Figure 4. 4: Attenuation correction applied with pathlengths obtained from SFDI absorption and scattering .....	92
Figure 4. 5: Accounting changes in tissue optical properties after stroke in the correction algorithm .....	94
Figure 5. 1: Simultaneous calcium and hemodynamic imaging post-stroke .....	116
Figure 5. 2: Correlation between evoked calcium and hemodynamic responses .....	119
Figure 5. 3: Neurovascular coupling with linear least-squares deconvolution .....	123
Figure 5. 4: Ability of the hemodynamic response function (HRF) to predict hemodynamics .....	126
Figure 5. 5: Global brain oscillations following stroke .....	130
Figure 5. 6: Global brain network dynamics assessed with RSFC .....	134
Figure 5. 7: Correlating cortical metrics to behavior outcomes.....	138
Figure 5. 8: Fluorescence correction for hemodynamic crosstalk .....	146
Figure 5. 9: Responses in the affected hemisphere normalized to pre-stroke .....	147
Figure 5. 10: Spatial maps of GCaMP and hemodynamic responses over time during sensory stimulation .....	148

Figure 5. 11: Correlation of calcium and hemodynamic evoked responses to sensory stimulation of the affected forelimb color-coded by mouse .....	149
Figure 5. 12: Responses within the unaffected hemisphere during stimulation of the unaffected forelimb .....	150
Figure 5. 13: Pearson's correlation coefficient of neurovascular coupling in healthy pre-stroke animals during sessions with evoked responses and resting-state sessions .	151
Figure 5. 14: RSFC proportional area and dice coefficient analysis at threshold of 0.4	152

## LIST OF ABBREVIATIONS

ADC.....	apparent diffusion coefficient
BOLD fMRI.....	blood-oxygen-level-dependent functional magnetic resonance imaging
CBF.....	cerebral blood flow
CMOS.....	complementary metal-oxide-semiconductor
COX-2.....	cyclooxygenase-2
DMD.....	digital micromirror device
DNA.....	deoxyribonucleic acid
DWI.....	diffusion weighted imaging
EEG.....	electroencephalography
fc-MRI.....	functional connectivity magnetic resonance imaging
FITC.....	fluorescein isothiocyanate
fMRI.....	functional magnetic resonance imaging
fnIRS.....	functional near-infrared spectroscopy
GABA.....	gamma aminobutyric acid
GFP.....	green fluorescent protein
HbO.....	oxy-hemoglobin
HbR.....	deoxy-hemoglobin
HbT.....	total hemoglobin
HRF.....	hemodynamic response function
IOSI.....	intrinsic optical signal imaging
IP.....	intraperitoneal

LED.....	light emitting diode
LSCI.....	laser speckle contrast imaging
LUT.....	lookup table
MCA.....	middle cerebral artery
MCAO.....	middle cerebral artery occlusion
MEG.....	magnetoencephalography
MTF.....	modulation transfer function
NA.....	numerical aperture
NO.....	nitric oxide
NVC.....	neurovascular coupling
OCT.....	optical coherence tomography
OD.....	optical density
PBS.....	phosphate-buffered saline
PET.....	positron emission tomography
PFA.....	paraformaldehyde
PGE2.....	prostaglandin E <sub>2</sub>
PI.....	propidium iodide
RSFC.....	resting-state functional connectivity
SFDI.....	spatial frequency domain imaging
TTC.....	triphenyl tetrazolium chloride

## CHAPTER ONE – BACKGROUND

Functional neuroimaging methods are invaluable for managing the treatment of stroke patients both in the acute and chronic phases of recovery<sup>1-4</sup>. At least some degree of spontaneous functional recovery is observed in most patients in the months following stroke and the biological mechanisms responsible for this recovery are under active investigation<sup>4,5</sup>. Neuroimaging studies, such as functional Magnetic Resonance Imaging (fMRI) and functional Near Infrared Spectroscopy (fNIRS), both of which measure the vascular response to brain activity, are not only used to monitor the recovery from stroke but also to understand the mechanisms responsible for recovery<sup>6,7</sup>. However, the vascular responses post-stroke are almost always altered relative to those seen in healthy individuals<sup>8,9</sup>. It is not known if these vascular response alterations are a reflection of the underlying differences in neuronal function or simply a result of injury to the vasculature. In other words, we do not know the effect of stroke on neurovascular coupling and thus are limited in our ability to use these valuable neuroimaging tools to study functional recovery in stroke survivors. Thus, there is a need for preclinical stroke models to evaluate the functional aspects of neurovascular recovery and to use these findings to improve the interpretations of human neuroimaging studies. The work of this dissertation is to develop and implement the tools required to study neurovascular recovery in a preclinical stroke model with high clinical relevance, as well as to use these tools to address changes in neurovascular coupling and functional recovery in the acute and chronic phases post-stroke.

### **1.1 Importance of studying neurovascular recovery following stroke**

Stroke is one of the leading causes of long-term disability worldwide. Every year approximately 800,000 people experience a stroke in the United States alone<sup>10</sup>. The majority of patients survive, and among survivors, work capacity is compromised in over 70% of affected individuals. Strokes can be categorized as either ischemic or hemorrhagic. An ischemic stroke, which accounts for over 85% of all strokes, occurs due to the interruption of blood flow caused by thrombosis or embolism. During ischemia, a reduction or complete loss of blood supply causes a starved oxygen environment and leads to neuronal damage within minutes<sup>11</sup>. As energy dependent processes continue to fail, neuronal damage leads to cell death and ultimately to sensorimotor and cognitive impairments over hours and subsequent days<sup>11–13</sup>. The complex spatial and temporal progression of the compromised area leads to the formation of an ischemic core and a surrounding penumbra in the acute phase after occlusion<sup>14</sup>. While the stroke core consists of tissue that has undergone irreversible damage, the penumbra is comprised of tissue with reduced blood flow that is compromised but not yet dead. Most therapies to enhance recovery post-stroke are targeted at the penumbra as it can be salvaged to regain some lost function<sup>14–17</sup>. Stroke progression is typically classified into two main phases in time, the acute phase, which is hours to a week following stroke, and the chronic phase, which spans weeks and months after stroke. The penumbra is called the peri-infarct in the chronic phase and is the target for longitudinal therapies such as rehabilitation.

A large body of evidence indicates that neural activity is closely related to cerebral blood flow (CBF), both spatially and temporally, and this relationship between neural

activity and CBF is termed neurovascular coupling (NVC)<sup>18–22</sup>. The tight coupling between neuronal activity and blood flow forms the basis of modern neuroimaging techniques that use the cerebrovascular changes caused by neural activation to map changes in function in the behaving human brain. These techniques have provided tremendous insights into the cognitive and sensorimotor functioning of the healthy human brain. NVC has been studied extensively in the healthy brain and continues to be an active area of investigation. However, the effect of stroke on NVC has received limited and sometimes conflicting attention<sup>23</sup>. While NVC is maintained in the healthy brain, pathologies such as traumatic brain injury, Alzheimer's disease, and stroke may lead to disruption in the interaction between neural activity and CBF, thereby confounding the interpretations of neuroimaging results<sup>24,25</sup>.

Nonetheless, spontaneous as well as treatment enhanced recovery following stroke is monitored longitudinally through functional neuroimaging techniques such as blood-oxygen-level-dependent functional Magnetic Resonance Imaging (BOLD fMRI) and functional Near Infrared Spectroscopy (fNIRS)<sup>26–29</sup>. Most stroke patients exhibit some degree of recovery over time, motivating the continued improvement in interventions, both pharmacological and rehabilitative, and the biological mechanisms responsible for recovery are under active investigation. Neuroimaging studies have revealed the remarkable ability of the brain to spontaneously reorganize and recover to some extent following stroke both on a local and global network scale<sup>5,8</sup>. Functional neuroimaging techniques are valuable non-invasive imaging tools for not only monitoring stroke patients during this recovery period but also to understand the mechanisms by which recovery takes

place, which are then used to guide rehabilitative interventions to accelerate recovery. However, fMRI and fNIRS measure the hemodynamic response to neuronal activation, and not neuronal activity directly. It is still unclear if the observed hemodynamic responses are a true reflection of the underlying physiology. While this poses a potential challenge, it also provides the advantage of being able to study how the neurovascular unit recovers after stroke, unlike electroencephalography (EEG) or magnetoencephalography (MEG), which provide information only about neural activity, as both the neural and vascular compartments are affected and both play a crucial role in recovery.

## 1.2 Cortical reorganization after stroke

The brain has the remarkable ability to compensate for structural damage through the reorganization of surviving networks<sup>30,31</sup>. These processes are fundamental for recovery of function for many forms of brain injury, including stroke. Most patients who have experienced a stroke exhibit continued functional recovery over many years following the initial injury and this recovery has been associated with brain plasticity. Evidence from fMRI and positron emission tomography (PET) studies has shown significant alterations in activation patterns during movement of the stroke affected hand in the acute phase, which then return to more physiological patterns in the chronic phase<sup>9</sup>. Specifically, movements of the affected hand in the acute phase were associated with a stronger bilateralization of activity in sensorimotor cortex<sup>26,32</sup>. Additionally, a meta-analysis on activation data from over 50 neuroimaging experiments has shown enhanced activity in the homotopic (symmetric) region of the contralesional hemisphere and is a highly reproduced

finding in the acute phase after stroke<sup>33,34</sup>. Studies associating cortical reorganization with behavior outcomes suggest that a decrease in this contralesional enhanced-activity correlated with better long-term recovery<sup>34–36</sup>. This suggests that successful recovery is associated with a normalization of pathologically enhanced brain activity over time. Moreover, increases in activity early after stroke are indicative of better functional recovery, thereby providing a prognostic marker for long-term recovery<sup>37</sup>.

While external stimuli or task-related studies address local changes to cortical activity, they do not address how connectivity within the entire cortical network has changed. Analyses of global functional connectivity across a wide network of brain regions are typically performed on resting-state fMRI time series, which reflect spontaneous fluctuations of activity in the absence of a structured task<sup>38–41</sup>. Connectivity studies using fMRI activity in the resting-state frequently demonstrated reduced functional connectivity between ipsilesional motor cortex and contralesional motor cortex as a function of motor impairment. Other brain regions also had less functional connectivity with the lesioned motor cortex when compared to healthy controls. Importantly, stronger functional connectivity of ipsilesional M1 with other brain areas in the early subacute phase post-stroke predicts better functional recovery 6 months later.

Animal models of stroke also show a similar pattern of improved cortical and behavioral performance, although the time course of this post-stroke recovery is much shorter. Dijkhuizen et al. showed that unilateral stroke in the forelimb sensorimotor region resulted in acute dysfunction of the contralateral forelimb, which then recovered at later stages<sup>42</sup>. Forelimb impairment in the acute phase was also accompanied by a loss of

stimulus-induced cortical activation, when assessed with fMRI, in the ipsilesional hemisphere while the contralesional hemisphere showed increased stimulus-induced responses. After two weeks, in the chronic phase, the peri-infarct showed significant responses while the contralesional hemisphere showed reduced involvement. A follow up study suggested that the extent of functional recovery is associated with the extent of preservation or restoration of activation in the ipsilesional hemisphere<sup>43</sup>. Other studies using in vivo voltage-sensitive dye imaging or calcium imaging using genetically encoded indicators have also shown that somatosensory activation maps that are lost due to somatosensory stroke are replaced over weeks through new structural and functional circuits within the peri-infarct<sup>44–47</sup>. Resting state functional connectivity (RSFC) studies have also been performed in mice using intrinsic optical signal imaging (IOSI) and have shown a loss in both the inter- and intra-hemispheric connectivity in relation to the lesion site<sup>48,49</sup>. Cortical alteration after stroke is summarized in Figure 1.1.

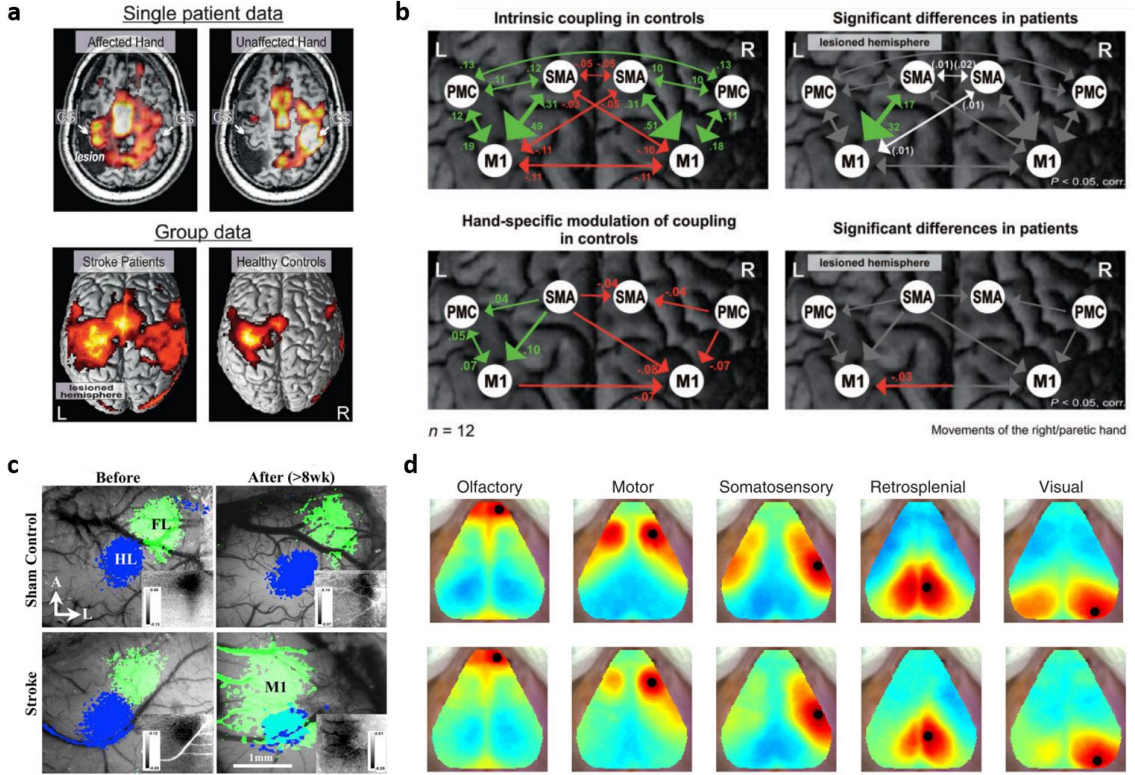


**Figure 1.1: Cortical reorganization after stroke**

(a) Evoked response reorganization. Top: BOLD fMRI of single patient data during movement of the affected and unaffected hands. Bottom: BOLD fMRI of grouped data in stroke and healthy controls. Taken from Grefkes and colleagues<sup>9</sup>. (b) Functional connectivity across different regions in healthy subjects and patients with subcortical stroke. Taken from Grefkes and colleagues<sup>8</sup>. (c) Evoked response reorganization of sensory forelimb region in a mouse photothrombotic stroke model. Taken from Brown and colleagues<sup>45</sup>. (d) Resting state functional connectivity in mice pre and post stroke. Taken from Bauer and colleagues<sup>49</sup>.

### 1.3 Neurovascular coupling mechanisms

The proper functioning of brain activity requires precise regulation of CBF and oxygen supply to meet the demands of neural activity, which is known as neurovascular coupling (NVC)<sup>18–22</sup>. Extensive research on NVC mechanisms over the last few decades has revealed that NVC is regulated by synchronous activity of different cell types including neurons, astrocytes, pericytes, endothelial cells, and smooth muscle cells, all of which

make up the neurovascular unit. Current evidence suggests that there are multiple mechanisms by which changes in neuronal activity are transduced into an integrated vascular response. Activated neurons and astrocytes release a multitude of vasoactive factors that act in unison to regulate CBF. These vasoactive messengers target pericytes, smooth muscle cells, and endothelial cells, which then convert the incoming signal into coordinated vascular adjustments that ultimately lead to an increase in CBF and oxygen.

The proposed mechanisms involved in the regulation of cortical microvessels include the roles of excitatory pyramidal cells, inhibitory interneurons, and astrocytes (Figure 1.2). The cerebral cortical network receives inputs from various sub-cortical regions. These activated networks have two main ways of eliciting a hemodynamic response: 1) they can act directly on the microvasculature<sup>50–52</sup>, which have receptors for vasoactive neurotransmitters and neuromodulators such as COX-2 derivatives (PGE2 and NO) released from pyramidal cells and GABA released from interneurons, and 2) they can act indirectly through astrocytes<sup>53,54</sup>, which are intermediaries to both excitatory and inhibitory neurons. The indirect response is comparatively slower than that of the direct pathway. Studies have shown that no single vasoactive messenger can individually account for the hemodynamic response and when individually summed the response exceeds the expected value of 100%<sup>55–58</sup>. This suggests that vasoactive messengers released by activated neurons and astrocytes do not operate independently from each other, but rather act like modulators in unison to elicit the hemodynamic response, which could depend on the nature of the afferent inputs. This tight coupling between neural activity and hemodynamics forms the basis on which functional neuroimaging studies are interpreted<sup>59</sup>.

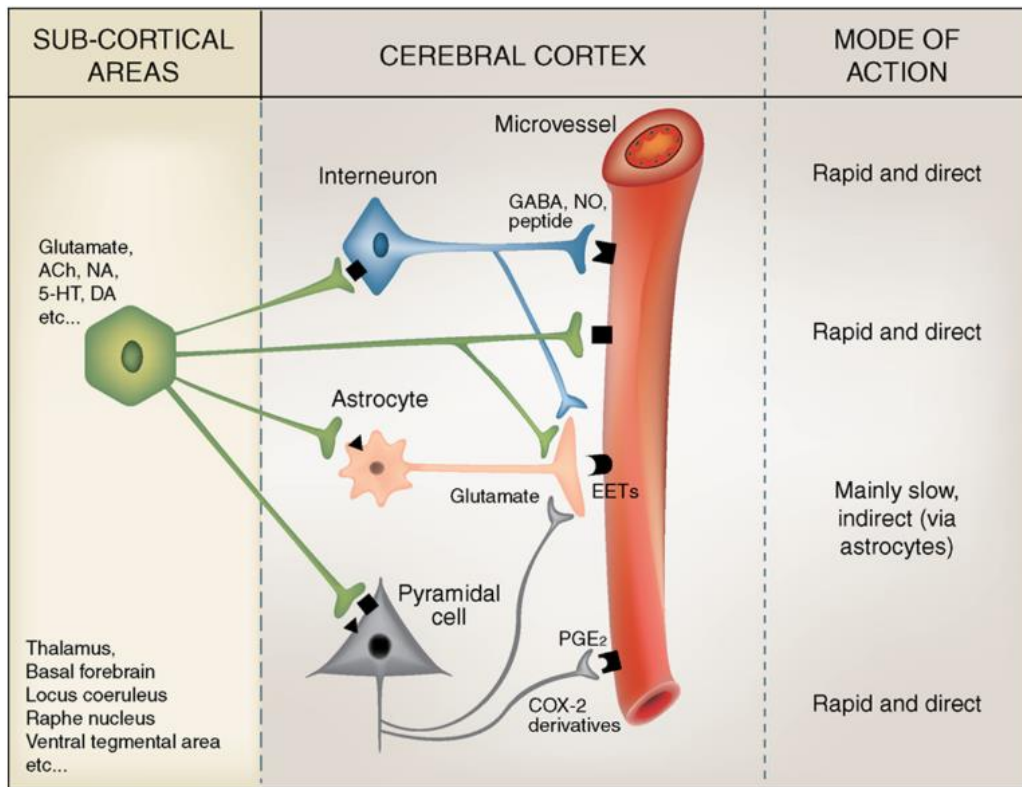


**Figure 1. 2: Summary of the proposed mechanisms involved in regulation of cortical microvessels by excitatory pyramidal cells, inhibitory interneurons, and astrocytes**  
Image originally from Hamel<sup>22</sup> and adapted by Cauli<sup>21</sup>.

Cerebral ischemia exerts a profound effect on the normal regulation of CBF<sup>24,25</sup>.

Following ischemic stroke, the reactivity of the vasculature to stimuli is altered<sup>60</sup>, autoregulation is impaired<sup>61</sup>, and the hemodynamic response due to functional activation is decreased<sup>26–28</sup>. These changes are associated with alterations to the structure and function of the neurovascular unit<sup>11</sup>. The reduction in the hemodynamic response is also associated with a reduction in the underlying neural activity, although the relationship between the reduction in neural versus hemodynamic response is still unclear and therefore the effect of stroke on neurovascular coupling is still unclear<sup>62,63</sup>. A number of studies have tried to address this question and have sometimes led to conflicting results<sup>64–66</sup>. In preclinical

studies, impaired hemodynamic activity has been observed in the tissue surrounding the stroke core despite intact neural activity, suggesting that blood flow does not accurately match the underlying neural activity. One study by Ueki et al. showed that 3 hours after ischemia the increase in CBF to external stimuli was still suppressed while somatosensory evoked potentials had already reappeared, suggesting that ischemia disrupts the coupling between synaptic activity and CBF<sup>64</sup>. Another study reflected similar results in human patients where all patients showed clear synchronized and stimulus-locked firing of neurons in the affected and unaffected primary sensorimotor cortex, but some patients showed no fMRI activation in either the affected or unaffected hemisphere<sup>65</sup>. However, in another study by Weber et al., simultaneously obtained somatosensory evoked potentials and fMRI showed a tight coupling of electrical brain activity and hemodynamic responses following stroke, indicating persistent preservation of neurovascular coupling<sup>66</sup>. Variabilities across studies could arise due to differences in the stroke model used as well as the time course and nature of the experiment and measurements. Most NVC studies measured either just the acute or just the chronic time points and very few studies actually obtained the full longitudinal evolution of functional recovery. Nevertheless, these discrepancies in neurovascular stroke studies have made the interpretation of BOLD fMRI data complicated and therefore NVC after stroke still remains an open question. BOLD fMRI and fNIRS have a huge potential to propel stroke research, predicated on carefully designed preclinical research to address quantitatively the changes in neurovascular coupling and provide the framework for better interpretations of functional neuroimaging findings in clinical settings. Neuroimaging opens the way for greater understanding of the

mechanisms of recovery and potentially improves our ability to deliver effective restorative therapy.

#### **1.4 Preclinical stroke models**

Preclinical animal models, specifically those in rodents, provide a great tool for *in vivo* optical investigation of brain activity both in healthy and diseased brains<sup>67–69</sup>. The last two decades have seen huge progress in our ability to not only record from but also modulate the brain activity of mice *in vivo*<sup>70,71</sup>. Additionally, the advancements in optical technology allow us to observe sub-micron resolution synaptic activity to large-scale population level activity<sup>72–75</sup>. Similarly, stroke studies have also utilized animal models to study the structural and functional alterations that result as a consequence of ischemic stroke<sup>49,76–79</sup> and continue to investigate the exact biological mechanisms involved in injury and eventual recovery<sup>11,12</sup>. Recently, the translational relevance of preclinical stroke models have been called into question, and there has been a great push to maximize the translation of rodent models to the clinical setting by focusing on the ability of the stroke model to more closely mimic the biology of a human stroke<sup>80–82</sup>.

In order to improve the translational nature of the stroke model in the context of studying functional recovery, a few factors can be considered which will allow the model to more closely resemble a human stroke. First, a procedure that allows occlusion of a single arteriole without causing damage to the surrounding tissue will enable ischemic damage to be due to the occlusion and not the procedure<sup>83,84</sup>. Second, a procedure that is minimally-invasive could allow the ischemia to be performed in an awake animal, which

will limit the effects of anesthesia, as anesthetics are potential confounding factors that can alter neural function and CBF<sup>85–87</sup>. Third, a procedure that allows target of a functionally relevant region, such as the somatosensory forelimb or whisker area, can capture the physiological characteristics of a distinct core and penumbra/peri-infarct<sup>47,88,89</sup>. Fourth, a procedure that can be performed without needing to sacrifice the animal after completion can allow for longitudinal monitoring of recovery mechanisms, both cortical and behavioral, in order to capture the acute and chronic phases of the recovery period.

The most commonly used model of ischemic stroke is the middle cerebral artery occlusion (MCAO), which is typically performed by direct mechanical blocking of blood flow by inserting a suture through the carotid artery<sup>90,91</sup>. A main disadvantage of this technique is the use of anesthetics while performing the occlusion, as anesthetics are potential confounding factors that can alter neural function and CBF. Other models of ischemic stroke are the use of ferric chloride to induce vascular thrombosis<sup>92</sup>, topical application of endothelin-1 to induce vasoconstriction<sup>93</sup>, or thrombin injection<sup>94</sup>. Each of these models suffer from different disadvantages of using anesthetics, requiring invasive surgery, or being acute preparations.

One model of ischemic stroke that stands apart from the rest is photothrombosis<sup>95</sup>, which induces ischemic stroke through photoactivation of a photosensitive dye. Illumination of the injected dye with a specific wavelength of light triggers a clotting cascade and leads to thrombosis and thereby occlusion of the targeted area. The downstream region supplied by the target vessel will experience a reduction of or complete loss in blood supply, leading to a starved oxygen environment similar to a human stroke.

As photothrombosis is an optical procedure, it is minimally-invasive and can be performed in an awake animal<sup>96</sup>, and allows for longitudinal monitoring of recovery mechanisms. Additionally, the optics can be tuned to create a small focal illumination point in order to occlude a single vessel with minimum laser damage to the surrounding tissue, and the vessel can be chosen for occlusion based on the regions it supplies to, such as the somatosensory forelimb area. As the vasculature across mice varies significantly, photothrombosis provides variability in the stroke size and extent. Finally, photothrombosis leads to sustained behavioral deficits that can be monitored longitudinally. With all the above benefits in mind, photothrombosis provides an ideal occlusion model to induce ischemic stroke in rodents with high clinical relevance as well as allow simultaneous monitoring of neural and hemodynamic activity through the acute and chronic phases of stroke recovery.

## 1.5 Research overview

In this work we seek to explore the effect of stroke on neurovascular coupling and its relation to longitudinal functional recovery. Results from this work will aid in our understanding of the differences between neural and hemodynamic recovery following stroke and provide insights about their relationship, which will in turn aid in better interpretation of human functional neuroimaging studies. For the purpose of this study, the exploration of neurovascular coupling in mice has been decomposed into three main areas of focus, which are the subjects of the following chapters. Chapter 2 describes our mouse model for a longitudinal stroke study, which involves the optimization of a previously used

stroke model to more closely mimic the pathophysiological processes observed in human stroke patients. Chapter 3 and 4 describe two optical technologies required to allow longitudinal and simultaneous monitoring of hemodynamic and neural activity: Chapter 3 implements spatial frequency domain imaging to longitudinally monitor the spatial extent of the stroke core without having to sacrifice the animal acutely, as well as provide tissue optical properties required for analysis in the following chapter. Chapter 4 implements combined intrinsic optical signal imaging and fluorescence imaging to simultaneously capture hemodynamic and neural activity, and the appropriate analysis techniques for hemodynamic crosstalk correction. Chapter 5 combines work from the previous chapters and explores the effect of stroke on local and global cortical reorganization and investigates the relationships between neural function, hemodynamic responses, and behavioral outcomes. Chapter 6 discusses the implications of the work and presents areas for future exploration. Taken together, this dissertation provides important insights into the effect of stroke on neurovascular coupling in the acute and chronic phases of stroke recovery, and provides a framework upon which functional neuroimaging studies can be better interpreted.

## **CHAPTER TWO – AWAKE CHRONIC MOUSE MODEL OF TARGETED PIAL VESSEL OCCLUSION VIA PHOTOTHROMBOSIS**

### **2.1 Abstract**

Animal models of stroke are used extensively to study the mechanisms involved in the acute and chronic phases of recovery following stroke. A translatable animal model that closely mimics the mechanisms of a human stroke is essential in understanding recovery processes as well as developing therapies that improve functional outcomes. We describe a photothrombosis stroke model that is capable of targeting a single artery with minimal damage to the surrounding parenchyma in awake head-fixed mice. Mice are implanted with chronic cranial windows above one hemisphere of the brain that allow optical access to study recovery mechanisms for over a month following occlusion. Additionally, we study the effect of laser spot size used for occlusion and demonstrate that a spot size with small axial and lateral resolution has the advantage of minimizing unwanted photodamage while still monitoring macroscopic changes to cerebral blood flow during photothrombosis. We show that temporally guiding illumination using real-time feedback of blood flow dynamics also minimized unwanted photodamage to the vascular network. Finally, through quantifiable behavior deficits and chronic imaging we show that this model can be used to study both recovery mechanisms and the effects of therapeutics longitudinally.

## 2.2 Introduction

Stroke is the leading cause of long-term disability and the second leading cause of death worldwide<sup>10</sup>. Strokes are either ischemic, which account for over 85% of all strokes and occur due to the interruption of blood flow caused by thrombosis, or hemorrhagic, which occur due to bleeding<sup>11,12</sup>. During ischemic stroke, a reduction or complete loss in blood supply causes a starved oxygen environment and leads to neuronal damage within minutes and ultimately to sensorimotor and cognitive impairment<sup>11,12</sup>.

Animal models provide a great tool to study the structural and functional consequences of ischemic stroke as well as to develop therapeutic methods to promote recovery after stroke<sup>69,97,98</sup>. In order to maximize the translation of pre-clinical research to the clinical setting, it is essential that animal models of stroke mimic the biology of human stroke<sup>80–82,97</sup>. The most commonly used animal model of ischemic stroke is occlusion of the middle cerebral artery (MCA), which is usually induced by direct mechanical blocking of blood flow via a suture inserted through the carotid artery<sup>90,99</sup>. One of the disadvantages of this model is the use of anesthetics in order to perform the occlusion, as anesthetics are potential confounding factors that alter neuronal function and cerebral blood flow<sup>85,86,100</sup>. Another drawback of this technique is the difficulty in monitoring changes to blood flow during occlusion since the animal is on its back during the procedure<sup>99</sup>. Although a recent study has shown the ability to perform MCA occlusion in a semi-awake setting, the animal preparation is acute and does not allow longitudinal monitoring of stroke progression<sup>101</sup>. Other currently used models of ischemic stroke are ferric chloride induced vascular thrombosis<sup>92</sup>, endothelin-1 induced vasoconstriction<sup>93</sup>, or thrombin injection<sup>94</sup>. However,

these models also suffer from the drawbacks of using anesthetics and being acute preparations.

Another common model of ischemic stroke is photothrombosis, which induces ischemic stroke by photoactivation of a photosensitive dye<sup>95</sup>. Illumination of the injected dye with a specific wavelength of light triggers a clotting cascade and leads to thrombosis. An advantage of this method is that it can be performed in an awake animal, eliminating anesthetics as a confounding factor<sup>102</sup>. Additionally, simultaneous imaging of cerebral blood flow changes or other physiological parameters such as tissue oxygen can be performed during photothrombosis, which can further our understanding of the mechanisms involved during stroke<sup>103</sup>. Photothrombosis also offers the benefit of targeting a specific region by selectively illuminating a region of interest, such as the forelimb region or the barrel cortex in rodents, to study the functional consequences of stroke on specific behaviors over weeks and even months<sup>44,47,89</sup>. However, a disadvantage of illuminating a functionally distinct cortical area is the non-physiological nature of photocoagulating an area of the brain<sup>84</sup>. This form of photothrombosis, with direct cortical wide-beam illumination, leads to widespread thrombosis of all vasculature within the illumination field, including arteries, arterioles, venules, and capillaries. In a natural situation, only the artery supplying the field is occluded. To maximize the relevance of animal models to human stroke it is crucial to target individual vessels and minimize unwanted photoactivation-induced damage to the tissue surrounding the target vessel. Previous studies, albeit under anesthesia, have shown the ability to occlude surface arterioles or individual penetrating arterioles using photothrombosis by controlling the parameters of

laser illumination in order to minimize photo damage to adjacent and deeper vessels<sup>77,83,104</sup>.

Although photothrombosis has been performed in awake animals<sup>105</sup> and has also been used to target individual vessels<sup>83</sup>, these methods have not been previously combined. In this work, we combine the benefits of formerly used techniques to create a chronically prepared mouse photothrombosis stroke model that induces targeted ischemic stroke in awake mice while simultaneously monitoring macroscopic changes to cerebral blood flow. We show the benefits of targeted illumination through Monte Carlo simulations as well as the benefits of guiding illumination using real-time feedback of cerebral blood flow through in vivo measurements. As shown through laser speckle contrast imaging and behavioral evaluation, this method leads to the formation of a reliable stroke with a forelimb functional deficit, which can be monitored chronically to study recovery mechanisms following stroke or to test the effects of potential therapeutics on the recovery process.

## 2.3 Methods

### 2.3.1 *Instrumentation*

A schematic of the imaging system used for photothrombotic stroke is shown in Figure 2.1a. To induce an occlusion in a distal pial branch of the middle cerebral artery (MCA) and simultaneously monitor changes to cerebral blood flow (CBF), the photothrombosis setup was coupled together with a laser speckle imaging system. The photothrombotic arm of the setup consists of a 520 nm laser diode (L520P50, 50 mW, Thorlabs) to photoactivate Rose Bengal via epi-illumination. A scan lens, which consists of three plano-convex lenses,

and tube lens combination, as shown in Figure 2.1b, were used to fill the back pupil of a 2X objective in order to obtain a focal spot with a lateral resolution of 6  $\mu\text{m}$  in diameter and an axial point spread function of 104  $\mu\text{m}$ . A neutral density filter along the imaging path allowed visualization of the illumination spot through a multispectral camera by avoiding oversaturation of the camera (Hamamatsu ORCA-Flash4.0 V3). By illuminating the cranial window with a blue LED, the surface vasculature can be visualized through the multispectral camera, thus making it possible to image the vasculature while performing photothrombosis. A 650nm short pass filter was placed along the path to prevent bleed through from the 785nm laser diode used for laser speckle imaging. Simultaneous laser speckle contrast imaging (LSCI) was performed by illuminating the cranial window using a VHG stabilized 785nm laser diode<sup>106</sup> (LP785-SAV50, Thorlabs) at a power density of approximately 10mW/cm<sup>2</sup> to provide an optimal contrast range and signal to noise ratio<sup>107</sup>. The back scattered light was imaged onto a CMOS camera (Basler acA2040-90um NIR, 2048 x2 048 pixels, 5.5 x 5.5  $\mu\text{m}$  pixel size) with a 2X magnification for a field of view of 5.6 mm x 5.6 mm. A 640 nm dichroic was used to split the visible and near infrared illumination. A polarizer and iris in the imaging path were used to reduce specular reflection and optimize for the speckle size respectively. Images were acquired at 40 frames per second with a 5 ms exposure. Real-time spatial laser speckle contrast was calculated from the raw images captured using software from The Functional Optical Imaging Laboratory at The University of Texas at Austin<sup>108</sup>.

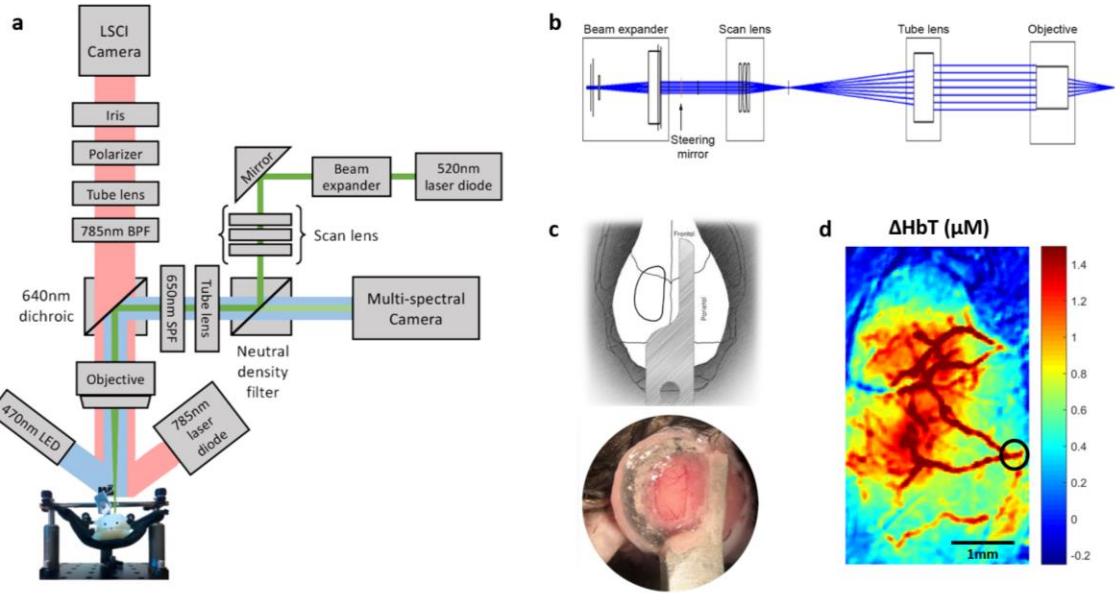


**Figure 2.1: Photothrombosis instrumentation and animal preparation**

(a) Schematic of imaging setup with combined laser speckle contrast imaging, intrinsic signal imaging, and photothrombosis. A parts list for this setup is included in supplementary information Table S1. (b) Zemax model of photothrombosis via epi-illumination. (c) Top: illustration of cranial window and head-bar placement, bottom: representative image of cranial window and head-bar immediately after surgery. (d) Intrinsic optical signal imaging of change in total hemoglobin concentration during air puff stimulation of the contralateral forelimb. Black circle indicates the vessel targeted for photothrombotic occlusion.

### 2.3.2 Surgical procedure

All animal procedures were approved by the Boston University Institutional Animal Care and Use Committee and were conducted following the Guide for the Care and Use of Laboratory Animals. All mice used in this study were adult WT C57Bl6, approximately 12 weeks old at the time of surgery. There were two groups of three mice each to validate our optimized and non-optimized photothrombotic stroke protocols, three mice were used to assess behavioral changes after stroke, and an additional three mice were used for histological analysis.

Mice were anesthetized using isoflurane (3% induction, 1-1.5% maintenance, in 1 L/min oxygen). Dexamethasone was administered 4 hours prior to the start of the procedure to minimize tissue swelling during surgery. Body temperature was maintained at 37°C and mice were monitored using respiratory rate and toe pinch throughout the procedure. A craniotomy was performed over one hemisphere of the brain and the skull was removed leaving the dura intact. The surface was covered with a half-skull-shaped curved glass<sup>109</sup> (modified from Crystal Skull, LabMaker, Germany) and sealed with dental acrylic. An aluminum bar was attached to the intact skull on the other hemisphere for head fixing the mice during photothrombosis and imaging. Animals were given buprenorphine and a prophylactic dose of cefazolin to reduce pain and risk of infection following surgery. The mice were allowed to recover from surgery for at least 10 days before head fixation. Mice were trained to become accustomed to head fixation for up to one hour over approximately 10 days before performing photothrombosis. All experiments are done in awake head-fixed mice<sup>110-112</sup>. A cranial window and head-bar illustration and preparation is shown in Figure 2.1c.

### 2.3.3 *Intrinsic optical signal imaging*

In order to determine the target vessel for photothrombotic occlusion, we performed intrinsic optical signal imaging during air puff sensory stimulation of the contralateral forelimb. Awake head-fixed mice were placed under the imaging setup shown in Figure 2.1a. Three light emitting diodes (LEDs) with center wavelengths at 470 nm, 530 nm, and 625 nm (MXL3-C1, Thorlabs, X is the center wavelength) were used to sequentially

illuminate the cranial window at 30 Hz (each wavelength at 10Hz). Images were collected by the sCMOS camera. For sensory stimulation, each trial consisted of a 5-second train of air puffs at 3 Hz delivered to the forelimb contralateral to the hemisphere implanted with the cranial window. We obtained 20 trials where each trial was obtained in a block-design fashion and consisted of 5 seconds of baseline, followed by 5 seconds of stimulation, followed by 20 seconds of recovery. Custom MATLAB codes were used to synchronize and trigger the sequential LEDs, camera acquisition, and air puff stimulation.

We computed changes in oxy-hemoglobin (HbO) and deoxy-hemoglobin (HbR) from the acquired images using the modified Beer Lambert relationship. Briefly, from the sequence of images acquired, we computed the change in optical density (OD) at each wavelength for each pixel as:

$$\Delta OD(\lambda, t) = -\ln \left[ \frac{I(\lambda, t)}{I_0(\lambda)} \right]$$

where,  $I(\lambda, t)$  is the reflected light intensity at wavelength  $\lambda$  and time  $t$ , and  $I_0(\lambda)$  is the baseline intensity (first 5 seconds of every trial). Using the modified Beer Lambert law:

$$I(\lambda, t) = I_0(\lambda) \exp[-\Delta \mu_a(\lambda, t)L(\lambda)]$$

where  $\Delta \mu_a(\lambda, t)$  is the change in optical absorption coefficient, and  $L(\lambda)$  is the wavelength-dependent mean free path length in the tissue as estimated by Kohl et al.<sup>113</sup> through Monte Carlo simulations of light propagation in tissue. We estimated  $\Delta \mu_a(\lambda, t)$  at each wavelength for each pixel. Using the estimated changes in absorption coefficients, we calculated changes in HbO and HbR for each pixel at each time using a set of three equations and the molar extinction coefficients of HbO and HbR:

$$\Delta\mu_a(\lambda, t) = \epsilon_{HbO}(\lambda)\Delta HbO(t) + \epsilon_{HbR}(\lambda)\Delta HbR(t).$$

Total hemoglobin HbT was calculated as a sum of HbO and HbR. HbT for 20 trials was averaged and the spatial map for change in HbT was obtained for the 5 second stimulus period. This spatial map was used to determine the branch of the MCA that supplied the forelimb region, which was the target branch for photothrombotic occlusion. Figure 2.1d shows a representative spatial map of change in HbT during forelimb activation.

#### 2.3.4 *Focal cerebral ischemia*

To induce an occlusion in a distal pial branch of the MCA while causing minimal damage to the surrounding parenchyma, we used a modified version of photothrombosis previously described by Watson et al. (1985)<sup>95</sup>. The 520 nm collimated laser diode was tuned to a post-objective power of 0.6 mW, which sufficed to occlude the target vessel. The post objective laser power was measured just below the focus before the start of each photothrombosis experiment. Mice were head-fixed and positioned under the imaging system so that the illumination spot was on the target vessel. A translation stage was used for bulk positioning of the mouse and a kinematic steering mirror was used for fine changes to steer the laser beam to the target vessel. The vasculature was visualized under blue light with a multispectral camera. Since Rose Bengal is activated with green light, blue light was used to visualize the vasculature to prevent any unwanted photoactivation. Baseline CBF was obtained using LSCI for ten minutes prior to the start of photothrombosis. Rose Bengal (100 µl, 15 mg/ml in saline) was injected retroorbitally while the mouse was anesthetized briefly with isoflurane. The active use of isoflurane, during induction and retroorbital

injection, was limited to a minute. Isoflurane was immediately discontinued after injection and the mice were allowed to recover from anesthesia, as determined by a return to baseline blood flow in the real-time laser speckle contrast images as well as a return of natural behavior such as whisking, before performing photothrombosis.

One set of animals underwent traditional photothrombosis (non-optimized protocol) where the target vessel was illuminated for 15 minutes, and the other set of animals underwent optimized photothrombosis (optimized protocol), where real-time laser speckle contrast feedback was used to guide the duration of illumination. In the optimized protocol, when the target vessel was occluded, as indicated by the branch disappearing during real-time LSCI, the 520 nm laser was decreased in power to half (0.3 mW post objective) for two minutes and then turned off. If the branch re-perfused, as indicated by a return in blood flow as seen in real-time LSCI, during the 1 hour that the mice were monitored under LSCI, the 520 nm laser was turned on until the vessel was occluded again. Sufficient Rose Bengal was present in the blood stream over an hour after injection as shown in Supplementary Figure 2.1, and can be in the blood stream for several hours after injection<sup>114,115</sup>. Similar to other studies, we found it necessary to target and occlude collateral branches in addition to the main target vessel in order to stabilize the effects of the stroke, since collateral supply or even flow reversal can prevent a single vessel occlusion from having a significant reduction in blood flow in the target region<sup>83,116</sup>. Collateral branches were determined on a case-by-case basis by observing flow redistribution in the MCA-supplied field using the real-time LSCI feedback.

To distinguish between a passive circulatory collapse or distal microembolism in

the nearby capillary network closest to the illumination point and a direct capillary photothrombosis near the illumination area, we tested our protocol in an additional animal, to thrombose two separate pial veins with both the optimized and non-optimized illumination strategies. Those targeted veins were of similar size to the previously targeted arterioles, to allow comparison. When a cortical vein is thrombosed at a single focal point, we can still expect at least some degree of redistributed flow in the nearby upstream capillary bed close to the illumination area, which can be easily detected with OCT angiography. This way, we could avoid the effect of microemboli and a passive circulatory collapse, better revealing the directly photothrombosed zone.

### 2.3.5 *Optical coherence tomography*

Optical coherence tomography (OCT) was used to obtain angiograms of the vasculature at the site of illumination before and after photothrombosis to analyze the vascular damage. A spectral domain OCT system (1310 nm center wavelength, bandwidth 170 nm, Thorlabs) was used for obtaining angiograms as described previously<sup>117</sup>. Briefly, OCT-angiograms were obtained using a frame-to-frame subtraction of the repeated complex OCT B-scan signal. Static tissue will show no (or very low) difference between the repeated B-scans and will appear as dark regions in the OCT angiogram. On the other hand, moving red blood cells within a vessel will cause OCT signal fluctuations resulting in a large intensity difference between the repeated B-scans and will show up as bright areas in the OCT angiogram. A 600 μm x 600 μm region around the target vessel was imaged before stroke and 1 hour after stroke. The region was scanned with 400 x 400 pixels to obtain a pixel

size of  $1.5 \times 1.5 \mu\text{m}^2$ . Each OCT angiogram was repeated 20 times to obtain an average of 20 angiograms. The transverse and axial resolutions of the OCT system using a 10X objective (Mitutoyo) were  $3.5 \mu\text{m} \times 3.5 \mu\text{m} \times 3.5 \mu\text{m}$ .

### 2.3.6 *Histological analysis*

In order to confirm the formation of an infarct, in two mice we performed histological staining with triphenyl-tetrazolium chloride (TTC) on fresh tissue at 24 hours after photothrombosis. TTC staining is used to differentiate between metabolically active and inactive tissue and is commonly used to identify infarcted tissue. The mice were deeply anesthetized with isoflurane and decapitated, and their brains were removed for TTC staining. The intact brain was incubated at 37C for 30 minutes in 2% TTC in 1X PBS. Images were acquired immediately after staining.

To assess the damage done to tissue at the illumination site, we stained for necrotic and apoptotic cells using Propidium Iodide (PI). PI is a fluorescent marker that binds to DNA of a cell but is not membrane permeable. This allows us to differentiate necrotic and apoptotic tissue from healthy cells. Mice were injected with 300 $\mu\text{l}$  of 1mg/ml of PI diluted in 300 $\mu\text{l}$  of saline intraperitoneally (IP) 24 hours after photothrombosis. We performed *in vivo* two photon imaging of PI 3 hours after injection at the illumination site and the stroke core. The mice were perfused 4 hours after PI injection with heparinized PBS followed by a 10% w/v gelatin solution in PBS with 30mg/ml of FITC-albumin in order to visualize the vasculature during *ex vivo* imaging. The brains were extracted and transferred to 4% PFA for 6 hours followed by 1X PBS for 3 days. The brains were then index matched with

increasing concentrations of fructose and sliced at the location of the target vessel for occlusion. The brains were then mounted in 100% fructose and imaged with a two-photon microscope to assess depth of tissue damage.

### *2.3.7 Behavioral testing*

The cylinder test was used in three mice to assess behavioral deficits in forelimb use over the course of 4 weeks following stroke<sup>118,119</sup>. Baseline testing was obtained the week before stroke induction to assess basal preference in forepaw use. Following photothrombotic stroke, mice were tested at 4 hours, 1 day, 3 days, 1 week, 2 weeks, 3 weeks, and 4 weeks. Each testing session involved placing a mouse in a clear glass cylinder and videotaping its natural behavior from below for 15 minutes. Forelimb use was assessed by counting the number of times the mouse used each forelimb to make first contact with the cylinder wall during rears. Asymmetry in forelimb use after stroke was quantified as a percent change from baseline use of the contralateral forelimb. Change from baseline was used to compensate for the fact that some mice have a preference for one paw over the other even before a stroke.

### *2.3.8 Data analysis*

Flow dynamics were analyzed offline through spatial speckle contrast by applying the commonly used model of blood flow index<sup>120</sup>. The speckle contrast was calculated from raw images captured by the camera using the equation,

$$K = \frac{\sigma_s}{\langle I \rangle}$$

where the spatial speckle contrast ( $K$ ) is defined as the ratio of the spatial standard deviation ( $\sigma_s$ ) and the mean intensity ( $I$ ) of the pixels in a  $7 \times 7$  bin. To provide a qualitative measure of blood flow dynamics, the blood flow index was calculated using<sup>111</sup>

$$BFI = \frac{1}{K^2}.$$

OCT angiograms were analyzed for capillary density differences between the optimized and non-optimized photothrombosis protocols. A custom MATLAB script was used to segment the vasculature and obtain the capillary density of a  $150 \mu\text{m}$  thick section of the  $600 \mu\text{m} \times 600 \mu\text{m}$  region of interest. Capillary segmentation was performed below the large surface vessels. The mean and standard deviation of capillary density was compared before and after stroke for the two groups. In addition to mean capillary density, the capillary density as a function of radial distance from the illumination site was calculated. Results are expressed as mean and standard deviations. Statistical analyses were made using an ANOVA with *post hoc* comparisons using t-tests. For capillary densities a two-sample t-test was performed to compare densities before and after stroke for each protocol. Additionally, the two-sample t-test was used to compare the capillary densities at different radial distances between the optimized and non-optimized protocols. For behavior analysis with the cylinder test, multiple pairwise comparisons were made with the pair-sample t-test at each time point with respect to baseline. A p-value of less than 0.05 was accepted as statistically significant.

## 2.4 Results

### 2.4.1 A $6\text{ }\mu\text{m}$ spot is superior to a $30\text{ }\mu\text{m}$ spot in preventing capillary damage as shown by Monte Carlo simulations

The photothrombosis laser was incorporated into an existing laser speckle contrast imaging system via epi-illumination to be able to simultaneously image changes to blood flow during vessel occlusion. To target a single branch of the middle cerebral artery without damaging the surrounding parenchyma, we designed a laser beam path that resulted in the smallest spot size possible given the imaging system's parameters. Filling the back aperture of a 0.1NA objective resulted in a spot size with a lateral resolution of  $6\text{ }\mu\text{m}$  in diameter at the focus and a Rayleigh range of  $60.8\text{ }\mu\text{m}$ . Zemax was used to design the required scan lens in order to fill the back pupil of the 2X objective with a 200 mm tube lens. The required beam profile was achieved with a combination of three plano-convex lenses as described in section 2.3.1. The Zemax model of the photothrombosis arm is shown in Figure 2.1b. The true beam size was validated and confirmed using a knife-edge beam profiler.

Photon migration within the tissue for the  $6\text{ }\mu\text{m}$  spot was modeled using a Monte Carlo simulation and compared against a simulation of a  $30\text{ }\mu\text{m}$  spot size (Figure 2.2a), since a number of previous studies have used a  $30\text{ }\mu\text{m}$  spot to perform targeted photothrombosis. A  $30\text{ }\mu\text{m}$  spot will have a very small NA of 0.02 and a Rayleigh range of 1.4 mm as shown in Figure 2.2a, resulting in less divergence of the beam. Thus, power density falls off slowly for the  $30\text{ }\mu\text{m}$  spot size, which will result in damage of not only the target vessel but also all the vessels within the parenchyma down to 1mm. However, a  $6\text{ }\mu\text{m}$  illumination spot has an NA of 0.1 and the beam diverges more quickly such that any

parenchymal photothrombotic damage will be limited to ~150  $\mu\text{m}$  below the target vessel as the power density beyond that depth drops below the threshold for activating Rose Bengal.

Tissue damage in depth due to illumination with the 6  $\mu\text{m}$  spot was validated in vivo and ex vivo using PI staining of damaged cells. Figure 2.2b shows damage at the target vessel location where the left panel indicates PI staining in vivo at 60  $\mu\text{m}$  depths apart starting from the surface and the right panel shows damage ex vivo. PI positive cells are no longer visible at 180  $\mu\text{m}$  below the surface, which was confirmed ex vivo where the damage was also limited to 150-200  $\mu\text{m}$  below the surface. This was in contrast to damage observed at the stroke core (Figure 2.2c), which was over 500  $\mu\text{m}$  away from the illumination site and any damage was due to occlusion itself and not the illumination. PI positive cells are present even at 300  $\mu\text{m}$  below the surface in vivo as shown in the left panel of Figure 2.2c and the full extent of the stroke core is shown ex vivo in the right panel of Figure 2.2c where it extends deep into cortex.

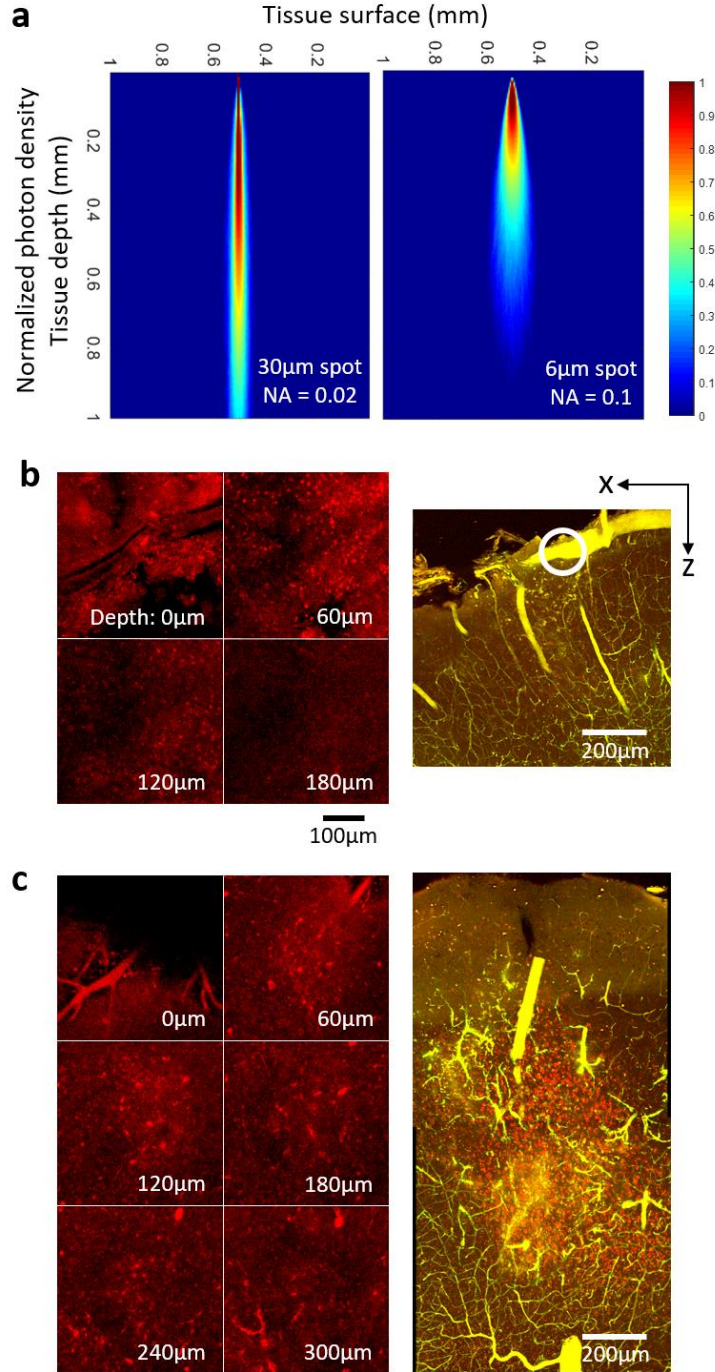


**Figure 2.2: Tissue damage with a 30  $\mu\text{m}$  and 6  $\mu\text{m}$  spot size**

(a) (Left) Monte Carlo simulation of photon density for a 30  $\mu\text{m}$  spot with numerical aperture of 0.02 and (right) for a 6  $\mu\text{m}$  spot with numerical aperture of 0.1. (b) PI staining in vivo (left) and ex vivo (right) at the site of illumination (circled in white). (c) PI staining in vivo (left) and ex vivo (right) at the stroke core.

#### 2.4.2 Optimized and non-optimized methods produce an ischemic stroke

Typically, previous studies have used a fixed duration of 10-15 min of laser illumination to occlude the target vessel<sup>102,115,121</sup>. Following a similar protocol, in one group of animals we illuminated our target vessel for 15 min with a laser power of 0.6 mW. We call this the non-optimized protocol. Occlusion was confirmed by measuring a greater than or equal to 80% drop in the qualitative blood flow index with LSCI and also a greater than 50% decrease in the region supplied by the target vessel by monitoring real-time spatial laser speckle contrast imaging feedback. For the optimized group, we used real-time LSCI feedback to guide the duration of illumination. Both the non-optimized and optimized groups showed an 80% decrease from baseline cerebral blood flow (CBF) in the target vessel as seen in the time course of the relative blood flow changes in the bottom panels of Figure 2.3a and 2.3b. Additionally, the regions supplied by the target vessel showed similar patterns of change in CBF from baseline in both groups (Figure 2.3a,b). The stroke core, which generally lies in the area supplied by the target vessel and indicated by region 1, sees a 60% drop in blood flow in both groups. Region 2 is shown as a representative region away from the tissue supplied by the target vessel.

CBF analysis is not provided for the periods when the collaterals were targeted, as indicated by breaks in the CBF time course plots since we needed to reposition the mouse so that the desired vessel was directly under the illumination spot. The targeted collaterals are indicated with black arrows in the leftmost reference images in Figure 2.3a,b. We found it necessary to target two to three collaterals to stabilize the effects of the stroke. An example collateral target is shown in Figure 2.3c with the black circle. The top panel shows

real-time laser speckle contrast images and the bottom panel shows the associated change in blood flow compared to baseline. We followed the same parameters of the optimized protocol to target the collaterals, where the illumination was turned on until the vessel was occluded following which the laser was turned off and the mouse repositioned to the original location. If the collateral branches re-canalized the mouse was moved again in order to occlude them. The time course of collateral occlusion is represented by breaks in the CBF time course in Figure 2.3a,b.

The optimized protocol used real-time laser speckle feedback to guide the duration of illumination of the target vessel. The green shaded region of the time course in Figure 2.3a,b is when the 520 nm laser was on. After the initial occlusion period, the laser was turned on again when the target vessel re-canalized, as shown by representative images in Figure 2.3d. A return of blood flow, indicated by a drop in laser speckle contrast signal intensity, was used as the criteria to turn the laser on, and a subsequent occlusion, indicated by an increase in signal intensity, was used to turn the laser off. This criteria for a return of blood flow and the subsequent occlusion are qualitative measures that are easily visualized in real-time laser speckle contrast images as the entire branch recanalized or disappeared respectively.

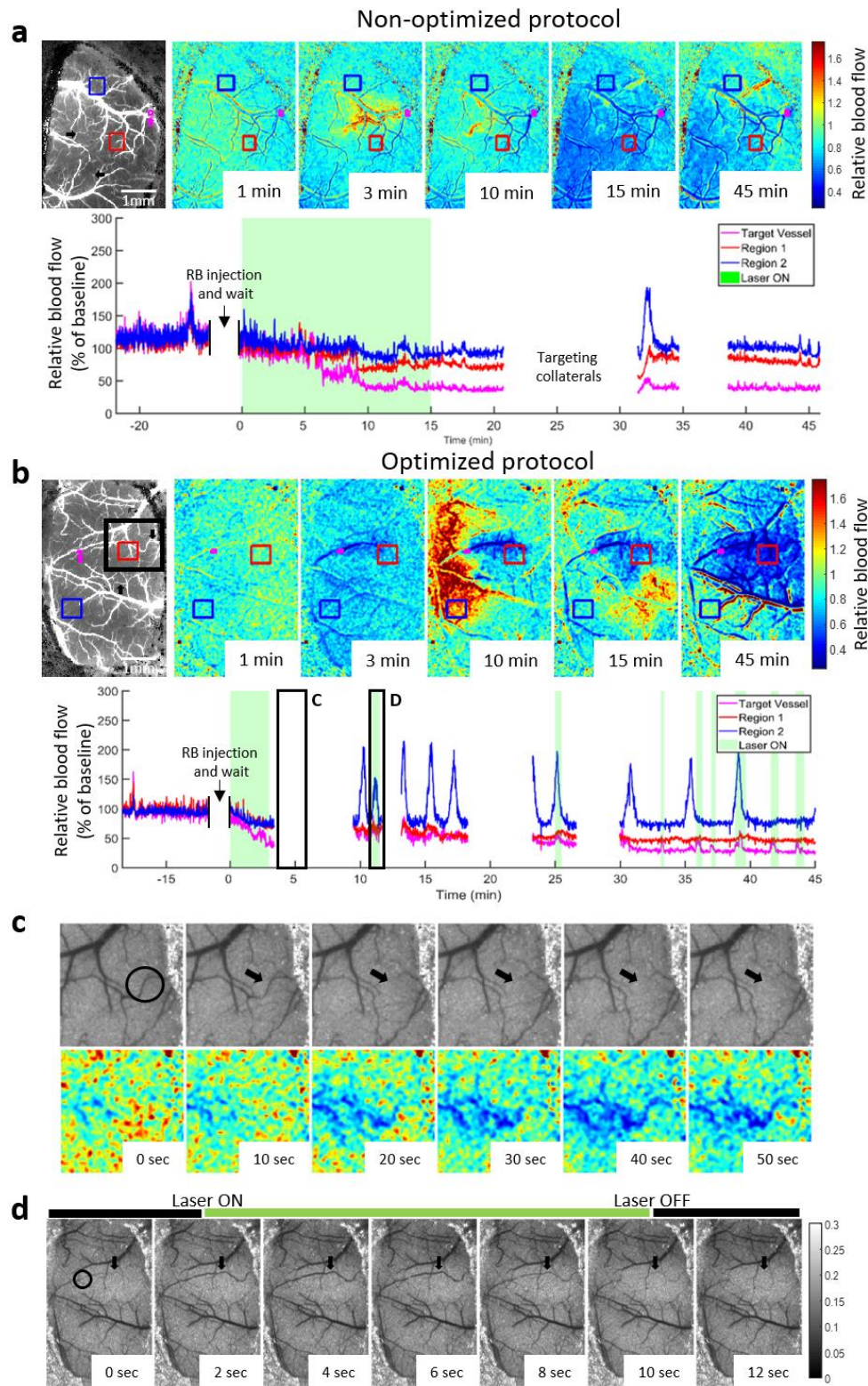


**Figure 2.3: Relative cerebral blood flow maps during photothrombosis**

(a) Relative CBF during non-optimized photothrombosis and (b) during optimized photothrombosis. Top panel shows spatial blood flow dynamics and bottom panel shows temporal dynamics for the regions specified in the top panel. Leftmost image in the top panel of (a) and (b) shows a reference indicating the target vessel in magenta arrows and collateral branches targeted for occlusion in black arrows. Both non-optimized and optimized protocol show similar blood flow dynamics during occlusion. Green shaded region on the bottom panel corresponds to photothrombosis laser ON periods. (c) Representative images showing collateral (circled in black) occlusion. Top panel shows laser speckle contrast images as visualized in real-time. Bottom panel shows relative blood flow changes associated with the occlusion. The region shown is represented as the black square in the reference image of the top panel of (b) and the time course chosen for images in (c) is shown as the first black square indicated as ‘C’ in the bottom panel of (b). (d) Representative images showing criteria for Laser ON/OFF periods in the optimized protocol. The time course chosen for images is shown as the second black square indicated as ‘D’ in the bottom panel of (b). Laser is turned on when the target vessel re-canализируется, indicated with a drop in intensity in real-time laser speckle contrast, and turned off when the vessel is occluded again, indicated with an increase in signal intensity of the target vessel.

#### 2.4.3 *The optimized method prevents capillary thrombosis*

The effect of photothrombosis on blood flow in the surrounding capillaries was assessed *in vivo* using OCT angiograms. The difference between image intensities of two repeated B-scans permits the detection of flowing capillaries. Figure 2.4 shows the average OCT angiograms of both the non-optimized and optimized photothrombosis methods for three mice in each group. In Figure 2.4a we show that after non-optimized photothrombosis there is a significant decline in capillary density immediately surrounding the targeted pial artery. The left panel in Figure 2.4a also shows that 1 hour after stroke, even though the surrounding parenchymal capillaries remained occluded, the target branch has re-canализировалась. This indicates that the traditional method of illuminating the target vessel for a fixed longer duration is not necessarily sufficient to occlude the vessel for even 1 hour post

stroke, but has produced a persistent cessation of blood flow in the immediate vicinity. These capillaries have been photothrombosed because of the prolonged laser exposure in the non-optimized method, and while the pial artery has recanalized in this case, the capillaries have not because their smaller diameter stabilized the thrombi.

Figure 2.4b shows the averaged OCT angiograms for the optimized protocol. We see that just the illuminated target vessel is occluded, and all the surrounding capillaries are intact. Both the optimized and non-optimized protocols show spontaneous recanalization in the target vessel after photothrombosis in some cases. Any drop in surrounding vessel density in the optimized protocol is due to blocked capillaries downstream of the target vessel. This can be shown by thrombosing a vein, as veins do not have any downstream capillaries and hence the capillary network should remain intact unless directly illuminated by the laser.

Figure 2.4c shows a vein photothrombosis with the optimized and non-optimized protocol. We see that with the optimized protocol only the target vessel is thrombosed and the capillary network within the immediate vicinity is intact, while in the non-optimized protocol the capillary network around the target vessel is also thrombosed. The optimized laser illumination ensures that the laser exposure to the capillaries remains below the threshold for photothrombosis to occur.

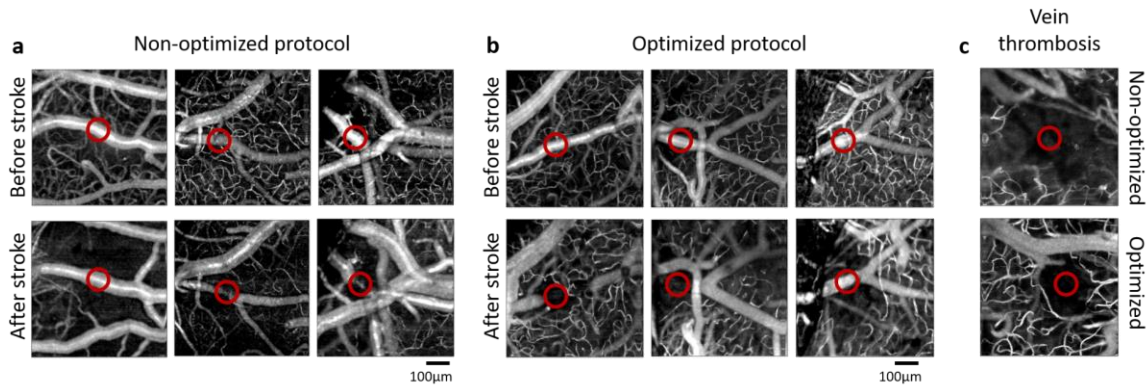


**Figure 2.4: Capillary damage with non-optimized and optimized photothrombosis**  
 (a) OCT angiograms of flowing vessel before stroke (top panel) and 1-hour after non-optimized stroke (bottom panel). (b) OCT angiograms of flowing vessel before stroke (top panel) and 1-hour after optimized stroke (bottom panel). (c) Vein thrombosis after non-optimized stroke (top panel) and after optimized stroke (bottom panel). The target vessel is shown by the red circle.

Quantitative analysis of vessel density also showed a decrease in capillary density for the non-optimized photothrombosis, as seen in Figures 2.5b,c. Figure 2.5a shows an example OCT angiogram before and after stroke (left column), with the red circle indicating the site of laser illumination. The middle panel of Figure 2.5a shows the maximum intensity projection of the segmented vasculature of the same example mouse for a 150 µm thick section of capillaries. In order to look at the capillary density as a function of distance from the site of occlusion, we constructed 50 µm concentric rings starting at 100 µm from illumination center and out to 300 µm. Figure 2.5b shows the capillary density for the full imaged region before and after stroke, averaged across 3 mice for each group. The non-optimized protocol shows a significant decrease in capillary density after stroke compared to before stroke ( $p<0.05$ ), while the optimized protocol does not show a significant decrease in capillary density. When looking at the capillary density as a function of distance from illumination, we see that the capillary density of optimized

protocol returned to baseline levels at 150-200  $\mu\text{m}$  from the center as shown in Figure 2.5c.

However, the capillary density of the non-optimized protocol remained at less than 50% of baseline vessel density out to 300  $\mu\text{m}$ . Capillary density of the non-optimized method was significantly less than that of the optimized method at greater than 150  $\mu\text{m}$  from the occlusion site ( $p<0.05$ ).

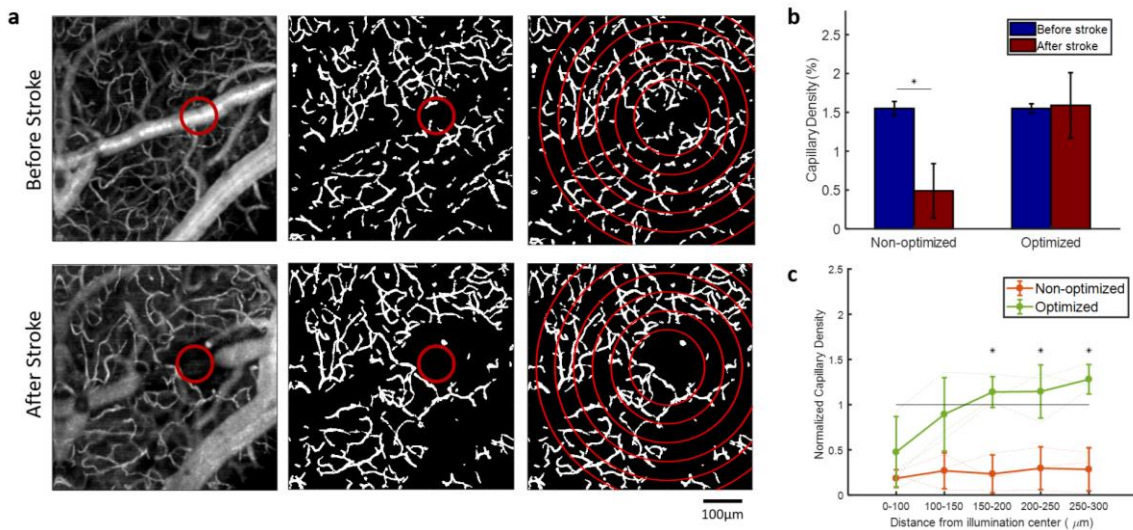


**Figure 2.5: Vessel segmentation and quantification of capillary damage**

(a) Example schematic of vascular segmentation in the optimized protocol. Left column shows an example angiogram with occlusion site within the red circle. Middle column shows capillaries segmented beneath the larger pial vessels. Right column shows 50  $\mu\text{m}$  concentric rings used to calculate capillary densities as a function of distance from the occlusion site. (b) Average vessel density for non-optimized and optimized methods before and 1-hour after stroke. The non-optimized protocol shows a significant decrease in capillary density after stroke compared to before stroke (\* $p<0.05$ ). (c) Capillary density as a function of distance from the occlusion site normalized to the baseline capillary density. Capillary density of the non-optimized method was significantly less than that of the optimized method at distances greater than 150  $\mu\text{m}$  from the occlusion site (\* $p<0.05$ ).

*2.4.4 Formation of a stable infarct was confirmed using blood flow changes, histological validation, and behavioral analysis*

In this study we simultaneously monitor changes to blood flow during stroke induction. This allowed us to visualize and confirm in real time the occlusion of the target vessel as well as a drop in blood flow to the area supplied by the vessel. Figure 2.6a shows a representative image of relative CBF 1 hour after photothrombosis. We observed a greater than 80% drop in blood flow within the target vessel and greater than 50% decrease in blood flow in the region supplied by the target vessel. TTC staining of viable tissue was used to confirm infarct formation at 24 hours after photothrombosis in a subset of animals. Figure 2.6b shows infarcted tissue corresponding to the region of low blood flow in Figure 2.6a. The target vessel is marked with black circles. In addition to decreased blood flow and histological damage, we monitored change in contralateral forelimb use with the cylinder test at various time points following photothrombosis. We observed a decrease in use of the forelimb contralateral to the ischemic hemisphere (impaired forelimb) when compared to baseline use as shown in Figure 2.6c. There was a significant decrease ( $p<0.05$ ) in the use of the impaired forelimb till one week after photothrombosis, following which behavior trended towards recovery to baseline. With these metrics we can confirm that our optimized photothrombotic stroke model can produce a reliable infarct with associated functional deficits.

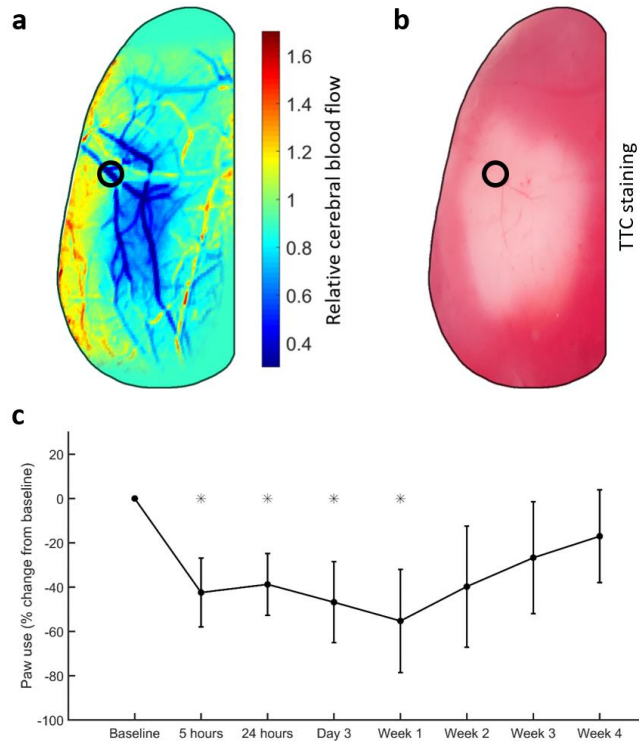


**Figure 2.6: Validation of stable infarct obtained with optimized photothrombosis**

(a) Relative cerebral blood flow at 1 hour after photothrombosis. The target vessel is indicated with the black circle. (b) Triphenyltetrazolium chloride (TTC) stain at 24 hours after photothrombosis. The infarct site coincides with the area of reduced cerebral blood flow (<60% of baseline) shown in (a). (c) Percent change in paw use of the impaired forelimb (contralateral to stroke) over the course of 4 weeks. Mice showed a significant decrease in the use of the impaired forelimb specifically till 1 week following photothrombosis. \* $p<0.05$ .

#### 2.4.5 *The chronic use of our model was validated using longitudinal imaging of vasculature*

Our cranial window preparations allow longitudinal monitoring in awake mice, which can be used to study stroke recovery mechanisms or the long-term effects of therapies. Here, we show that we are able to follow vascular structure using two-photon microscopy for one month following photothrombosis (Figure 2.7). While we followed the vasculature for

one month, at which point the mice were sacrificed for ex vivo analyses, the mice can be monitored for even longer time points if desired since one-month post-stroke showed minimal deterioration to the window quality. An inflammatory response that results due to the lesion could cause cellular build up under the window which could deteriorate the quality of the window. However, that deterioration is minimal and we are able to penetrate to 400  $\mu\text{m}$  below the surface with sufficient signal to background ratio using a two-photon microscope. In order to test the longevity of the cranial windows, we followed control mice for 6 months and expect that the stroked mice can also be followed for that long. Thus, our model is ideal for longitudinal stroke studies and can be used to study various physiological parameters across a number of imaging modalities.

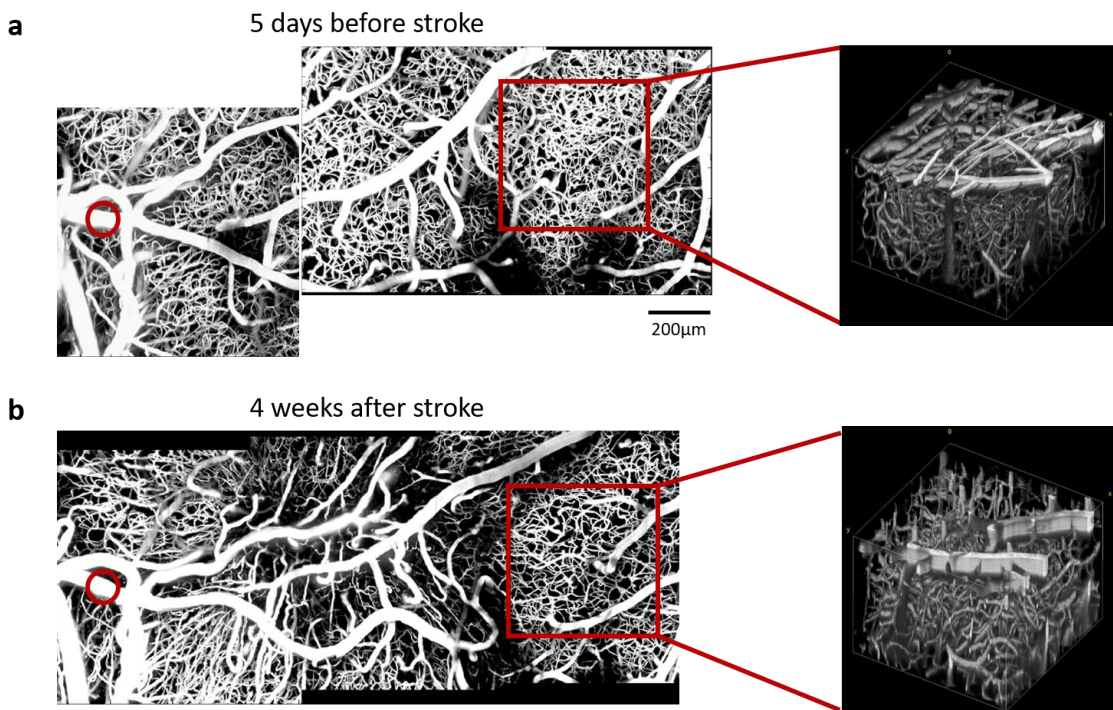


**Figure 2.7: Longitudinal multi-modal optical imaging after stroke**

Two-photon maximum intensity projections (left) and volumes (right) of 400  $\mu\text{m}$  stack (a) 5 days before photothrombosis and (b) 4 weeks after photothrombosis. Red circle indicates vessel targeted for photothrombosis. Red square indicates regions chosen for volume projections.

## 2.5 Discussion

We have developed a chronic animal model that can be used to induce ischemic stroke in awake mice while monitoring changes to cerebral blood flow. We also show that the limited laser spot size and real-time CBF permits us to occlude a target pial artery without occluding the surrounding and underlying capillaries. Although a number of previous models have performed single vessel occlusion and produced the desired ischemic core and peri-infarct zone, they were performed on anesthetized mice<sup>83,84,104,122</sup>. Anesthetics are known to modulate blood flow, which could impact the mechanisms leading to parenchymal failure after a stroke<sup>85–87,100</sup>. Additionally, it has been shown that anesthetics can mask the benefits of a neuroprotective therapy<sup>102</sup>. A prior study has shown the ability to use an MCA occlusion model without the effects of anesthesia, but the animal preparation is acute and does not allow the animals to recover from surgical procedures, which could be a confounding factor<sup>101</sup>. Our model uses a cranial window preparation that is performed three weeks prior to stroke induction, allowing the mouse time to recover from the surgery. Additionally, our cranial windows allow longitudinal monitoring of stroke recovery mechanisms, which can be used to study long-term stroke progression or the long-term effects of therapies.

The photothrombotic stroke model is advantageous for studying the mechanisms of the functional, structural, and behavioral responses involved in stroke recovery due to its ability to precisely target a desired region<sup>44,47,89,103,123</sup>. However, a drawback of directly targeting an anatomically distinct area, which includes larger vessels and parenchyma, using photothrombosis, is the relatively small ischemic penumbra that results due to

oxidative damage primarily within the ischemic core, rather than gradually distributed in the peri-infarct zone<sup>84,97,98</sup>. This hinders the understanding of how mechanisms within the peri-infarct influence functional recovery. In this chapter we have shown that targeting an upstream branch of the MCA supplying a functionally distinct area is capable of creating an infarct core in the area it supplies as seen by greater than 60% drop in blood flow, as well as a penumbra as seen by a 40-60% drop in blood flow in the area surrounding the ischemic core. This method of artery targeted photothrombosis that leads to a widened vascular penumbra suitable to study recovery mechanisms within the peri-infarct zone has also been shown previously by Clark et al.<sup>84</sup>. We have also shown that our model is capable of targeting a distinct functional area of the forelimb cortical representation that produces longitudinally quantifiable deficits in forelimb use.

Additionally, through Monte Carlo simulations we have shown that the size of the beam used to occlude the target vessel must be considered in order to minimize unwanted photodamage to the surrounding parenchyma. We have shown that it is not sufficient to decrease the lateral resolution of the illumination spot to the size of the branch being targeted. The size of a distal MCA is ~30-50  $\mu\text{m}$ , and a spot size with a lateral resolution of 30  $\mu\text{m}$  will result in vascular damage of over 1mm beneath the target vessel. Decreasing the spot size to a 6  $\mu\text{m}$  lateral resolution resulted in significantly less unwanted vascular damage and was limited primarily to the target surface vessel. Histological evidence validated that the parenchymal damage was limited to the surface at the site of illumination, while the core showed damaged parenchyma deep in cortex.

Other groups have shown the ability to use photothrombosis to induce the desired

core and peri-infarct zones using variations of the vessel occlusion model. A number of single-vessel occlusion models have been proposed that utilize an objective with higher magnification and larger numerical aperture to target a region smaller than the vessel itself to minimize photodamage<sup>83,122</sup>. They typically involve starting laser illumination on one side of the vessel and traversing the laser beam laterally to facilitate thrombus formation along the vessel. Although this leads to negligible unwanted photodamage, it does not allow simultaneous macroscopic imaging of CBF. These models also result in relatively small ischemic regions that are useful for studying the effects of small strokes but are not large enough to follow functional recovery mechanisms. Another model is artery-targeted photothrombosis using a digital micromirror device (DMD) to provide patterned illumination along the length of the artery with minimal exposure to the surrounding parenchyma<sup>84,103,124</sup>. This method also allows targeting multiple arteries simultaneously, permitting illumination of collaterals together with the main branch and thus controlling perfusion within the area. Some drawbacks of these methods are that photothrombosis is still performed under anesthesia and the instrumentation is more expensive and difficult to implement.

In addition to spatially adjusting the laser illumination, we have also shown the advantages of temporally controlling the duration of illumination. A previous study has mentioned the use of real-time blood flow feedback to guide photothrombosis<sup>77</sup> and in this study we show that the typically used fixed-duration illumination protocol results in unwanted vascular damage and optimizing that protocol to guided illumination using real-time blood flow feedback further minimizes damage to the surrounding parenchyma. The

duration of illumination is limited to when the target vessel is flowing, as observed using laser speckle contrast imaging. Capillary damage was analyzed by looking at the density of flowing capillaries obtained from OCT, where we show an intact flowing capillary network in the immediate vicinity of the occluded vessel in the optimized protocol as opposed to the non-optimized protocol. To rule out the possibility of downstream capillary thrombosis due to laser illumination, we performed optimized thrombosis on a vein, which did not show any drop in capillary density apart from the target branch. However, vein photothrombosis using the non-optimized protocol showed a similar drop in capillary density compared to artery illumination with the non-optimized protocol.

This photothrombosis stroke model also has a few limitations. One limitation is the brief use of isoflurane during intravenous Rose Bengal injection. Although the use of isoflurane is limited to a minute, it must be noted that there may be remnants of its effects even after the discontinuation of anesthesia. As we are primarily concerned about the effects of isoflurane on blood flow during photothrombosis, our criteria of recovery is the return of blood flow to baseline levels as seen with real-time laser speckle contrast imaging before the start of photothrombosis. A second limitation is that the laser needs to be manually turned on and off to optimize the illumination duration. This can be automated in the future by linking the real-time CBF from laser speckle contrast imaging to the laser for photothrombosis. Additionally, the mouse needs to be laterally translated when targeting the collateral branches. This can also be improved upon by allowing a larger range of lateral control of the laser beam.

In brief, this model is fairly easy and inexpensive to implement and can be used for

experiments that more accurately mimic the mechanisms and recovery processes of ischemic stroke and allows longitudinal monitoring of recovery mechanisms.

## 2.6 Supplementary material

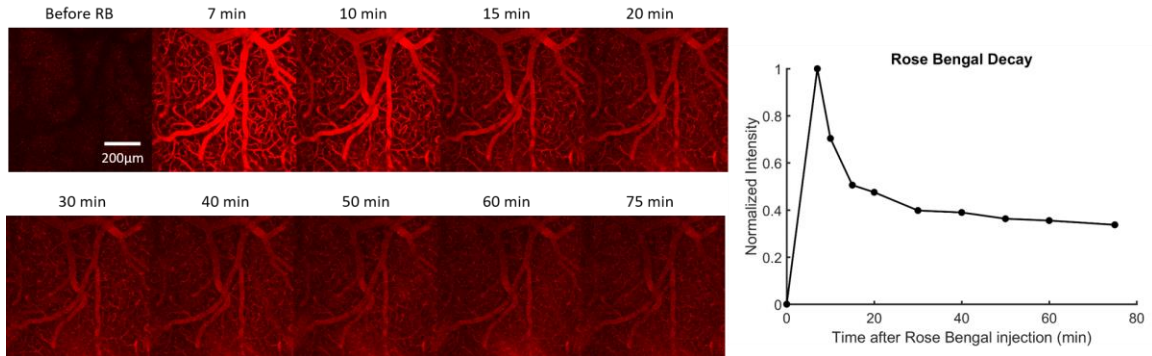


**Figure 2.8: Rose Bengal decay imaged using two-photon microscopy**

The left panel shows 150  $\mu\text{m}$  maximum intensity projections of the vasculature imaged before and at various time points after Rose Bengal injection. The laser and signal amplification parameters were kept constant throughout the session. The right panel shows normalized signal intensity over time. Rose Bengal decays exponentially as expected. We observe that ~40% of the initial Rose Bengal is still present in circulation at 1 hour after injection.

**Table 2. 1: Supplementary table with list of parts for IOSI, LSCI, and photothrombosis system**

Parts list for the combined photothrombosis, laser speckle contrast imaging, and intrinsic optical signal imaging system.

Combined multispectral and laser speckle imaging system				
	Item	Vendor	Part	Quantity
<b>Illumination (IOSI)</b>	LED	Thorlabs	M470L3	1
		Thorlabs	M530L3	1
		Thorlabs	M625L3	1
	Filters	Thorlabs	FB470-10	1
		Thorlabs	FB530-10	1
		Thorlabs	FB620-10	1
	LED power	Thorlabs	LEDD1B	3
		Thorlabs	KPS101	3
	Collimation	Thorlabs	ACL2520U-DG6-A	3
		Thorlabs	SM1V05	3
		Thorlabs	SM1L03	3
	Dichroics	Thorlabs	MD568	1
		Thorlabs	DMLP490R	1
		Thorlabs	DFM1B	2
<b>Illumination (LSCI)</b>	Laser diode	Thorlabs	LP785-SAV50	1
	Current controller	Thorlabs	LDC205C	1
	Temperature controller	Thorlabs	TED200C	1
	Laser diode mount	Thorlabs	LDM9LP	1
	Collimation and expansion	Thorlabs	F280FC-780	1
		Thorlabs	AD1109F	1
		Thorlabs	GBE05-B	1
<b>Objective</b>	2X, 0.1NA, 56mm WD	Thorlabs	TL2X-SAP	1
<b>Image splitting</b>	Beamsplitter	Semrock	FF640-FDi02-t3	1
<b>Filters</b>	IOSI	Thorlabs	FESH0650	1
	LSCI	Thorlabs	FB780-10	1
<b>Camera lenses</b>	IOSI	Thorlabs	TTL200-A	1
	LSCI	Thorlabs	TTL200-B	1

<b>Camera</b>	IOSI	Hamamatsu	ORCA Flash 4.0 V3	1
	LSCI	Basler	acA2040-90um NIR	1
<b>Translation stages</b>	X,Y translation	Thorlabs	LTS150	2
	Z translation	Thorlabs	MLJ150	1
<b>Optomechanics</b>	Base breadboard	Thorlabs	MB30	1
	Microscope body	Thorlabs	CEA1400	1
	Objective holder	Thorlabs	ZFM1020	1
	Breadboard top	Thorlabs	CSA3010	1
	National instruments DAQ	NI	PCIe-6321 X Series DAQ	1
<b>Photothrombosis</b>				
Item	Vendor	Part	Quantity	
Illumination	Laser diode	Thorlabs	L520P50	1
	Collimation	Thorlabs	C110TMD-A	1
		Thorlabs	LDH56-P2	1
	Strain relief cable	Thorlabs	SR9HA-DB9	1
	Beam expander	Thorlabs	GBE05-A	1
	Current controller	Thorlabs	LDC205C	1
Optics	Kinematic mirror	Thorlabs	KCB2C	1
		Thorlabs	BB2-E02	1
	Scan lenses	Edmund Optics	32-861	1
		Edmund Optics	32-865	2
	ND filter	Edmund Optics	46-123	1
		Thorlabs	LC6W	1
Optomechanics	Breadboard	Thorlabs	MB1224	1
	Lens housing	Thorlabs	SM2NR1	1

## CHAPTER THREE – STROKE CORE REVEALED BY TISSUE SCATTERING USING SPATIAL FREQUENCY DOMAIN IMAGING

### 3.1 Abstract

Ischemic stroke leads to a reduction or complete loss of blood supply causing injury to brain tissue, which ultimately leads to behavioral impairment. Optical techniques are widely used to study the structural and functional changes that result as a consequence of ischemic stroke both in the acute and chronic phases of stroke recovery. It is currently a challenge to accurately estimate the spatial extent of the infarct without the use of histological parameters, however, and in order to follow recovery mechanisms longitudinally at the mesoscopic scale it is essential to know the spatial extent of the stroke core. In this chapter we first establish optical coherence tomography (OCT) as a reliable identifier of the stroke core by analyzing signal attenuation and spatially correlating it with the infarct, determined by staining with triphenyl-tetrazolium chloride (TTC). We then introduce spatial frequency domain imaging (SFDI) as a mesoscopic optical technique that can be used to accurately measure the infarct spatial extent by exploiting changes in optical scattering that occur as a consequence of ischemic stroke. Additionally, we follow the progression of ischemia through the acute and sub-acute phases of stroke recovery using both OCT and SFDI and show a consistently high spatial overlap in estimating infarct location. The use of SFDI in assessing infarct location will allow longitudinal studies targeted at following functional recovery mechanisms on a mesoscopic level without having to sacrifice the mouse acutely.

### 3.2 Introduction

In ischemic stroke, a reduction or complete loss in blood supply to a region of the brain results in a cascade of events over a varied temporal scale of minutes (hyperacute) and hours (acute), to days and ultimately weeks (chronic)<sup>11,12,17</sup>. The region directly supplied by the occluded vessel sees the largest reduction in blood flow (20% of normal flow) and undergoes cellular death within minutes of an occlusion. This area of metabolically dead tissue is referred to as the core of the stroke. The region surrounding the core contains hypo-perfused tissue that is damaged but not yet dead<sup>14</sup>. This peripheral area that represents salvageable tissue is called the penumbra in the acute phase or the peri-infarct region in the chronic phase. When properly managed with timely interventions, the penumbra can be saved before the core expands into it<sup>125–127</sup>. In the chronic phase, the peri-infarct undergoes significant spontaneous reorganization and restoration that results in functional and behavioral recovery<sup>4,5</sup>.

Preclinical animal models provide a great tool to study the structural and functional consequences of ischemic stroke<sup>69,97,98</sup> and are used extensively to enhance our understanding of stroke recovery mechanisms<sup>44,45,78,128</sup>. This understanding through experimental research goes hand-in-hand with the advancements seen in optical imaging techniques. Laser speckle contrast imaging (LSCI) allows visualization of changes to relative cerebral blood flow (CBF) before and after stroke over a large field of view with relatively high spatial (10-100 μm) and temporal resolution (10-100 frames/sec)<sup>120,129,130</sup>. In the acute phase following occlusion, LSCI can be used to closely monitor tissue perfusion in the core and penumbra, as well as evaluate the effect of treatment on tissue

reperfusion and recovery. Optical coherence tomography (OCT) has been used to obtain absolute blood flow measures over several millimeters with micron-level resolution<sup>131–133</sup> and two-photon microscopy is capable of imaging cellular-level information down to hundreds of microns below the brain surface<sup>134</sup>. Functional neuroimaging methods are valuable for monitoring stroke recovery processes<sup>7,23,27,135</sup>.

A number of studies have followed neuronal and vascular recovery mechanisms longitudinally in the peri-infarct<sup>78,128</sup>. These studies typically rely on CBF as a metric to define either the stroke core or the peri-infarct region. While CBF has been validated as a reliable metric in determining the extent of tissue damage, the CBF cut-off values for the core and peri-infarct vary across different studies<sup>136–138</sup>. In addition, CBF obtained from LSCI is a relative measure that can depend on the instrumentation and experimental parameters. Histological staining of brain tissue with triphenyl-tetrazolium chloride (TTC) has been well-established as a gold standard to identify the stroke core as TTC can differentiate between metabolically active and inactive tissue<sup>139</sup>. However, the drawback with TTC staining is that it needs to be performed within 72 hours of the stroke in order to be a reliable measure of the infarct and requires the animal to be sacrificed, thereby not allowing valuable longitudinal studies.

Traditionally, the stroke core has been evaluated longitudinally with diffusion weighted imaging (DWI), which is a type of magnetic resonance imaging that measures the apparent diffusion coefficient (ADC) of water within the brain tissue<sup>140,141</sup>. Perfusion deficits, which lead to metabolic energy failure, result in cellular swelling in the early hours after ischemic stroke<sup>142,143</sup>. Cellular swelling results in a decrease in ADC, which is

measured as an increase in the DWI signal. Although DWI is a widely accepted method, it is hard to implement due to high cost and space constraints related to MRI instrumentation. It is expected that cellular and intracellular organelle swelling also changes the optical scattering coefficient within the brain tissue, as has been observed with OCT<sup>144,145</sup>. Tissue scattering or light attenuation obtained from microscopy techniques, such as OCT, are optical analogs to DWI and are expected to be reliable metrics of the stroke core that can help guide longitudinal monitoring of functional recovery following stroke, as suggested in recent publications<sup>144,145</sup>.

OCT typically captures micrometer-resolution three-dimensional images across a few millimeter (1-3 mm) fields of view from within optically scattering samples such as the brain. For monitoring the stroke core in animal models, it is advantageous to compliment the OCT measures with mesoscopic resolution over larger fields of view (6-10 mm) that cover the entire mouse cortex. Spatial frequency domain imaging (SFDI) is a wide-field diffuse optical reflectance-based technique that can quantify sample absorption ( $\mu_a$ ) and reduced scattering ( $\mu_s'$ ) coefficients<sup>146,147</sup>. While SFDI has been used to study the hemodynamic response during ischemic stroke<sup>148</sup>, it has not been used in the context of longitudinally mapping the stroke core. This approach is useful for combining stroke lesion identification with other wide-field imaging such as calcium signals or intrinsic optical signal imaging. In this chapter we present SFDI as an optical technique to accurately measure the spatial extent of the stroke core. We follow the optical evolution of the stroke core before and after the onset of stroke and at various time points until 72 hours post-stroke. We first validate that OCT signal attenuation can reliably predict the stroke core by

comparing to TTC staining. SFDI scattering is then validated alongside OCT signal attenuation, following which SFDI is validated against TTC staining.

### 3.3 Methods

#### 3.3.1 *Instrumentation*

A schematic of our imaging setup, used for producing a stroke with photothrombosis and then monitoring it with spatial frequency domain imaging, is shown in Figure 3.1. Our combined laser speckle contrast imaging (LSCI) and photothrombosis setup for optimized induction of photothrombotic stroke has been described in detail previously in Chapter 2<sup>96</sup>.

In order to induce an occlusion in a distal pial branch of the middle cerebral artery (MCA) and simultaneously monitor changes to cerebral blood flow (CBF), the photothrombosis setup was coupled together with the LSCI system. Briefly, LSCI is used to image CBF by illuminating the surface of the brain with a 785 nm laser diode (LP785-SAV50, Thorlabs) and imaging the back scattered light using a CMOS camera (Basler acA2040-90um NIR). A 785 nm band pass filter, with a bandwidth of 10 nm, along the detection path was used to spectrally restrict the light. Additionally, in order to minimize specular reflections and optimize the speckle size, a linear polarizer and iris were placed along the imaging path respectively. The pupil diameter of the iris was adjusted such that the speckle to pixel size ratio was 3.2 as calculated from the spatial cross-correlation of the speckle pattern obtained from a static scattering sample. Speckle images were acquired with a 5 ms exposure time at 40 frames per second. To perform photothrombosis via photoactivation of a photosensitive dye, Rose Bengal, the system contains a 520 nm laser diode in an epi-

illumination configuration. The laser spot size was designed to obtain a lateral resolution of 6  $\mu\text{m}$  in diameter with an axial point spread function of 104  $\mu\text{m}$ . A beam splitter along the imaging path allows visualization of the laser spot on the scientific CMOS camera (Hamamatsu ORCA-Flash4.0 V3). A 470 nm LED (not shown in the schematic) was used to illuminate the surface vasculature in order to position the laser spot on the target pial vessel. A 640 nm dichroic beam-splitter was used to split the near-infrared and visible light and a 650 nm short pass filter was used to prevent bleed through from the 785 nm laser diode used for LSCI. The imaging setup includes a 2X objective for a field of view of 5.6 mm x 5.6 mm for the CMOS (LSCI camera) and 6.5 mm x 6.5 mm for the sCMOS.

Instrumentation for spatial frequency domain imaging (SFDI) has been added to this imaging setup to allow estimation of tissue optical properties including the absorption ( $\mu_a$ ) and reduced scattering coefficients ( $\mu_s'$ )<sup>149</sup>. A 530 nm LED was used for SFDI so that the absorption images would be representative of total hemoglobin concentration without confounding impacts of hemoglobin oxygenation. A digital micromirror device (DMD) (LC4500, Keynote Photonics) along the illumination path is used to spatially modulate the light at the desired frequencies. An achromatic lens is placed after the DMD along the illumination path to magnify the image from the DMD onto the sample. Additionally, a polarizer is placed along the illumination and imaging paths in order to cross polarize the light and reduce specular reflections. A mirror along the illumination path is placed after the polarizer to direct and center the light beam on the mouse brain. The reflected light is captured with the sCMOS camera.

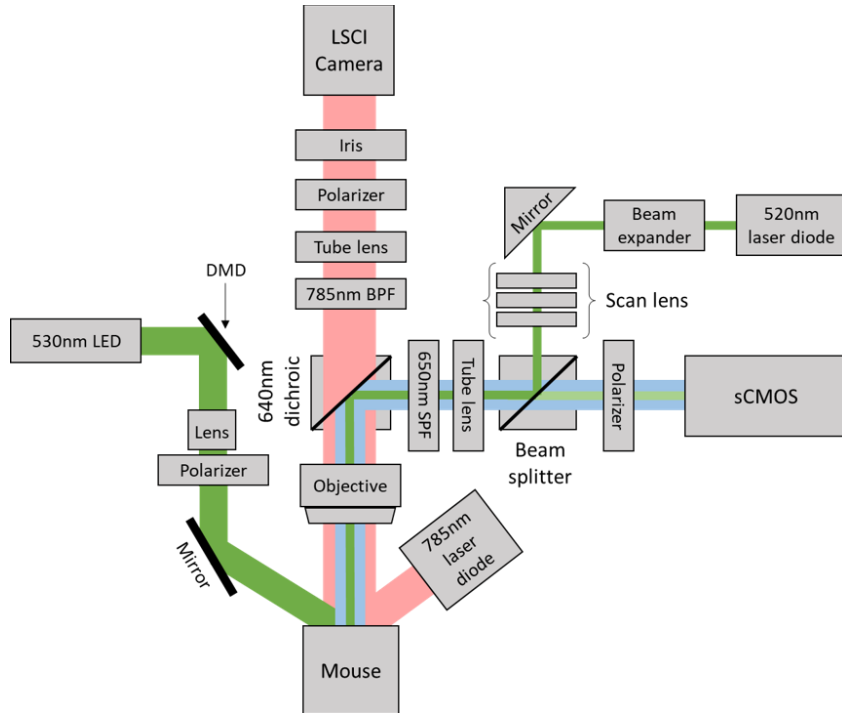


**Figure 3. 1: Schematic of the imaging setup with combined photothrombosis, laser speckle contrast imaging, and spatial frequency domain imaging**

### 3.3.2 Surgical procedure

All animal procedures were approved by the Boston University Institutional Animal Care and Use Committee and were conducted following the Guide for the Care and Use of Laboratory Animals. All mice used in this study were adult wildtype C57Bl6 at approximately 15 weeks old. A total of 7 mice were used in the study; 4 mice were sacrificed at 24 hours after stroke and 3 mice were sacrificed at 72 hours after stroke for histological analysis.

Our surgical procedure has been described previously in Chapter 2<sup>96</sup>. Briefly, 4 hours prior to the start of surgery, dexamethasone was administered intraperitoneally in order to minimize cerebral edema during and after surgery. Isoflurane was used to anesthetize the mice (3% at induction and 1-1.5% for maintenance with 1L/min oxygen),

while body temperature was maintained at 37°C with a homeothermic blanket. Respiratory rate and toe pinch were used to monitor the depth of anesthesia throughout the surgical procedure. After incision of the scalp, a craniotomy was performed on one hemisphere of the brain in order to remove the skull. A half-skull-shaped curved glass<sup>150</sup> (modified from Crystal Skull, LabMaker, Germany) was used to cover the surface of the brain and then sealed with dental acrylic. To allow head-fixation of the mice under the imaging system, an aluminum head post was attached to the intact skull of the other hemisphere. After a two week recovery period, mice were trained over approximately 10 days to remain head-fixed for up to 1 hour. All experiments are done in awake head-fixed mice.

### 3.3.3 *Focal cerebral ischemia*

Optimized photothrombosis was performed as described in the previous chapter. A modified version of photothrombosis previously described by Watson et al. (1985)<sup>95</sup> was used to perform an occlusion of a distal pial branch of the middle cerebral artery (MCA). The 520 nm laser diode was tuned to a post-objective focal power of 0.6 mW prior to the start of photothrombosis. The surface vasculature was visualized under the 470 nm LED and the mouse was positioned so that the laser spot is directly over the target vessel. Ten minutes of baseline CBF were obtained, following which the mouse was lightly anesthetized for retroorbital injection of Rose Bengal (100 µl, 15 mg/ml in saline). The active use of isoflurane is limited to under one minute, which includes induction and injection, after which the mouse is immediately taken off isoflurane and allowed to recover. Recovery of the mouse was determined as a return to baseline CBF and exhibiting natural

behavior such as whisking. Our optimized photothrombosis protocol uses real-time laser speckle contrast feedback to guide the duration of illumination in order to minimize unwanted photodamage to the surrounding vasculature as a consequence of laser illumination. The 520nm laser was turned on until the target vessel was occluded, as indicated by a disappearance of the branch in real-time LSCI, and then decreased to half the power for two minutes. Real-time spatial laser speckle contrast was calculated from the raw images captured using software from The Functional Optical Imaging Laboratory at The University of Texas at Austin<sup>108</sup>. The mouse was monitored for 1 hour under the LSCI setup and, if the branch reperfused during this time, the laser was turned on again until subsequent occlusion. Additionally, as previously described in Chapter 2, two collateral branches were also targeted in order to obtain a stable infarct.

### *3.3.4 Optical coherence tomography*

In order to validate the scattering maps obtained from SFDI, we used optical coherence tomography (OCT). OCT signal attenuation has been used and validated previously as a technique to obtain the spatial extent of the stroke core<sup>144,145</sup>. OCT angiograms of the vasculature were obtained at pre-stroke, 1 hour, 2 hours, 4 hours, 24 hours, and 72 hours after photothrombosis. A spectral domain OCT system (1310 nm center wavelength, bandwidth 170 nm, Thorlabs) was used for obtaining angiograms as previously described<sup>117</sup>. A 5X objective (Mitutoyo) was used to obtain a field of view of 2.5 mm x 5 mm. The region was scanned with 500 x 1000 pixels to obtain a pixel size of 5  $\mu\text{m}$  x 5  $\mu\text{m}$ . OCT angiograms were obtained using a repeated complex OCT B-scan signal. Each OCT

image was repeated 5 times to obtain an average of 5 angiograms. The average of the raw signal was processed offline using a custom MATLAB code to extract the OCT signal attenuation. The signal intensity was calculated as the log of the average of the two repeated B-scans. The signal was spatially down-sampled in the XY-direction to minimize speckle noise by taking an average of pixels in the nearest 4x4 neighborhood. The OCT attenuation, defined as the slope of signal decay with respect to depth, was obtained by performing a linear fit to each pixel in the XY-direction. A 450  $\mu\text{m}$  region (in depth) was selected, starting at approximately 100  $\mu\text{m}$  below the glass, to perform the fit. Figure 3.2 shows an outline of OCT analysis where Figure 3.2a shows an OCT angiogram. Figure 3.2b shows an XZ profile of the red line indicated in the left angiogram and the slope of signal decay from two points, one within the stroke (blue) and one outside the stroke (green). Figure 3.2c shows OCT attenuation at each XY pixel where the darker pixels have a larger slope due to faster signal decay, depicting the stroke core.

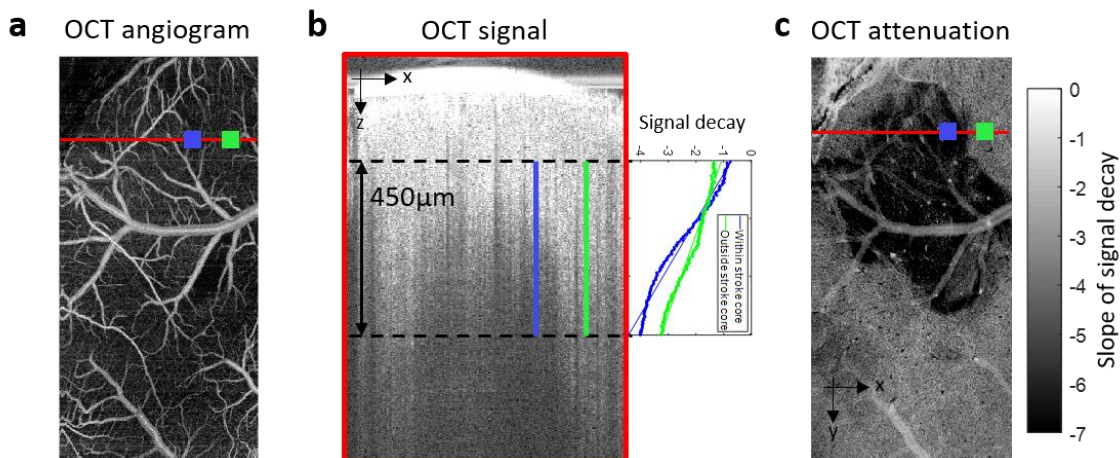


**Figure 3.2: OCT analysis for signal attenuation**

(a) Example XY profile of an OCT angiogram from which a signal attenuation map is derived. (b) Left: XZ profile of a single line scan (red line in left panel) with 450  $\mu\text{m}$  segment used to obtain signal attenuation. Right: OCT signal decay vs depth taken from

two regions of interest, blue region lies within the stroke core and green region lies outside the stroke core. (c) XY map of OCT attenuation at 2 hours after stroke.

### 3.3.5 Spatial frequency domain imaging

SFDI uses spatially varying sinusoidal patterns, which are projected onto a sample surface, and the reflected light is detected with a camera. The spatial modulation transfer function (sMTF), which contains optical property information, is obtained through a demodulation and calibration procedure performed on the reflected light. The sMTF is then calibrated with a silicone phantom to obtain the diffuse reflectance, which is then compared to the results obtained from Monte Carlo simulations of photon transport to determine absorption and reduced scattering. The instrumentation for SFDI is previously described in section 3.3.1 and was adapted from Applegate et al. (2020)<sup>149</sup>. A schematic of just the SFDI setup is shown in Figure 3.3a. Optical properties of the brain were obtained at pre-stroke, 1 hour, 2 hours, 4 hours, 24 hours, and 72 hours after photothrombosis. The DMD in the illumination path spatially modulates the light at six spatial frequencies (0, 0.05, 0.1, 0.2, 0.4, 0.5 mm<sup>-1</sup>) and each sinusoidal pattern is projected at three phases (0, 120, and 240 deg). The reflected light is captured with a sCMOS camera with a FOV of 6.5 mm x 6.5 mm and is synchronized with the mirror display and LED. Total acquisition time for 6 frequencies, at 3 phases, repeated 5 times is ~5 min or ~3 s/frame. In addition to imaging the awake mice, a silicone phantom with known optical properties is imaged with the same protocol to calibrate for system errors. The images obtained are processed offline using MATLAB following previously established protocols<sup>146,151</sup> to obtain a pixel-by-pixel map of the tissue optical properties. Demodulated intensity at each spatial frequency were

calculated using:

$$M_{AC}(x_i, f_x) = \frac{2^{1/2}}{3} [(I_1 - I_2)^2 + (I_2 - I_3)^2 + (I_1 - I_3)^2]^{1/2}$$

where  $M_{AC}$  is the demodulated AC component and  $I_1$ ,  $I_2$ , and  $I_3$  are the reflected intensity images at the three phases for each spatial frequency.  $M_{AC}$  images were then calibrated to the reference phantom to obtain the diffuse reflectance. Measurements were analyzed using a lookup table (LUT) from Monte Carlo simulations<sup>152</sup>, where the reflectance patterns are recorded for various values of  $\mu_a$  and  $\mu_s'$  with a point source as an input. The simulated spatial frequency dependent reflectance can be obtained by convolving the incident sinusoidal source pattern with the reflectance pattern obtained from the point source. We have assumed the anisotropy factor  $g=0.9$ . A two frequency LUT was generated from the simulation results for spatial frequencies of  $0 \text{ mm}^{-1}$  and  $0.4 \text{ mm}^{-1}$ . While we obtained data for a range of spatial frequencies, only two spatial frequencies were used to generate the LUT and analyze the results. The spatial frequency used for analysis was chosen based on the orthogonality of the LUT, minimal coupling between  $\mu_a$  and  $\mu_s'$  in the LUT, and where most of the diffuse reflectance data points from the sample fell within the range of the LUT<sup>153</sup>. This corresponded to the LUT of spatial frequencies  $0 \text{ mm}^{-1}$  and  $0.4 \text{ mm}^{-1}$ . Figure 3.3b shows a flowchart of the SFDI data processing method. The top panel shows raw intensity images with planar (left) and sinusoidal (right) spatial patterns. The middle panel shows the diffuse reflectance images after AC demodulation of the three phases for each frequency and the bottom panel shows the absorption and reduced scattering coefficients obtained from the Monte Carlo LUT. Some cross-talk is observed in the extracted absorption and scattering images as seen by a decreased  $\mu_a$  in the large blood vessels, which

we expect to have higher absorption. The data points corresponding to the large vessels fall outside the range of the LUT, where there is coupling between  $\mu_a$  and  $\mu_s'$ , therefore not allowing accurate estimation of the optical properties. Figure 3.3c shows a visualization of the LUT and data points. The data points that fall outside the LUT are plotted in red along with their corresponding spatial location on the  $\mu_s'$  image to more clearly indicate the points in the image for which we do not trust the estimated optical properties. We are primarily interested in changes to scattering within the parenchyma following stroke, which we can see falls within the LUT as shown by the green points in Figure 3.3c. Figure 3.3d shows the reduced scattering coefficient in  $\text{mm}^{-1}$  before stroke and at three time points after stroke in the top panel. The bottom panel shows the percent change in reduced scattering coefficient compared to pre-stroke, where the stroke core is clearly highlighted due to increased scattering.

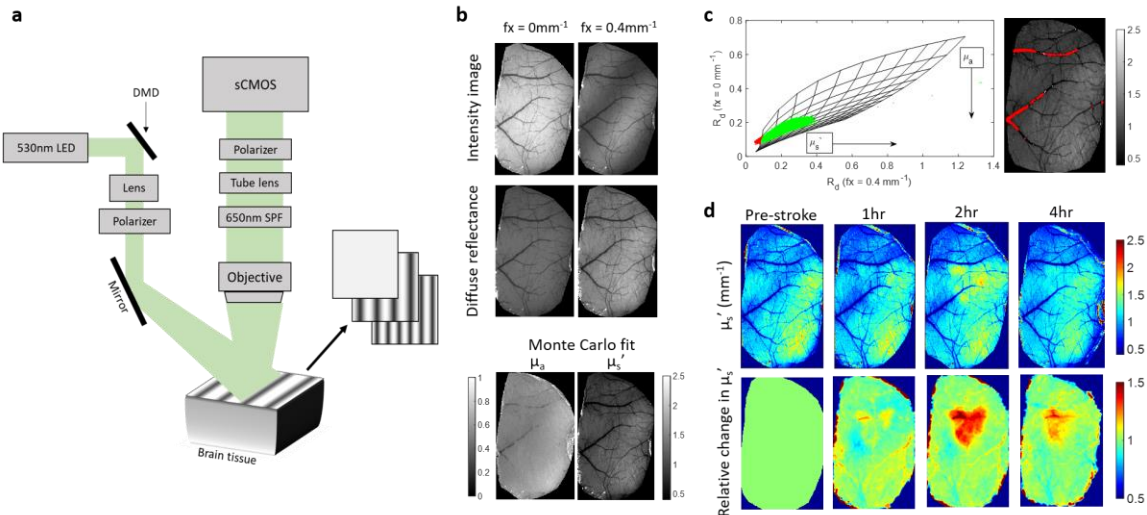


**Figure 3. 3: SFDI instrumentation schematic and analysis pipeline**

(a) Imaging schematic of the spatial frequency domain imaging (SFDI) setup. (b) SFDI data processing flowchart: Intensity image at two frequencies (three phase images per frequency) are demodulated and calibrated with reference phantom images (diffuse reflectance) and then fit to a lookup table generated from Monte Carlo simulations to obtain

$\mu_a$  and  $\mu_s'$ . (c) Top row: Reduced scattering coefficient before and after photothrombosis, bottom row: percent change from baseline reduced scattering coefficient after photothrombosis.

### 3.3.6 Histological analysis

We performed histological staining with triphenyl-tetrazolium chloride (TTC) to assess the stroke core at 24 hours in 4 mice and 72 hours in 3 mice. TTC has been well established as a technique for identifying infarcted tissue due to stroke by differentiating between metabolically active and inactive tissue<sup>139</sup>. After the final imaging time point mice were deeply anesthetized with isoflurane, decapitated, and whole brain extracted for TTC staining. The intact brain was incubated at 37°C for 30 minutes in 2% TTC in phosphate-buffered saline. Images were acquired immediately after staining under a surgical microscope.

### 3.3.7 Data analysis

All data were analyzed offline using custom MATLAB codes. First, the OCT and SFDI data were analyzed individually as described in the above sections. Then, SFDI scattering and OCT attenuation image from all time points of each animal were registered to the pre-stroke SFDI scattering image of the same animal. Once registered, the percent change in SFDI scattering and OCT signal attenuation were calculated from their respective pre-stroke values. In order to validate the spatial overlap between the stroke core as determined by SFDI and OCT we used the Dice coefficient, which is a statistic metric used to determine the similarity of two samples<sup>154–156</sup>. To calculate the overlap, a stroke core

outline was semi-automatically drawn using built in MATLAB contour function, activecontour, for corresponding SFDI and OCT percent change images. The active contours technique is an iterative region-growing image segmentation algorithm that uses initial curves that are user specified after which the algorithm evolves the curves towards the object boundary. Each image had a user defined curve positioned within the core region. Each contour image was then converted into a binary image and the Dice coefficient built in function was used to assess the similarity between the two binary images. A total of 7 animals were used to calculate overlap between SFDI and OCT at all time points except 72 hours, where 3 animals were used. In addition to estimating the spatial overlap with OCT, SFDI scattering was also validated with TTC staining using the same Dice coefficient procedure. Here, 5 animals were used ( $n=2$  at 24 hours and  $n=3$  at 72 hours) as 2 of the 4 animals sacrificed at 24 hours did not show any distinct TTC abnormality. The green channel from the TTC image was used to register vascular landmarks from TTC with SFDI before performing similarity analysis. Quantitative results are expressed as mean and standard deviations.

### 3.4 Results

#### 3.4.1 Increased OCT signal attenuation in a mouse photothrombosis stroke model is a reliable predictor of the stroke core

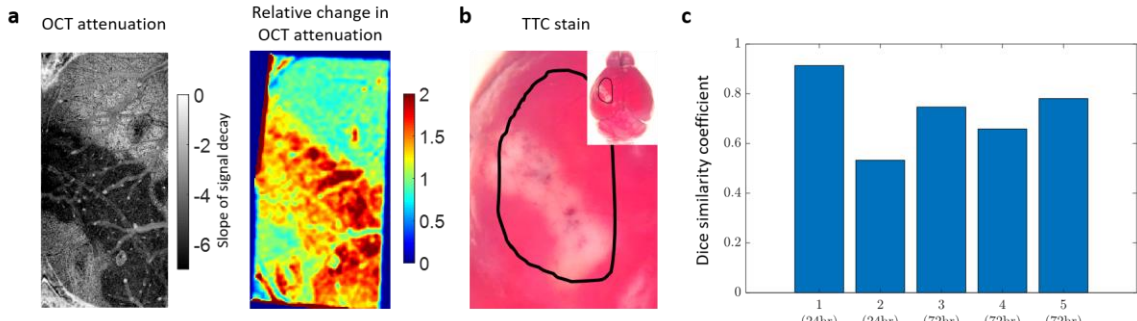


**Figure 3.4: Spatial overlap of OCT attenuation and TTC staining**

(a) Left: OCT attenuation map at 72 hours shown as the slope of signal decay, right: percent change in OCT attenuation at 72 hours compared to pre-stroke. (b) TTC stain at 72 hours after stroke, black outline indicates cranial window location. (c) Spatial overlap shown by Dice similarity coefficient for five mice.

Prior studies have shown that OCT signal attenuation increases in the area of focal cerebral ischemia<sup>144,145</sup>. They have also shown the spatial expansion of signal attenuation as ischemia progressed over time and suggested that the infarcted tissue may be identified with these optical signals. However, OCT signal attenuation has not been statistically compared against the gold standard TTC stain for infarcted tissue. Here, we used the OCT XY-attenuation map with the co-registered TTC map to determine spatial overlap. Figure 3.4a shows the spatial OCT attenuation map expressed as a slope of signal decay in the left panel. The right panel shows the percent change in OCT signal compared to the pre-stroke signal. Figure 3.4b shows the TTC stain and the black outline corresponds to the cranial window location. The TTC image at the corresponding time point was co-registered to the OCT image and the dice coefficient was used to estimate overlap. There was a strong

overlap between OCT and TTC with a similarity mean and standard deviation of  $0.73 \pm 0.13$ . Figure 3.4c shows the similarity coefficient for individual animals ( $n=5$ :  $n=2$  at 24 hours,  $n=3$  at 72 hours). Animals that did not show any apparent tissue infarct at 24 hours were excluded from the analysis ( $n=2$ ).

### *3.4.2 Reduced scattering coefficient obtained from SFDI reliably predicts increased signal attenuation seen with OCT following stroke*

While OCT provides microscopic information over millimeter fields of view in the brain, for monitoring the stroke core in animal models, it is advantageous to compliment the OCT measures with mesoscopic resolution over larger fields of view. This approach is useful when lesion identification is combined with other modalities such as calcium imaging or intrinsic optical signal imaging for neural and vascular dynamics respectively. Spatial frequency domain imaging (SFDI) is a wide-field diffuse optical technique that can separate sample absorption ( $\mu_a$ ) and reduced scattering ( $\mu_s'$ ) coefficients. Cellular swelling in the acute time points following stroke has been well established and this swelling leads to an increase in optical scattering<sup>157,158</sup>. Therefore, SFDI is potentially a great tool to longitudinally monitor the spatial progression of ischemia.

In order to validate SFDI as a technique that reliably predicts the stroke core, we can first verify that the reduced scattering coefficient obtained from SFDI spatially overlaps with OCT signal attenuation. Figure 3.5 shows an example mouse with side-by-side comparison of SFDI and OCT. Figure 3.5a shows the percent change in reduced scattering coefficient from SFDI (top row) and the percent change in co-registered OCT

attenuation (bottom row) at various time points in the acute and sub-acute phases of stroke recovery. Qualitatively we observe good spatial overlap between the regions that show changes from pre-stroke at all the time points imaged after stroke. Figure 3.5b shows the corresponding TTC stain at 72 hours after stroke.

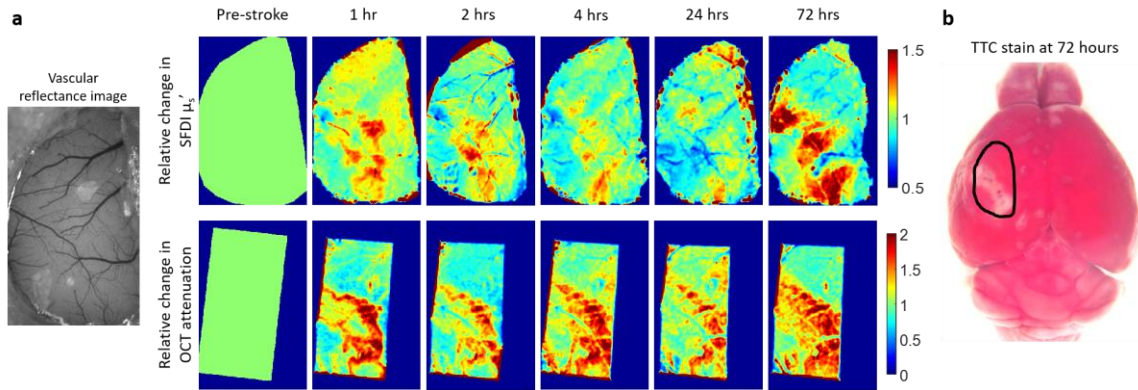


**Figure 3.5: Signal attenuation comparison between SFDI and OCT**

(a) Percent change in reduced scattering obtain from SFDI (top row) and percent change in OCT signal attenuation (bottom row) from one example mouse at 1hr, 2hr, 4hr, 24hr, and 72hr after stroke. (c) TTC staining at 72 after stoke, black outline indicates cranial window location.

Quantitative analysis of spatial overlap also shows high similarity between OCT signal attenuation change and SFDI scattering change at all the time points after stroke except at 24 hours. Figure 3.6 shows the workflow and analysis for quantifying the Dice similarity coefficient. Figure 3.6a shows an example SFDI and OCT percent change image, which is low-pass filtered, using a 2-D Gaussian filter with a standard deviation of 2, and automatically contoured by selecting a representative region of the stroke core. Figure 3.6b shows the low-pass filtered and contoured image of the same example. The contours are then converted to a binary image and assessed for similarity. Figure 3.6c shows the mean Dice similarity coefficient and standard deviation for all mice ( $n=7$  for the first 24 hours

and n=3 for 72 hours). All time points, except 24 hours, show a larger than 70% overlap between SFDI scattering and OCT attenuation changes.

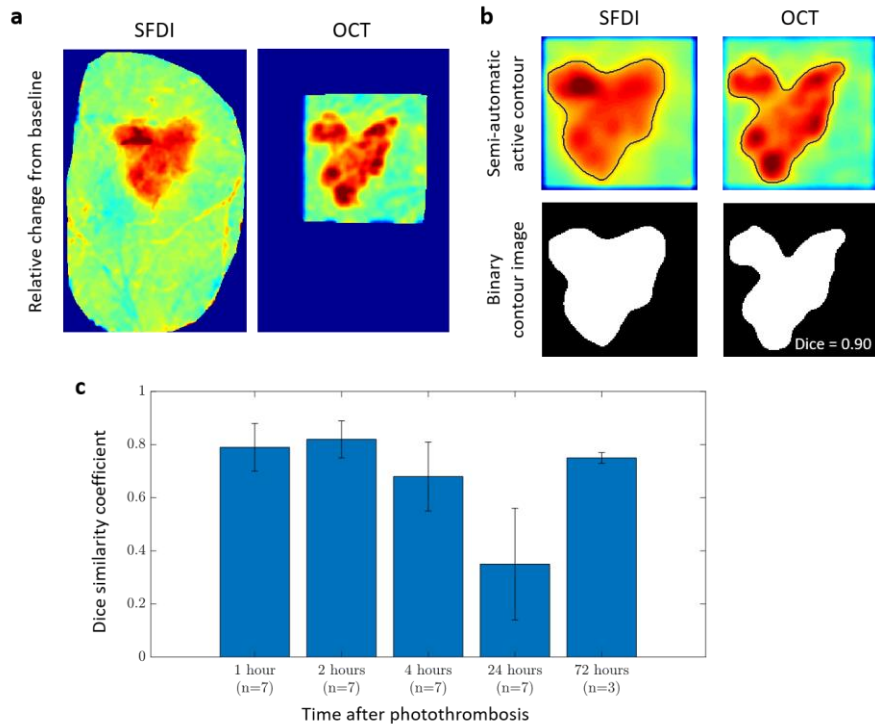


**Figure 3.6: Dice similarity coefficient workflow and calculation for stroke overlap**  
 (a) Example SFDI and OCT percent change images at 2 hours after stroke. (b) Top row: Semi-automatic contour outline of stroke core, bottom row: binary image from contour to calculate the dice similarity coefficient. (c) Dice similarity coefficient for SFDI and OCT stroke core overlap at each time point following stroke represented as mean and standard deviation.

### 3.4.3 Scattering increase as determined from SFDI following phot thrombotic stroke is a reliable predictor of the stroke core

Similar to validating OCT attenuation against TTC staining we validated SFDI with TTC staining as well in order to reveal the true stroke core. As described in section 3.4.1, we co-registered the TTC image with the SFDI percent change image at the corresponding time points and performed the similarity analysis (Figure 3.7). Figure 3.7a shows an example

SFDI percent change image (left panel) that has been low-pass filtered and core outlined (right panel), and Figure 3.7b shows the corresponding TTC image. The dice similarity coefficient for five animals is shown in Figure 3.7c. The mean spatial overlap was 0.74 with a standard deviation of 0.07. From this we show that increased scattering observed from SFDI is a reliable analog for measuring the stroke core.

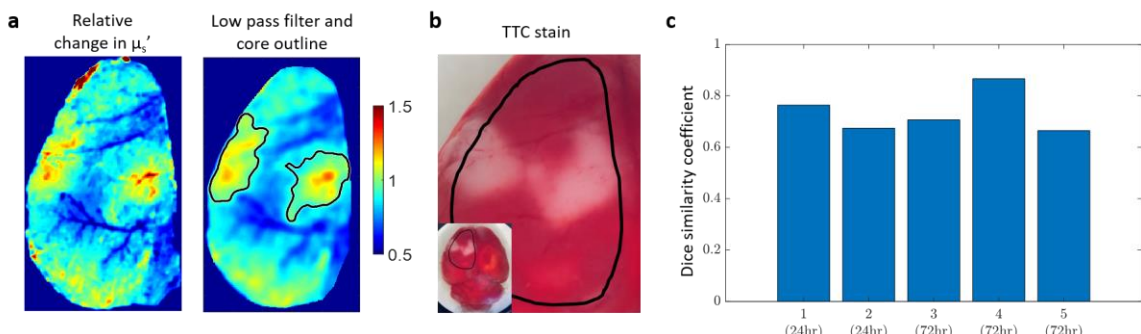


**Figure 3.7: SFDI spatial overlap with TTC staining**

(a) Example percent change image (left) with corresponding low-pass filtered and contoured image (right). (b) TTC stain at the corresponding time point as in (a) (24 hours after stroke). (c) Dice similarity coefficient of spatial overlap for five mice.

### 3.5 Discussion

In this chapter we have demonstrated the use of scattering from spatial frequency domain imaging (SFDI) as an optical measure of identifying the stroke core. We first demonstrated the accuracy of OCT signal attenuation in estimating the stroke core by comparing it to the well-established TTC stain. We then compared the spatial overlap between SFDI scattering changes and OCT signal attenuation, following which we compared SFDI to TTC staining. While SFDI has been widely used for various biological and clinical applications<sup>147,148</sup>, it has not been previously used to estimate and follow the progression of the stroke core longitudinally.

Following the stroke core is an essential component of monitoring stroke progression in both the acute and chronic phases of stroke recovery. In the acute phase following stroke, DWI in the clinical setting is used to assess the extent of infarct and determine the appropriate treatment protocols, such as the administration of tissue plasminogen activator or clot thrombolysis for recanalization, to prevent the infarct from expanding and also to monitor the effects of such treatments on infarct outcome<sup>125,127,159</sup>. In the pre-clinical research setting, acute monitoring is valuable to understand the pathophysiological mechanisms that impact tissue outcome and also assess the feasibility of interventions that improve tissue outcome<sup>79,160</sup>. Most of these interventions are targeted towards the penumbra region of the stroke as it is comprised of salvageable tissue that is compromised but not yet dead<sup>161</sup>. If left alone, the stroke core expands into the penumbra and results in a larger infarct, but if salvaged the penumbra can be returned to normal functioning healthy tissue. These studies require monitoring the infarcted tissue at frequent intervals in not only the acute phase but also chronically to truly determine long-term benefits, which require the mouse to not be sacrificed for TTC staining to determine infarct size. In addition to acute studies, longitudinal studies are valuable to understand long-term recovery mechanisms that occur both spontaneously as well as enhanced through rehabilitation<sup>3,5</sup>. These mechanisms, which primarily occur in the peri-infarct region, are seen as changes to the vascular response to brain activity in fMRI and fNIRS studies<sup>8,9</sup>. Apart from observations made in the clinical settings, animal models are used extensively to understand the structural and functional changes that lead to the observed behavioral recovery<sup>45,123,162</sup>. This requires longitudinal monitoring from days to weeks and even

months, where optical measures of the stroke core could be very useful.

Here, we have validated that OCT and SFDI are reliable optical measures of the stroke core when compared to TTC staining, thereby allowing longitudinal studies. TTC, or triphenyl-tetrazolium chloride, is an indicator used to determine ongoing cellular energy metabolism. Due to its ability to detect tissue viability, by differentiating between metabolically active or inactive tissue, it is used extensively in pre-clinical stroke research to identify damaged tissue and evaluate infarct size due to the stroke<sup>139</sup>. A drawback of TTC staining is that it needs to be performed within 72 hours of stroke induction, with 24 hours after stroke being the most commonly used time point<sup>163</sup>. The reason for this is that TTC at later time points is confounded by the robust inflammatory response that results due to stroke and is typical of the secondary or delayed phase of the response to ischemia. This response involves the migration of inflammatory cells towards the stroke core, which play an important role in the post-ischemic recovery period. With the presence of these active cells in the stroke core and peri-infarct region, TTC staining is no longer able to accurately differentiate metabolically dead tissue as these active cells would show viable tissue and mask the true region of inactive tissue. Therefore, TTC staining has to be performed within 72 hours after stroke induction, which is before inflammatory cells have established themselves in the stroke affected region, and is therefore a serious limitation when designing long-term experiments. The mechanisms that result from stroke that lead to metabolically dead tissue present themselves as optical changes in tissue properties that can be imaged<sup>142,144,145</sup>. We have shown that OCT signal attenuation and SFDI increased scattering at 24 and 72 hours after stroke have on average greater than 70% overlap with

metabolically dead tissue that was identified with TTC staining. Therefore, by using OCT or SFDI we can capture the spatial extent of the infarct and identify the stroke core and peri-infarct regions while still being able to perform longitudinal stroke experiments.

In addition to imaging at the time points when TTC would have been done, we can use the same imaging techniques to monitor the progression of ischemia throughout the acute phase and sub-acute phase at various time points as the progression can be very dynamic and sometimes biphasic in nature<sup>164</sup>. In the early hours following stroke it has been hypothesized that cellular and organelle swelling occur due to metabolic dysfunction, which leads to intracellular water accumulation. This presents itself as changes in optical properties of the tissue, which begin as early as 30 minutes after stroke induction. We have shown changes in optical scattering at 1 hour, 2 hours, 4 hours, 24 hours, and 72 hours after stroke induction. We observed greater than 70% overlap in the spatial extent of optical changes between OCT and SFDI at all the time points after stroke except 24 hours, which showed low overlap and high variability. This was due to the fact that scattering changes were inconsistent in both OCT and SFDI across all animals at 24 hours. One explanation for this inconsistency is the effect of reperfusion time on scattering changes and tissue outcome. Evidence has indicated that ischemic hyperintensity seen with DWI in rats can be reversible or biphasic if reperfusion is performed shortly after stroke induction<sup>160,165</sup>. Our photothrombosis model allows for spontaneous recanalization of the occluded vessel after the 1 hour photothrombosis session is complete. While this lends well to study the effect of reperfusion or reflects more naturally what happens in stroke, it introduces variability in the tissue response. The inconsistency seen with tissue scattering at 24 hours

can be explained when time to reperfusion following occlusion is taken into consideration. Animals that showed reperfusion within 4 hours, assessed through laser speckle imaging, showed more inconsistent scattering at 24 hours compared to animals that reperfused after 4 hours or did not reperfused at all. Reperfusion variability can also increase variability in tissue water content at 24 hours, as reperfusion can be associated with an oxidative injury, which can damage the blood brain barrier and lead to vasogenic edema. We speculate that the tissue water content, independent from cellular swelling, may be affecting our results at certain time points. However, the infarct had stabilized at 72 hours after stroke and proved to be a better determinant of tissue outcome. Though the point of this study was not to investigate the effects of reperfusion time on tissue outcome, we hope to address that question in future experiments.

This approach has a few limitations worth noting. The first is the difference in tissue depth interrogated by OCT and SFDI. Here, we are using a depth of 450  $\mu\text{m}$  in OCT, as larger depths provided more accurate fitting of the data while still remaining within gray matter. Additionally, due to a relatively small and heterogeneous infarct caused by photothrombosis compared to a stronger MCA occlusion, a larger depth provided better visualization of the changing infarct. SFDI on the other hand is integrating across a depth of approximately 300  $\mu\text{m}$ , as calculated from previously published papers<sup>151,166</sup>. We do not expect this difference in integrated tissue volume to have a notable effect on the estimated lateral spatial extent of the stroke core. A second limitation is the crosstalk observed between absorption and scattering in the large blood vessels. Blood is very absorbing at 530nm, making it challenging to accurately separate scattering from absorption as

visualized by its coupling in the LUT. While this can be overcome by using longer wavelengths we advocate for the use of 530nm for two main reasons, one is that we are interested in mapping scattering changes in the tissue and not the blood vessels, and two, 530nm is the isosbestic point of hemoglobin therefore allowing estimation of total hemoglobin concentrations, which is beneficial for studies monitoring changes in hemodynamics following stroke. Future studies can address this crosstalk issue by performing a series of phantom measurements in a physiologically relevant range of optical properties across different wavelengths to quantify the accuracy of the SFDI estimates.

In conclusion, we have validated the use of OCT as an optical indicator of the stroke core by computing signal attenuation and comparing against TTC. We have applied the use of SFDI as a mesoscopic measure of spatial changes to optical properties, which was validated against both OCT and TTC. Changes in optical scattering as determined by SFDI was a reliable optical analog of the stroke core thereby allowing longitudinal experiments without the need for sacrificing animals acutely.

## **CHAPTER FOUR – SIMULTANEOUS WIDE-FIELD OPTICAL IMAGING OF NEURAL ACTIVITY AND HEMODYNAMICS DURING STROKE RECOVERY**

### **4.1 Abstract**

Wide-field optical imaging is used in preclinical animal models to obtain simultaneous neuronal and hemodynamic measures to study neurovascular coupling in healthy and diseased brains. To accurately extract the true neuronal activity, the recorded fluorescence signal must be corrected for hemodynamic crosstalk. However, currently used correction methods have not yet been validated against a cellular structural fluorescent marker, which has overlapping excitation and emission spectra with that of the fluorophore. Additionally, these techniques have been developed for the healthy brain and do not account for changes in tissue optical properties and neurovascular uncoupling that are known to occur post-stroke. Therefore, there is a need to establish and validate an appropriate hemodynamic correction method that can be applied pre- and post-stroke. In this chapter we highlight the need for hemodynamic correction, implement commonly used techniques, and validate their accuracy. Our results suggest that previous techniques underestimate the required correction during the response phase of cortical activation from external stimuli due to deviations in pathlength factor used in the correction. To overcome this challenge, we use pathlength factors obtained from Monte Carlo simulations based on absorption and scattering coefficients extracted from SFDI, which improves the correction. Additionally, we use this technique to improve hemodynamic crosstalk correction post-stroke.

## 4.2 Introduction

Ischemia leads to the formation of a stroke core, which is localized to the irreversibly damaged tissue around the occlusion, and a peri-infarct zone, which is a region of compromised tissue with reduced blood supply that surrounds the stroke core<sup>2,11</sup>. While the tissue damage from stroke is localized mainly to the core, it has become clear that even such a focal injury can lead to global changes in functional connectivity and activation patterns<sup>8,9</sup>. BOLD fMRI studies have revealed that response measurements following stroke show pronounced alterations in amplitude and spatial extent of the BOLD signal in both the ipsilesional and in the contralateral hemispheres<sup>23,27,28</sup>. Additionally, studies assessing resting-state functional connectivity obtained with MRI (fc-MRI) have shown that intra- as well as inter-hemispheric connections are altered in the early acute phase of stroke in humans<sup>167,168</sup>. However, these functional neuroimaging studies represent the vascular response to brain activity and not the brain activity directly. It is still unclear if this vascular response is a true reflection of the underlying neuronal activity. Therefore, in order to better interpret human neuroimaging studies, we need to not only obtain simultaneous measures of both hemodynamic and neuronal activity but also obtain these measures on a macroscopic scale to understand the local and global alterations and their involvement in recovery<sup>169</sup>.

Optical technology to study neuronal and vascular activity *in vivo* in rodents has advanced immensely over the last few decades and has been used to understand healthy as well as diseased brains<sup>109,170,171</sup>. In stroke, functional imaging studies in preclinical animal models have also shown similar results related to changes in local and global activation

patterns compared to those in humans. Specifically, *in vivo* calcium fluorescence imaging studies have shown activation reorganization and functional remapping of the affected brain regions into the peri-infarct zone longitudinally<sup>44,45,47,123</sup>. Additionally, intrinsic optical signal imaging has been used to map changes to hemodynamics by assessing global changes using resting-state functional connectivity (RSFC) and also local changes through functional activation<sup>49,89</sup>. However, to the best of our knowledge, simultaneous neural and hemodynamic measures have not yet been obtained on a macroscopic and longitudinal scale to address their relationship and alterations to neurovascular coupling during stroke recovery.

Before evaluating neurovascular coupling after stroke, a few optical constraints need to be addressed. Through the process of neurovascular coupling, virtually all neuronal activity is accompanied by a hemodynamic response<sup>19,21</sup>, and due to the strong absorptive properties of blood in the visible range, this hemodynamic response contaminates the fluorescence signal. In order to accurately extract the true neuronal activity, the recorded fluorescence signal needs to be corrected for this hemodynamic crosstalk<sup>172–174</sup>. Prior efforts in healthy rodent brains have established two main correction algorithms: 1) the ratiometric method, where the fluorescence images are divided by the green diffuse reflectance images with the assumption that the absorption is the same at the excitation and emission wavelengths, and 2) the attenuation estimation method, where simultaneously obtained measures of oxy- and deoxy-hemoglobin are used to approximate the attenuation of the fluorescence signal at the excitation and emission wavelengths of the fluorescence probe, by estimating the absorption coefficient of hemoglobin at those wavelengths.

Method 2, the attenuation method, is a more rigorous way to correct for the hemodynamic confound as it does not assume the excitation and emission wavelength tissue properties to be the same. However, an in-depth analysis and validation of these methods has yet to be performed. Additionally, these correction methods have been developed for the healthy brain and do not account for changes in tissue optical properties and neurovascular uncoupling that are known to occur post-stroke. Therefore, there is a need to establish and validate an appropriate hemodynamic correction method that can be applied post-stroke.

In this chapter, we present the instrumentation necessary for simultaneous neural and hemodynamic measures, as has been done previously by others<sup>172</sup>. Additionally, we test commonly used hemodynamic correction techniques on a genetically encoded calcium probe, GCaMP, and validate their accuracy against the cellular structural fluorescent marker, GFP, which has overlapping excitation and emission spectra with those of GCaMP. First, we highlight the need for correction and compare previously used correction techniques. Next we introduce the use of spatial frequency domain imaging to obtain tissue optical properties and use those properties to improve existing correction techniques. Finally, we validate the correction post-stroke and address the changes in tissue optical properties that result post-stroke and how to account for those changes in the correction algorithm. Accurate correction for hemodynamic crosstalk in fluorescence data is vital for the correct interpretation of the changes to neuronal activity during stroke recovery.

### 4.3 Methods

#### 4.3.1 Animal preparation

All animal procedures were approved by the Boston University Institutional Animal Care and Use Committee and were conducted following the Guide for the Care and Use of Laboratory Animals. There were two groups of mice used in this study. The first group of mice were adult Thy1-GCaMP6f mice (Jackson Labs, strain code: 025393, C57BL/6J-Tg(Thy1-GCaMP6f)GP5.17Dkim/J)), that were used for simultaneous hemodynamic and neural activation experiments. Additionally, we used Thy1-EGFP mice (Jackson Labs, strain code: 007788, Tg(Thy1-EGFP)MJrs/J) to validate the hemodynamic crosstalk correction algorithm.

The surgical procedure used here was adapted from the previously described procedures<sup>96</sup>. Briefly, mice were injected with Buprenorphine subcutaneously 1 hour prior to the start of surgery. During surgery, mice were anesthetized with isoflurane (3% at induction and 1-1.5% for maintenance with 1L/min oxygen) and body temperature was maintained at 37°C. Respiratory rate and toe pinch were used to monitor the depth of anesthesia throughout the surgical procedure. After incision of the scalp, a round aluminum head post, 12 mm in diameter, was attached to the intact skull with dental acrylic. A craniotomy was performed on one hemisphere of the brain in order to remove the skull. A half-skull-shaped curved glass<sup>109</sup> (modified from Crystal Skull, LabMaker, Germany) was used to cover the surface of the brain and then sealed with dental acrylic. The craniotomy and glass procedure were repeated on the other hemisphere of the brain in order to create a bilateral cranial window implant. Recovery procedures were followed according to the

guidelines provided by Boston University. After a two week recovery period from surgery, mice were trained to remain head-fixed for up to 1 hour for approximately 10 days. All experiments are done in awake head-fixed mice.

#### *4.3.2 Hemodynamic and neural imaging instrumentation and acquisition*

Intrinsic optical signal imaging (IOSI) can be used to obtain changes in oxy-hemoglobin ( $\text{HbO}$ ) and deoxy-hemoglobin ( $\text{HbR}$ ) concentrations based on their oxygen-dependent optical absorption spectra<sup>175,176</sup> and fluorescence imaging of the genetically encoded calcium indicator, GCaMP, can be used to obtain changes in neural activity<sup>177</sup>. For IOSI, two light emitting diodes (LEDs) with center wavelengths at 530 nm and 625 nm (MXL3-C1, Thorlabs, X is the center wavelength) were used to sequentially illuminate the surface of the brain. The reflected images were collected by a sCMOS camera (Hamamatsu ORCA-Flash 4.0 V3) after passing through a 2X objective and the corresponding tube lens system. For fluorescence imaging, a 473nm laser diode (OptoEngine: MBL-N-473A laser, 473 nm, 600 mW, pumped, good beam, 5% power stability) was used to excite the GCaMP and a 500 nm long pass filter (FELH0500, Thorlabs) along the detection path blocked the excitation light and allowed only the emission spectrum of GCaMP to pass through to the camera. The excitation and emission spectra of GCaMP along with the absorption spectrum of hemoglobin are shown in Figure 4.1a.

Awake head-fixed mice were placed under the imaging setup and the surface of the brain was illuminated with a planar wave at each wavelength (473 nm, 530 nm, and 625 nm) sequentially with a frame rate of 15 frames per second, which amounts to 5 frames per

second per wavelength. The fluorescence and reflectance images were captured by the sCMOS camera as 16-bit 512 x 512 pixel images. For sensory stimulation, each trial consisted of a 5-second train of air puffs at 3 Hz delivered to the forelimb contralateral to the target hemisphere. We obtained 20 trials where each trial was obtained in a block-design fashion and consisted of 5 seconds of baseline, followed by 5 seconds of stimulation, followed by 20 seconds of recovery. Custom MATLAB scripts were used to synchronize and trigger the sequential LEDs, camera acquisition, and air puff stimulation.

#### *4.3.3 Image processing for hemodynamics*

We computed changes in oxy-hemoglobin (HbO) and deoxy-hemoglobin (HbR) from the acquired images using the modified Beer Lambert relationship<sup>176,178</sup>. Briefly, from the sequence of images acquired at 530 nm and 625 nm, we computed the change in optical density (OD) at each wavelength for each pixel as:

$$\Delta OD(\lambda, t) = -\ln \left[ \frac{I(\lambda, t)}{I_0(\lambda)} \right]$$

where,  $I(\lambda, t)$  is the reflected light intensity at wavelength  $\lambda$  and time  $t$ , and  $I_0(\lambda)$  is the baseline intensity (mean of the full time-course for resting state and first 5 seconds of every trial for sessions with stimulation). Using the modified Beer Lambert law:

$$I(\lambda, t) = I_0(\lambda) \exp[-\Delta \mu_a(\lambda, t) L(\lambda)]$$

where  $\Delta \mu_a(\lambda, t)$  is the change in optical absorption coefficient and  $L(\lambda)$  is the wavelength-dependent mean free path length in the tissue as obtained previously by others. After obtaining the changes in absorption coefficients at each pixel for each wavelength, we

calculated changes in HbO and HbR for each pixel at each time using a set of two equations and the molar extinction coefficients of HbO and HbR:

$$\Delta\mu_a(\lambda, t) = \epsilon_{HbO}(\lambda)\Delta HbO(t) + \epsilon_{HbR}(\lambda)\Delta HbR(t)$$

Total hemoglobin HbT was calculated as a sum of HbO and HbR.

#### *4.3.4 GCaMP fluorescence correction for hemodynamic crosstalk*

It is important to consider that both the excitation and emission wavelengths of GCaMP fluorescence are absorbed by HbO and HbR, whose concentrations vary over time. If this contamination is not corrected for accurately, it could influence the analysis performed for the coupling relationship between neural activity and hemodynamics. Here we implemented two commonly used methods of correction for hemodynamic crosstalk<sup>173</sup>:

##### 1) Ratiometric method

This first approach for hemodynamic correction uses the simultaneously obtained diffuse reflectance images at 530 nm. Here, we assume that the tissue properties are the same at the GCaMP excitation and emission wavelengths, 473 nm and 530 nm respectively, and the pathlength is the sum of the excitation and emission pathlengths. This allows us to remove hemodynamic crosstalk by dividing the change in GCaMP fluorescence by the change in 530 nm reflectance, which is approximately equal to the change in calcium concentration,

$$\frac{c_f(t)}{c_f(t_0)} \approx \frac{F(t)}{F(t_0)} / \frac{I(t, \lambda_{Em})}{I(t_0, \lambda_{Em})}$$

While the ratio method is simple to implement, it assumes that the tissue properties at the

excitation and emission wavelength are the same and is therefore a less rigorous method of correction.

## 2) Attenuation estimation method

The attenuation estimation method is a more rigorous way to correct for the hemodynamic crosstalk as it uses the simultaneously obtained HbO and HbR concentration to estimate the attenuation of the fluorescence signal. This method has been described in detail previously. The change in calcium concentration is approximately equal to the change in GCaMP fluorescence scaled by a time-varying hemoglobin absorption factor at both the GCaMP excitation and emission wavelengths:

$$\frac{\Delta c_{GCaMP}(t)}{c_{GCaMP}} = \frac{\Delta F(t)}{\bar{F}} \cdot \exp(\Delta\mu_{a,Ex}(t)x_{Ex} + \Delta\mu_{a,Em}(t)x_{em})$$

where  $\Delta\mu_{a,Ex}$  is the change in absorption at the excitation wavelength,  $\Delta\mu_{a,Em}$  is the change in absorption at the emission wavelength,  $x_{Ex}$  is the excitation pathlength, and  $x_{Em}$  is the emission pathlength. The time-varying absorption coefficient at each wavelength can be expressed as a sum of HbO and HbR.

$$\Delta\mu_{a,\lambda}(\lambda, t) = \epsilon_{HbO}(\lambda)\Delta[HbO](t) + \epsilon_{HbR}(\lambda)\Delta[HbR](t)$$

where,  $\epsilon(\lambda)$  is the wavelength-dependent extinction coefficient of HbO and HbR, and  $[HbO]$  and  $[HbR]$  are their concentrations. Estimates of the pathlength factor can be obtained from Monte Carlo simulations of photon transport<sup>152,179</sup>. For the Monte Carlo simulations (described in Section 4.3.5 below) we used tissue optical properties obtained from SFDI performed at 530 nm<sup>180</sup>. Therefore we obtained the pathlength at the emission wavelength only. To determine the effect of pathlength and model the error involved in the

correction algorithm due to pathlength, we ran the attenuation estimation calculation using a range of excitation and emission pathlengths from  $X_{ex} = 0.52:0.02:0.9$  mm and  $X_{em} = 0.52:0.02:0.9$  mm. By assuming that the total pathlength remains constant (as described in Results) we can also calculate the excitation pathlength required for accurate correction.

#### *4.3.5 Monte Carlo simulations*

To obtain accurate pathlengths at the emission wavelengths of 530 nm we ran Monte Carlo simulations of photon transport using the Monte Carlo eXtreme (MCX) platform, a GPU-accelerated simulator that simulates thousands of photons simultaneously to model light transport in 3D turbid media<sup>179,181</sup>. For the simulation, a disk shaped light source with large diameter was incident on a semi-infinite medium with a scattering anisotropy of  $g = 0.9$  and refractive index of  $n = 1.33$ . The 3D medium had dimensions of 60 x 60 x 60 mm with the source centered at  $(x,y,z) = (30,30,1)$  mm with a diameter of 60 mm. The detector was a point detector with radius 1 pixel located at  $(x,y,z) = (30,30,1)$ . The edges of the medium are index matched and the simulation was run with  $10^6$  photons. The absorption and scattering coefficient are obtained from SFDI measures as described in Section 3.1. The absorption coefficient used was  $0.58\text{mm}^{-1}$  and the scattering coefficient used was  $10.4\text{mm}^{-1}$ , which was obtained by averaging the scattering and absorption coefficients obtained with SFDI across all control non-stroked mice. After stroke, the absorption and scattering coefficients used were determined on a semi pixel-by-pixel basis. A Monte Carlo simulation was run on any pixel that had a scattering coefficient that was 30% larger than the mean scattering coefficient of the control animals, using the respective absorption and

scattering coefficients of that pixel. The average pathlength was calculated from the history file of the detected photons. Each photon was converted to a weight depending on its likelihood of existing based on the absorption coefficient of the medium. The average pathlength is then calculated by summing each photon's weight multiplied by its pathlength.

## 4.4 Results

### 4.4.1 *Fluorescence correction for hemodynamic crosstalk is needed for accurate estimation of GCaMP dynamics*

The GCaMP excitation and emission spectra have strong overlaps with the absorption spectrum of hemoglobin, as shown in Figure 4.1a. Moreover, most neural activity on the hemodynamic response timescale is accompanied by an increased blood flow and metabolic demand, which results in an increase in oxy-hemoglobin and total hemoglobin and a decrease in deoxy-hemoglobin. This change in the hemodynamic response that accompanies increased neural activity absorbs some of the GCaMP excitation and emission light, thereby contaminating the fluorescence signal measured by the camera. This contamination needs to be corrected for accurate analysis of the GCaMP signal and of neurovascular coupling.

Figure 4.1a shows the absorption spectrum of oxy- and deoxy-hemoglobin at the wavelengths of light measured by the IOSI setup overlaid with the GCaMP excitation and absorption spectrum. Figure 4.1b top panel shows the imaging session schematic, where each trial involved 5 seconds of baseline, followed by 5 seconds of stimulation with air-

puff to the forepaw, followed by 20 seconds of recovery. Each trial was repeated 20 times in one session. The hemodynamics are analyzed, and the 20 trials are averaged, as described in the methods section. The GCaMP dynamics are analyzed as a change in fluorescence over time compared to baseline fluorescence. The middle panel of Figure 4.1b shows the spatial extent of the both the hemodynamic and GCaMP responses to air-puff during the 5 seconds of stimulation. The bottom panel of Figure 4.1b shows the time course of the responses. While the hemodynamic response follows the expected dynamics, the GCaMP showed an increase in fluorescence immediately following the start of stimulation but began to decrease and went negative before the end of the 5 seconds of stimulation. Averaging the GCaMP response during the 5 seconds of stimulation manifests as a zero net change and therefore we do not observe any spatial activation in the GCaMP map in the middle panel of Figure 4.1b. This decrease in the GCaMP signal is due to absorption of the GCaMP signal by the hemodynamic response.

To validate this claim, we can image a mouse with a cellular fluorescence marker, that is, fluorescence that does not depend on neural activity, with the same excitation and emission spectra as GCaMP. Our expectation would be that the hemodynamic response would lead to a corresponding decrease in the baseline fluorescence. That is indeed what was observed as seen in Figure 4.1c, where the raw fluorescence showed a decrease that corresponded to the simultaneous increase in hemodynamics.

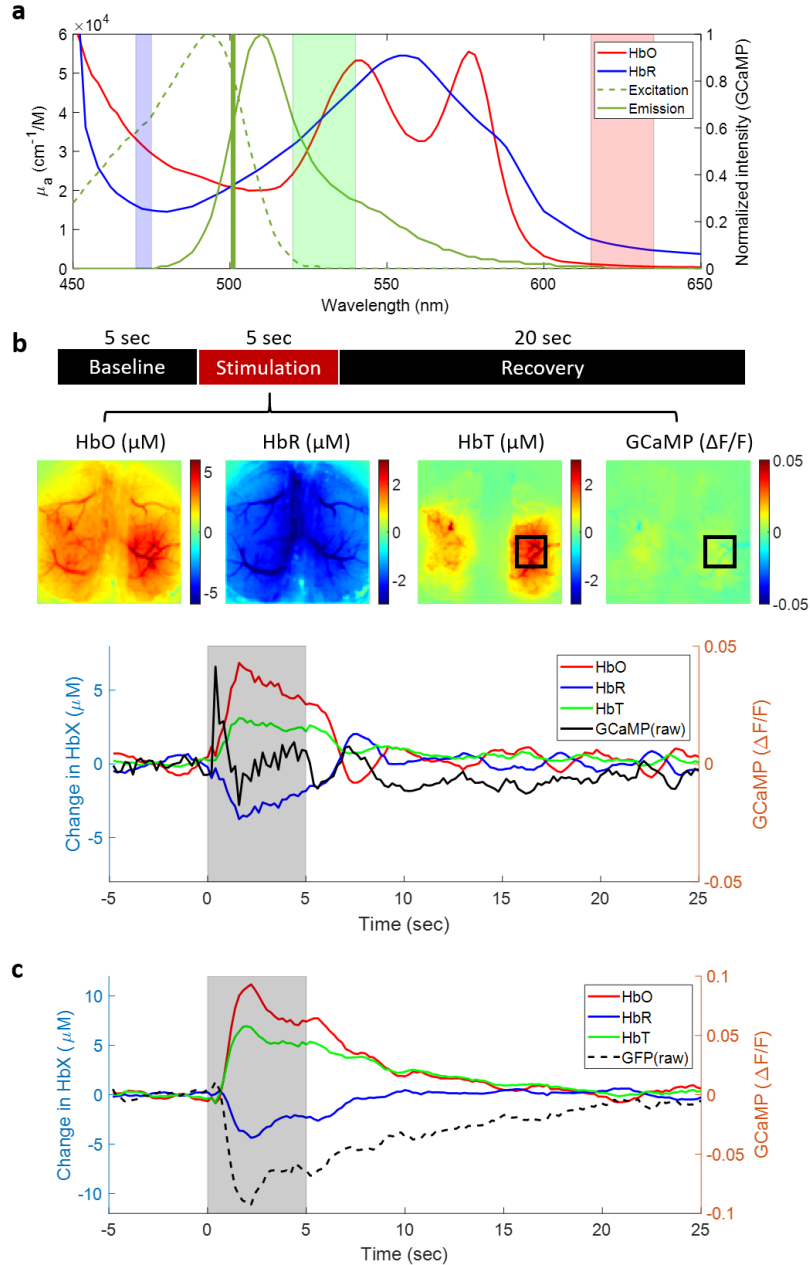


**Figure 4.1: Hemodynamic contamination of fluorescence data**

(a) Absorption spectra of oxy- and deoxy-hemoglobin overlaid with the GCaMP excitation and emission spectra along with bands indicating wavelengths used for imaging. (b) Spatial and temporal changes in GCaMP and hemodynamics during forelimb air-puff stimulation. Top: Trial breakdown during stimulation, middle: spatial maps of changes in oxy, deoxy, and total hemoglobin, as well as change in GCaMP, black box indicates ROI for time traces, bottom: time course of each metric. The gray shaded region indicates stimulus on periods. (c) Change in oxy, deoxy, and total hemoglobin along with change in GFP fluorescence during stimulation in a GFP positive mouse.

#### *4.4.2 Fluorescence correction for hemodynamic crosstalk with the ratiometric method underestimates the correction*

The ratiometric method is a simple technique that uses diffuse reflectance images acquired simultaneously with fluorescence GCaMP images to correct for the hemodynamic crosstalk. This method assumes that the excitation and emission wavelengths of GCaMP have the same tissue optical properties and the pathlength is the sum of the excitation and emission pathlengths. This allowed us to remove hemodynamic crosstalk by dividing the change in GCaMP fluorescence by the change in 530 nm reflectance, which is approximately equal to the change in calcium concentration. Figure 4.2a shows a GCaMP expressing mouse without and with the ratiometric correction. Now we see the spatial map of increased neural activity in the forelimb somatosensory region as well as a sustained increase in neural activity through the full 5 seconds of air-puff stimulation with the correction applied.

While this method does alter the neural response as expected, we need to validate the accuracy of the correction. To that end we applied the same correction method to the GFP expressing mouse during forepaw stimulation, with the expectation that the correction algorithm would yield a flat line at zero if the correction is accurate, as the cellular fluorescence is not dependent on neural or hemodynamic activity. Figure 4.2b shows the spatial and temporal uncorrected and ratio corrected GFP activity. The time course showed good correction, except in the early response phase, where we see that the corrected signal still exhibits a slight decrease when we expect no GFP signal change.

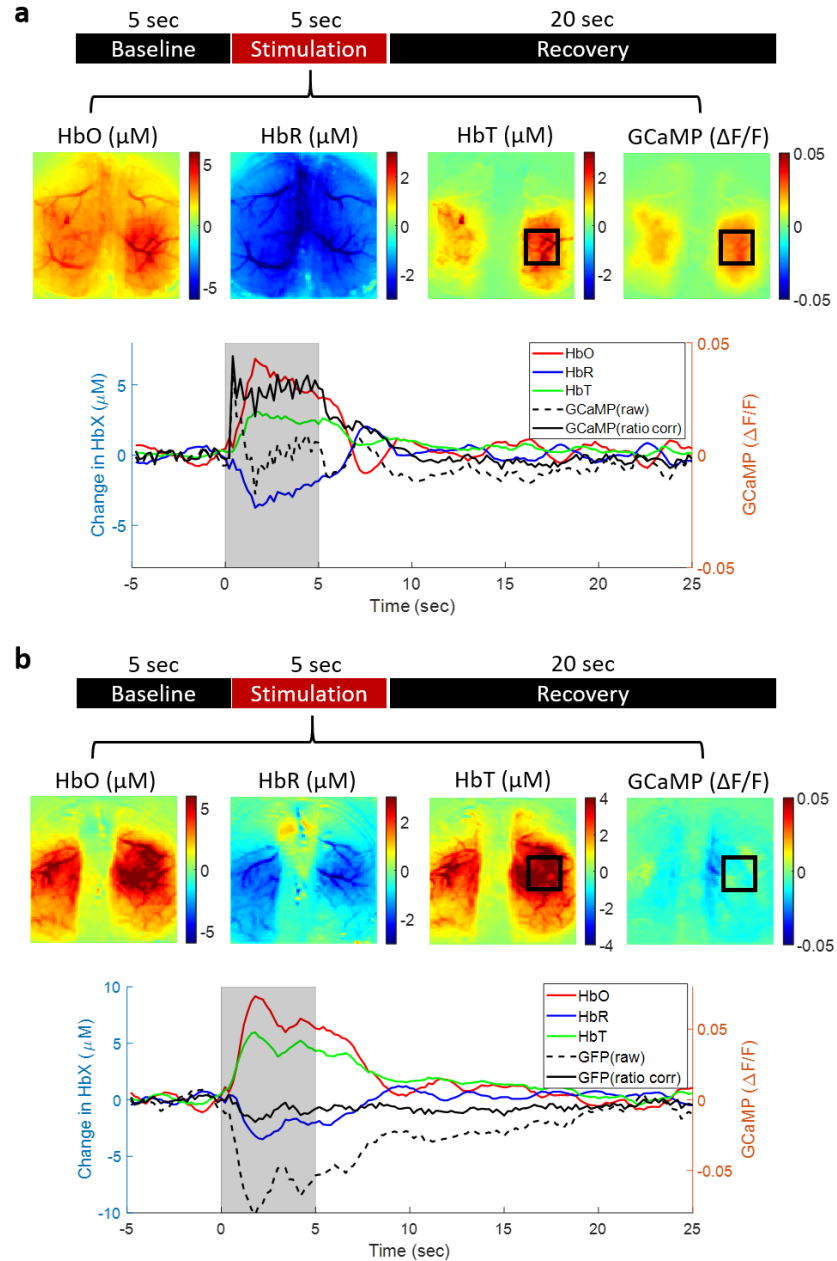


**Figure 4. 2: Fluorescence correction for hemodynamic crosstalk with ratiometric method**

(a) Spatial and temporal changes in GCaMP and hemodynamics during forelimb air-puff stimulation. Top: Trial breakdown during stimulation, middle: spatial maps of changes in oxy, deoxy, and total hemoglobin, as well as change in ratio corrected GCaMP, black box indicates ROI for time traces, bottom: time course of each metric, note that corrected GCaMP is elevated through the full stimulus period. Gray shaded region indicates stimulus on periods. (b) Same as in (a) but in a GFP positive mouse. Ratio correction is underestimated during the stimulus period.

*4.4.3 Attenuation estimation correction more accurately corrects for hemodynamic crosstalk when appropriate pathlength factors are considered*

The ratiometric correction method assumes that the tissue optical properties at the excitation and emission wavelength are the same and that the pathlength of the 530 nm reflected light images are approximately the sum of the excitation and emission pathlengths. During functional activation the balance between oxy- and deoxy-hemoglobin is altered compared to baseline and the absorption within the tissue of oxy- and deoxy-hemoglobin at the excitation and emission wavelengths are different. These factors could cause systemic errors in the correction provided by the ratio method.

The attenuation estimation method overcomes these challenges by using simultaneously obtained changes in oxy- and deoxy-hemoglobin to calculate the time-varying absorption factor to better account for the confounding influence of the hemodynamics of the measured fluorescence signal. The attenuation estimation method also takes into account the difference in pathlengths at the excitation and emission wavelengths for better approximations of calcium dynamics. Previous work in resting-state neurovascular coupling has shown that an excitation pathlength of 0.056cm and emission pathlength of 0.057cm obtained from Monte Carlo simulations yield corrected GCaMP images with minimal vessel artifact. However, use of these pathlengths also led to an underestimation of correction in our data when applied to GFP animals, as shown in Figure 4.3a.

To understand the effect of pathlength on the correction we tested a range of excitation and emission pathlengths on a stimulation session performed in a GFP mouse

and calculated the sum of squared error from the expected fluorescence corrected value of zero to find the optimal set of pathlengths to obtain the most accurate correction. A pathlength range of 0.042 cm – 0.094 cm was used for both excitation and emission. Figure 4.3b shows the raw GFP trace along with a trace for each combination of excitation and emission pathlengths, shown by the gray lines, and is also overlaid with the oxy, deoxy, and total hemoglobin change. Figure 4.3c shows individual traces within five different pathlength combinations to better understand its effects on correction. Short excitation and emission pathlengths lead to underestimation of the correction, while long excitation and emission pathlengths lead to overestimation of the correction during the response phase. A combination of excitation and emission pathlengths lie on a diagonal in the mid-range where the corrections were similar and they also had a good fit with respect to the expected zero value. Figure 4.3d shows the sum of squared error with respect to zero for each combination of excitation and emission pathlengths. The region of best fit lies on a diagonal with a slope of -1 and the sum of excitation and emission pathlengths along this diagonal, which corresponds to the total pathlength, was conserved.

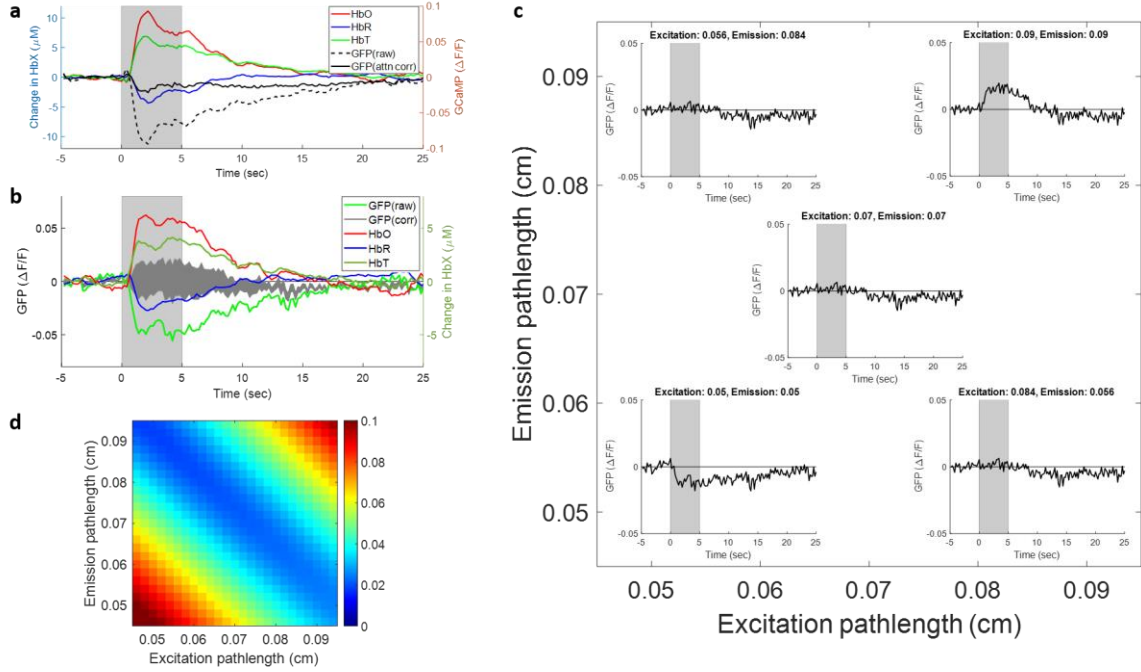


**Figure 4.3: Effect of pathlength on attenuation correction**

(a) Time trace of change in oxy, deoxy, and total hemoglobin overlaid with raw and attenuation corrected change in GFP signal during air-puff stimulation to the forelimb. (b) Same as in (a) with attenuation corrected GFP time traces using a range of excitation and emission pathlengths (0.042 – 0.094 cm). (c) Five representative combinations of excitation and emission pathlengths and its effect on correction. (d) Sum of squared errors with respect to zero for each excitation-emission combination.

To determine the appropriate combination, a Monte Carlo simulation can be run with some prior knowledge of the optical properties of the tissue. Monte Carlo simulations of photon transport have been used for decades to simulate the propagation of light through turbid 3D samples that mimic brain tissue. Our prior knowledge of absorption ( $\mu_a$ ) and scattering coefficients ( $\mu_s$ ) of brain tissue can be obtained from SFDI performed at 530 nm, as described in Chapter 3. Figure 4.4a shows a spatial map of  $\mu_a$  and  $\mu_s$  for one example mouse (left) and the mean and standard deviations for all mice (right). A mean  $\mu_a$  of  $0.58\text{mm}^{-1}$  and  $\mu_s$  of  $10.4\text{mm}^{-1}$  are used in the Monte Carlo simulations. With these

parameters we obtain an average pathlength at the emission wavelength of 530 nm equal to 0.84 mm and to maintain a conserved total pathlength of 1.38 mm we get an excitation pathlength equal to 0.54 mm. With these new pathlengths we can validate the accuracy of the correction with the GFP mouse as shown in Figure 4.4b. With the new pathlengths the attenuation estimation method is more accurate.

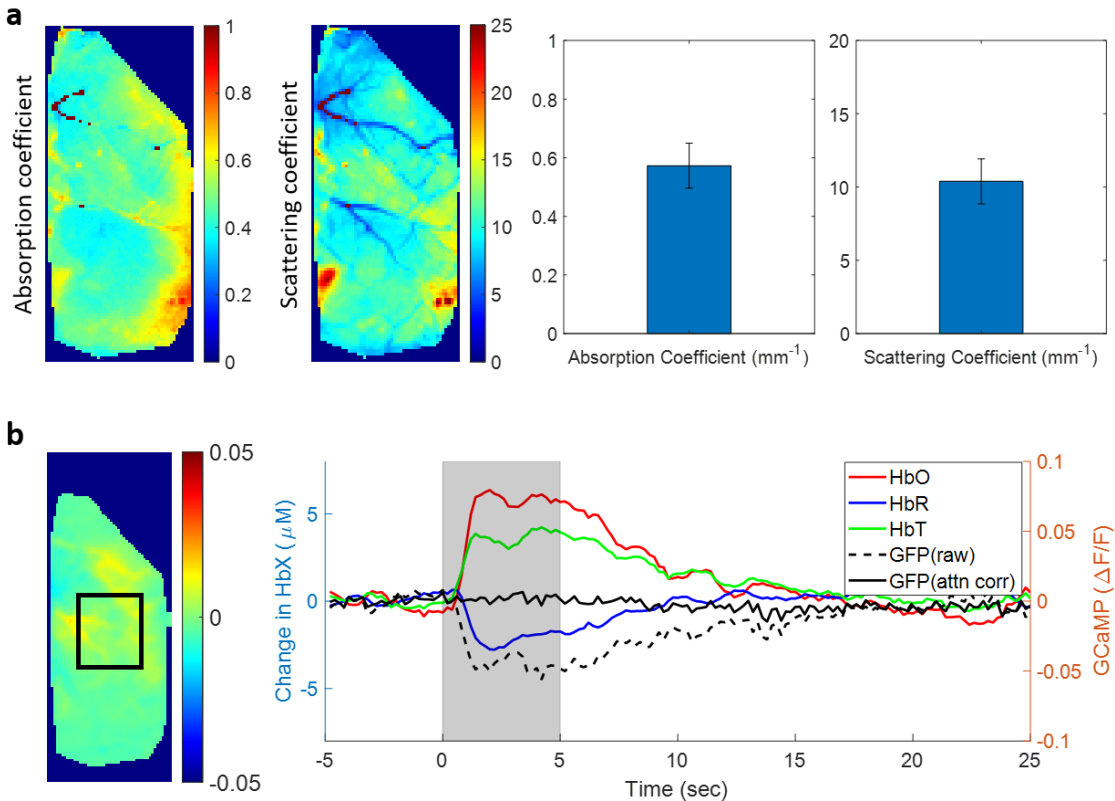


**Figure 4.4: Attenuation correction applied with pathlengths obtained from SFDI absorption and scattering**

(a) Absorption and scattering coefficients obtained from SFDI, left: spatial map from one animal, right: mean and standard deviation from all animals. (b) Time trace of change in oxy, deoxy, and total hemoglobin overlaid with raw and attenuation corrected change in GFP signal during air-puff stimulation to the forelimb using the Monte Carlo obtained pathlengths.

#### *4.4.4 Stroke leads to changes in tissue optical properties that can be accounted for in the correction algorithm*

Prior work from our lab and others have shown that tissue optical properties are altered in both the acute and chronic phases of stroke. Chapter 3 implemented spatial frequency domain imaging (SFDI), which is a diffuse optical reflectance technique that estimates tissue absorption and reduced scattering coefficients. We showed that the reduced scattering coefficient at 530 nm increases in the acute phase after stroke and the spatial region with increased scattering corresponds to the stroke core. The reduced scattering coefficient can be converted to the scattering coefficient with the anisotropy factor. Figure 4.5a shows that the scattering coefficient is also increased in the chronic phase after stroke. These changes in the absorption and scattering coefficients post-stroke can affect the correction algorithm for hemodynamic crosstalk as they alter the pathlength of light in tissue. The use of inaccurate pathlengths for correction can contaminate the correction and confound the relationship between neural and hemodynamic activity.

This change in pathlength can be accounted for by using the absorption and scattering coefficients obtained from SFDI to calculate new pathlength factors at each time point after stroke at the emission wavelength of 530 nm. Any pixel with a scattering coefficient larger than 30% of the mean scattering coefficient pre-stroke was run through a Monte Carlo simulation to obtain the new pathlength. Pathlengths at all other pixels are maintained at the pre-stroke pathlength. Figure 4.5b shows all the pixels that are larger than 30% of the mean scattering coefficient from the 1 week image from 4.5a and Figure 4.5c shows the pathlength (in cm) at 530 nm at each pixel for the same time point. Since we

estimated the total pathlength for most accurate correction and we also know that the total pathlength is conserved, we can calculate the pathlength at the excitation wavelength that provides the best fit for correction.

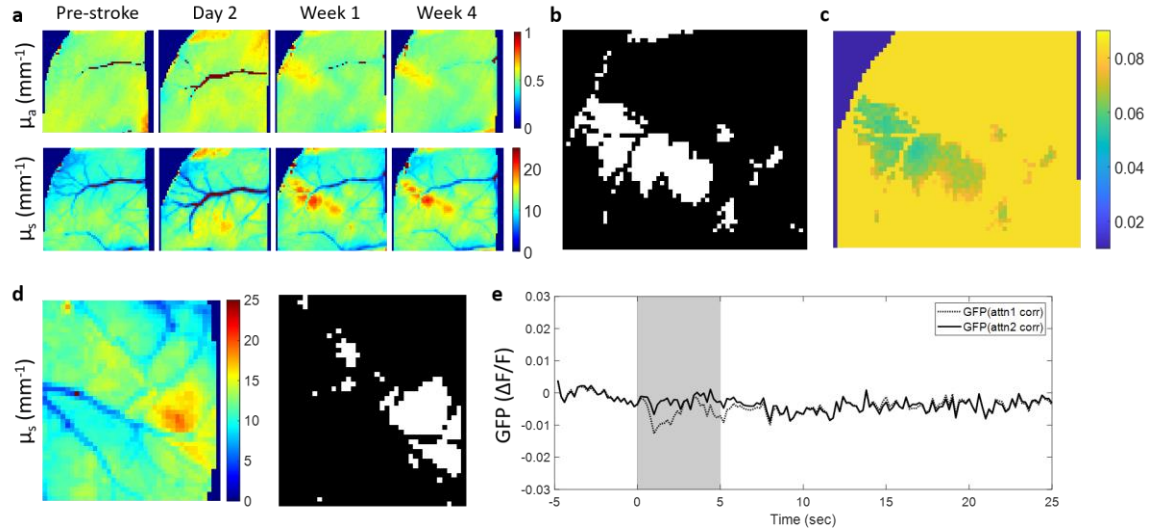


**Figure 4.5: Accounting changes in tissue optical properties after stroke in the correction algorithm**

(a) Stroke leads to changes in tissue optical properties that can be monitored through SFDI. (b) Binary image showing pixels with a scattering coefficient greater than two standard deviations from the mean scattering coefficient. Image is shown for 1 week after stroke from (a). (c) Pathlength calculated for each pixel in cm at 530 nm. (d) GFP mouse at 2 days after stroke, left: scattering coefficient, right: pixels with scattering coefficient above threshold. (e) Correction without and with accounting for optical property changes post-stroke applied to GFP mouse, attn1 corr corresponds to no accounting for optical changes and attn2 corr corresponds to with accounting for optical changes.

We can validate this method post-stroke by analyzing the functional responses in a GFP expressing mouse. A GFP expressing mouse can be analyzed with and without accounting for pathlength changes after stroke to see the effect of altered pathlength on the accuracy of the hemodynamic correction. Figure 4.5d shows a GFP mouse at 2 days post-stroke where the left image shows the scattering coefficient from SFDI and the right image shows the pixels with scattering coefficient above the two standard deviation threshold.

Figure 4.5e shows the GFP time trace without accounting for optical property changes (attn1 corr, dotted line) and with accounting for optical property changes (attn2 corr, solid line). When optical property changes, and therefore pathlength changes, are not accounted for there is an underestimation of the correction required, but when changes are accounted for the correction has a smaller error.

## 4.5 Discussion

In this chapter we have implemented the instrumentation required for simultaneous neural and hemodynamic functional imaging and addressed the need for accurate GCaMP fluorescence correction for hemodynamic crosstalk when evaluating neurovascular coupling. We first highlighted the need for hemodynamic crosstalk correction and then implemented two commonly used correction techniques in healthy animals. Additionally, we explored the influence of optical pathlength on the correction. We then showed that stroke leads to changes in tissue optical properties, which need to be accounted for in the correction algorithm to accurately correct for hemodynamic crosstalk.

Accurate fluorescence correction for hemodynamic crosstalk is essential for applications studying neurovascular coupling. Neurovascular coupling forms the basis for functional neuroimaging studies, such as fMRI and fNIRS, which monitor the vascular responses to brain activity and rely on neuronal activity being coupled to hemodynamics for interpreting the results<sup>59</sup>. For accurate interpretation of brain activity we need to understand this neural and hemodynamic coupling both in healthy brains and in brains with neurological injury. With the advancements of in vivo optical technology in preclinical

animal models, these models make excellent tools to study the underlying physiological mechanisms such as neurovascular coupling. These studies then aid in better interpretations of human functional neuroimaging studies. Specifically, the genetically encoded fluorescence calcium indicator, GCaMP, which becomes activated during neuronal activity, has allowed a whole new suite of neuroscience questions to be answered, and understanding and modeling neurovascular coupling is one of these questions<sup>172,182,183</sup>. Prior works from these groups have studied neurovascular coupling by simultaneously capturing neuronal spiking activity and local field potentials, fluorescence GCaMP activity, and changes in oxy- and deoxy-hemoglobin on a macroscopic scale. Additionally, the contamination of the GCaMP signal by the hemodynamic activity has also been addressed<sup>173,174</sup>. The GCaMP excitation and emission light must travel in the brain tissue and will therefore experience the absorptive properties of brain tissue it travels through. Hemoglobin has strong absorption properties in the excitation and emission spectrum of GCaMP and primarily contributes to GCaMP absorption. If the background absorption properties remained constant then these effects would have minimal impact, however, through neurovascular coupling, almost all neuronal activity is accompanied with a hemodynamic response and therefore will modulate the amount of GCaMP absorbed accordingly. This confounds the true calcium signal and needs to be corrected for accurate analysis of neuronal activity and neurovascular coupling.

Prior work has established two main methods to correct for the hemodynamic crosstalk, the ratiometric method and the attenuation estimation method. The ratiometric method, which corrects for crosstalk by dividing the change in fluorescence by

simultaneously acquired changes in diffuse reflectance images captured at the emission wavelength of GCaMP, is the most commonly used method as it is simple to implement and requires only one additional wavelength<sup>155,184</sup>. The attenuation method uses simultaneously obtained changes in oxy- and deoxy-hemoglobin to calculate the absorption experienced by the GCaMP to correct for crosstalk<sup>172</sup>. The attenuation method is a more rigorous method as it does not assume that the tissue properties are the same at the excitation and emission wavelengths and calculates the attenuation at both wavelengths. While this method is more rigorous, it is used less often as it needs at least two additional wavelengths for hemodynamic calculations, therefore slowing down the frame-rate. However, these techniques had yet to be validated in a mouse model with a fluorescent neuronal structural marker that does not depend on neuronal activity and which has a similar excitation and emission spectrum compared with GCaMP. Here, we tested the accuracy of these methods, using a mouse strain that expressed green fluorescent protein (GFP) in excitatory pyramidal cells, during external stimulation with air-puff to the forelimb. Our results indicated that the ratiometric method underestimated the correction during the early response phase of stimulation. This could be due to the different timelines with which oxy- and deoxy-hemoglobin respond to stimulus<sup>185,186</sup>. It has been shown that there is first an increase in oxy-hemoglobin followed by a decrease in deoxy-hemoglobin during the onset of the hemodynamic response to stimulation. Oxy- and deoxy-hemoglobin have different absorption properties at the excitation wavelength and therefore the assumption that tissue optical properties, like absorption and pathlength, are the same at the excitation and emission wavelength may result in errors during correction.

To overcome these assumptions, the attenuation estimation method uses changes in both oxy- and deoxy-hemoglobin to estimate the correction required. From this we can infer the time-varying changes in attenuation at the excitation and emission wavelengths and perform the correction by scaling the change in fluorescence with the attenuation and a pathlength factor. Prior work has identified pathlength factors that yield corrected GCaMP images with minimal vessel artifacts<sup>173</sup>. However, these pathlengths were determined for resting-state spontaneous activity and not during stimulus induced activity where the hemodynamic changes are much larger. Additionally, the correction technique was validated in a yellow fluorescent protein expressing mouse where the fluorophore spectra varies from GCaMP. Our validation data suggests that the pathlength has a significant influence on the accuracy of correction and previously used values underestimate the correction during the stimulation response phase. Additionally, we found that the total pathlength is conserved for combinations of excitation and emission pathlengths that yielded the least correction error, that is, the correction with least error was on a diagonal with slope of -1. We calculated the pathlength at the emission wavelength of GCaMP using Monte Carlo simulations of photon transport with tissue properties estimated from SFDI and then used this pathlength and the knowledge of the total pathlength to calculate the excitation pathlength. This method yielded the least correction error when validated with the GFP mouse.

Finally, we need to address any changes to the correction algorithm required post-stroke when tissue optical properties have changed. Stroke leads to changes in absorption and especially scattering coefficient in the acute and chronic phases of recovery<sup>145,180</sup>. In

the acute phase increase in scattering is believed to be due to cellular swelling, while in the chronic phase it is due to cell death and inflammation. These changes in optical properties need to be accounted for in the correction algorithm for accurate estimation of the true calcium dynamics. Here, we used the SFDI and Monte Carlo methods set up for the healthy brain to obtain pathlength factors for the stroke brain. Accounting for changes in optical properties had less correction error compared to not accounting for these changes primarily during the cortical response phase of stimulation. We suggest that these factors aid in better extraction of the calcium signal post-stroke and will aid in better interpretation of changes to neurovascular coupling during the stroke recovery phase when assessing local changes during stroke recovery.

A limitation of the current work is the small sample size for the GFP mouse. We have validated our technique with one mouse, however responses can vary across mice and may impact the correction factors. Although, we believe that our techniques, validated across multiple sessions, depend on the pathlength factor, which should not be affected by the small sample size. In conclusion, we bring to attention the need for more rigorous validation of fluorescence correction for hemodynamic crosstalk and some challenges faced by techniques used today. We implemented two commonly used techniques and suggested improvements that would aid in more accurate correction algorithms. Finally, we applied our technique to mice that have undergone photothrombotic stroke.

## CHAPTER 5 – TARGETED PHOTOTHROMBOTIC STROKE DISRUPTS NEUROVASCULAR COUPLING

### 5.1 Abstract

Functional neuroimaging, which measure vascular responses to brain activity, are invaluable for monitoring stroke patients during recovery. However, the interpretation of these vascular signals, which are altered after stroke, in terms of the underlying neuronal activity is under active investigation. In other words, we do not know the effect of stroke on neurovascular coupling and are therefore limited in our ability to use these vital techniques to monitor stroke recovery. There is a need for preclinical animal models to capture neuronal and hemodynamic activity simultaneously to assess alterations in neurovascular coupling. In this study, we simultaneously captured neuronal activity, through fluorescence calcium imaging, and hemodynamics, through intrinsic optical signal imaging, during longitudinal stroke recovery. We found that photothrombotic stroke to somatosensory forelimb area altered neurovascular coupling in the acute phase within the affected forelimb and peri-infarct regions. Neurovascular coupling was reestablished in the chronic phase and acute recovery of neurovascular coupling predicted behavioral outcome. Stroke also resulted in acute increases in excitability and global brain oscillations, which showed distinct spatial patterns between calcium and hemodynamics. Increases in contralesional forelimb excitability was associated with increased functional connectivity of the contralesional forelimb representation. Additionally, increases in hemodynamic, but not calcium, oscillations were associated with improved long term behavioral outcomes.

## 5.2 Introduction

An ischemic stroke occurs due to an interruption of blood flow caused by thrombosis or embolism of a blood vessel, which leads to a reduction or complete loss of blood supply to downstream areas. Loss of blood supply causes a starved oxygen environment and leads to cellular damage within minutes and ultimately to sensorimotor and cognitive impairments<sup>11,187</sup>. A majority of stroke patients survive the incident; however, most survivors are compromised in work capacity, the extent of which varies across patients from mild to severe impairments<sup>188</sup>. Some spontaneous recovery is typically seen in most patients in the months following injury, and most post-stroke recovery currently relies heavily on rehabilitative treatments<sup>4,5,30</sup>.

Functional neuroimaging methods such as fMRI and fNIRS, which measure the vascular response to brain activity, are valuable tools for monitoring and managing the recovery and treatment of stroke patients both in the acute and chronic phases of stroke recovery<sup>23,169,189</sup>. However, the vascular responses post-stroke are almost always altered relative to those seen in healthy individuals. BOLD-fMRI studies have revealed that task-related cortical responses following stroke undergo pronounced alterations in amplitude and spatial extent of the BOLD signal in both the ipsilesional and the contralateral hemispheres<sup>23,27,28</sup>. Additionally, studies assessing resting-state functional connectivity obtained with MRI (fc-MRI) have shown that inter-hemispheric connections are altered in the early acute phase of stroke in humans<sup>167,168</sup>. Whether these vascular response alterations are a reflection of the underlying differences in neuronal function or simply a result of injury to the vasculature is still under active investigation. In other words, we do not know

the effect of stroke on neurovascular coupling and thus are limited in our ability to use these valuable neuroimaging tools to study functional recovery in stroke survivors.

Neurovascular coupling (NVC) has been studied extensively in healthy subjects and there is a large body of evidence demonstrating that neural activity is closely related to cerebral blood flow and hemodynamics<sup>19,20</sup>. This tight coupling between neural activity and blood flow forms the basis of modern neuroimaging techniques that use the cerebrovascular changes caused by neural activation to map changes in function in the behaving human brain<sup>59</sup>. While NVC is maintained in the healthy brain, brain pathologies such as traumatic brain injury, Alzheimer's disease, and stroke may lead to disruptions in the interactions between neural activity and CBF, thereby confounding the interpretations of neuroimaging results<sup>24,25</sup>. Additionally, the effect of stroke on NVC has received limited and sometimes conflicting attention<sup>23,62,66</sup>. Thus, there is a need for preclinical stroke models to evaluate the functional aspects of neurovascular recovery and to use these findings to improve the interpretations of human neuroimaging studies.

Preclinical animal models of stroke have been used extensively over the last few decades to understand the mechanisms involved in stroke recovery, from molecular and cellular changes to large scale functional network reorganization<sup>97,98,190</sup>. On a mesoscopic level, studies performing in vivo calcium fluorescence imaging of neuronal activity have shown activation reorganization and functional remapping of the affected brain regions into the peri-infarct zone longitudinally, reflecting the evolution of stroke in humans<sup>44,45,47,123</sup>. Additionally, intrinsic optical signal imaging has been used to map changes to hemodynamics by assessing global changes using resting state functional

connectivity and also local changes through functional activation<sup>49,89</sup>. To improve interpretations of human functional neuroimaging studies and to understand the underlying physiology that gives rise to the observed vascular changes we need to obtain simultaneous measures of neural and hemodynamic changes post-stroke. Moreover, these measures need to be obtained on a macroscopic scale to understand both the local and global changes that result due to stroke, as well as cover the entire longitudinal recovery phase to capture both acute and chronic time points.

Prior work on functional recovery following ischemic stroke has focused either just on neuronal or hemodynamic activity changes or just the acute or chronic phase and, to the best of our knowledge, these measures have not yet been integrated to study neurovascular coupling during stroke recovery<sup>40,44,49,78,89</sup>. In this chapter, using our optimized mouse photothrombotic stroke model, we study the relationships between neuronal and hemodynamic activity in the affected and unaffected hemispheres during longitudinal stroke recovery.

### 5.3 Methods

#### 5.3.1 Experimental design

All experiments and animal procedures were approved by the Boston University Institutional Animal Care and Use Committee and were conducted following the Guide for the Care and Use of Laboratory Animals. All animals used in this study were adult Thy1-GCaMP6f mice (Jackson Labs, strain code: 025393, C57BL/6J-Tg(Thy1-GCaMP6f)GP5.17Dkim/J). The mice were implanted with bilateral cranial windows, one

window on each hemisphere, and allowed to recover for two weeks. Following recovery, mice underwent a habituation training in a custom imaging cradle to get adapted to the imaging setup and environment. Pre-stroke control measures were obtained one week prior to stroke and photothrombotic stroke was performed on Day 0 of the experiment. Following photothrombosis, mice were imaged longitudinally at Day 2, Week 1, Week 2, and Week 4 to span both the acute and chronic phases of stroke recovery. To correlate the cortical measures to behavior, forelimb asymmetry was measured using the cylinder test at each of the imaging time points. The timeline of experiments is outlined in Figure 5.1a.

### 5.3.2 *Animal preparation*

A bilateral cranial window exposing both hemispheres of the brain was implanted in all mice to determine the effect of stroke on both the ipsilesional and contralateral hemispheres. The surgical procedure for implantation of bilateral cranial windows followed a similar procedure to unilateral windows that has been previously described<sup>96</sup>. Briefly, mice were injected with Buprenorphine subcutaneously 1 hour prior to the start of surgery. During surgery, mice were anesthetized with isoflurane (3% at induction and 1-1.5% for maintenance with 1L/min oxygen) and body temperature was maintained at 37°C. Respiratory rate and toe pinch were used to monitor the depth of anesthesia throughout the surgical procedure. After incision of the scalp, a round aluminum head post, 12 mm in diameter, was attached to the intact skull with dental acrylic. A craniotomy was then performed on one hemisphere of the brain in order to remove the skull. A half-skull-shaped

curved glass (modified from Crystal Skull<sup>150</sup>, LabMaker, Germany) was used to cover the surface of the brain and then sealed with optical glue and dental acrylic. The craniotomy and glass procedure were repeated on the other hemisphere of the brain in order to create a bilateral cranial window implant. Recovery procedures were followed according to the guidelines provided by Boston University. After a two-week recovery period from surgery, mice were trained to remain head-fixed for up to 90 min for approximately 10 days. All experiments are done in awake head-fixed mice.

### *5.3.3 Simultaneous hemodynamic and calcium imaging*

To evaluate local and global changes in neurovascular coupling post-stroke, simultaneous measures of hemodynamic and neural activity were obtained during forelimb sensory stimulation and resting state. The instrumentation, task setup, and data analysis pipeline for measuring cortical hemodynamics have been outlined previously<sup>96</sup>. Figure 5.1a shows a simplified schematic of the imaging setup. Intrinsic optical signal imaging was used to assess changes to oxy- and deoxy-hemoglobin, HbO and HbR respectively, for the hemodynamic measure, and fluorescence GCaMP imaging was performed to assess changes in calcium dynamics as a measure of neural activity. The cortical windows were illuminated sequentially with 470 nm, 530 nm, and 625 nm LEDs (MXL3-C1, Thorlabs, X is the center wavelength), where the 470 nm LED was used for GCaMP excitation and the 530 nm and 625 nm LEDs were used for calculations of oxy- and deoxy-hemoglobin. A 500 nm long pass filter (FELH0500, Thorlabs) placed along the detection path blocked

out any GCaMP excitation light. Images were collected by a sCMOS camera (Hamamatsu ORCA-Flash 4.0 V3) at 15 Hz, 5 Hz per wavelength, with an exposure time of 50 ms. For resting state, spontaneous activity was obtained for 8 min. For sensory stimulation, two imaging session were performed at each time point pre- and post-stroke, one where the contralateral (affected) forelimb was stimulated and the second where the ipsilateral (unaffected) forelimb was stimulated. Each stimulation session consisted of 20 trials where each trial was obtained in a block-design fashion and consisted of 5 seconds of baseline, followed by 5 seconds of 3 Hz air-puff stimulation, followed by 20 seconds of recovery. A custom MATLAB script was used to synchronize and trigger the sequential LEDs, camera acquisition, and air puff stimulation. Raw images at 530 nm and 625 nm were analyzed for changes in oxy- and deoxy-hemoglobin using the modified Beer-Lambert relationship as described previously (Chapter 2 and 4)<sup>96,176</sup>. Calcium dynamics were analyzed as a change in fluorescence over time from the interspersed raw images excited at 470 nm. The fluorescence data were corrected for hemodynamic crosstalk, as hemodynamic changes contaminate the fluorescence signal and both the excitation and emission wavelengths. The correction algorithm used has been previously described and modified from Ma et al.<sup>172</sup>. The correction estimates the attenuation experienced by the GCaMP signal from the simultaneously obtained changes to oxy- and deoxy-hemoglobin. The change in calcium concentration is approximately equal to the change in GCaMP fluorescence scaled by a time-varying hemoglobin absorption factor at both the GCaMP excitation and emission wavelengths. The pathlength factor used for correction is obtained from Monte Carlo simulations of photon transport using the Monte Carlo eXtreme (MCX) platform<sup>179,181</sup>. The

absorption and scattering coefficients used for the MCX simulation were obtained from spatial frequency domain imaging (described below). For pre-stroke imaging, a single absorption and scattering coefficient, yielding a single pathlength, was used for correction of all pixels. A modified correction technique was introduced after stroke in order to account for changes in tissue optical properties<sup>145,180</sup>. After stroke, the absorption and scattering coefficients used were determined on a semi pixel-by-pixel basis. A Monte Carlo simulation was run on any pixel that had a scattering coefficient that was 30% larger than the mean scattering coefficient of the control animals, using the respective absorption and scattering coefficients of that pixel. This new pathlength was used for the correction of pixels within the stroke region that had increased scattering. The attenuation correction applied spatial maps and temporal traces are shown in Figure 5.1b and supplementary Figure 5.8.

#### 5.3.4 *Spatial frequency domain imaging*

To capture the spatial extent of the stroke core longitudinally and aid in fluorescence correction for hemodynamic crosstalk, SFDI was performed pre-stroke and at each time point post-stroke. The instrumentation, acquisition, and analysis to obtain absorption and scattering coefficients of the tissue have been described previously (Chapter 3)<sup>180</sup>. Spatially varying sinusoidal patterns were projected onto the cranial window by a digital micromirror device (DMD), and the reflected light was imaged by the sCMOS camera. Two spatial frequencies (0 and 0.4 mm<sup>-1</sup>) were projected at three phases (0, 120, and 240 deg). The acquired images were processed offline using MATLAB. The intensity at each

spatial frequency was demodulated and calibrated to a reference phantom to obtain the diffuse reflectance. A two-frequency lookup table was generated by Monte Carlo simulations at the two frequencies used for imaging from which absorption and scattering coefficients were extracted. To obtain the spatial extent of the stroke core, the relative change in scattering coefficient post-stroke was calculated with respect to pre-stroke scattering, and a semi-automatic contour was applied using a custom MATLAB script to create a stroke core outline. This core outline was used as the boundary for the start of the peri-infarct zone. The peri-infarct zone was defined as the region that extended 0.5 mm outward from the stroke core outline. SFDI was also used in the correction of GCaMP for hemodynamic crosstalk. The absorption and scattering properties obtained at each time point post-stroke were used to run the Monte Carlo simulation to determine the pathlength of light traveled in tissue. This pathlength is then used in the correction algorithm to scale the GCaMP signal, based on the time-varying changes in hemodynamic absorption, for accurate estimation of calcium dynamics (supplementary Figure 5.8).

### 5.3.5 Resting state functional connectivity analysis

Global network connectivity changes following stroke were assessed using resting state functional connectivity as described previously by a number of groups<sup>191–193</sup>. Time traces of HbO and GCaMP were bandpass filtered into two frequency bands, the typically used infraslow (0.008-0.09 Hz) frequency band and a high frequency band (0.09-0.4 Hz), and regressed to remove any global fluctuations in the signal. To evaluate the strength of

network connections to the affected forelimb region, a seed was placed in the center of the original forelimb somatosensory region of the affected hemisphere. The seed time trace was calculated by averaging the time trace within 0.25 mm of the seed location and connectivity was assessed by calculating the correlation between the seed time trace and the time course of every other pixel. By averaging the positive correlation coefficients between the forelimb seed and all pixels that lie in the contralateral forelimb, region we calculated a forelimb connectivity map. Interhemispheric connectivity maps were calculated by correlating each pixel within the affected hemisphere with its mirror pixel, mirrored along the midline, in the unaffected hemisphere. The interhemispheric connectivity index was then calculated by averaging all the pixels within the homotopic map of the affected hemisphere. To assess the overall connectivity of the brain, global connectivity maps were generated by calculating the correlation of each pixel with every other pixel and then assigning the average of the positive correlation coefficients to that pixel. From the global connectivity maps, a global connectivity index was calculated by taking the mean of the correlation coefficients for all pixels within the map. We also evaluated the strength of connectivity of the contralateral forelimb within the contralateral hemisphere. A similar procedure for ipsilesional forelimb was followed, except that the seed was placed in the contralateral forelimb region and intrahemispheric connectivity was calculated.

### 5.3.6 Neurovascular coupling

To assess the relationship between neuronal activity and hemodynamics, neurovascular coupling was modeled using linear least-squares deconvolution<sup>172</sup>. The cortical hemodynamic response is known to be a linear convolution of neural activity and a hemodynamic response function (HRF), also called an impulse response function. HRF is the hemodynamic response to a neural stimulus. In a linear system, the convolution can be expressed as  $y = X * h$ , and can be represented as:

$$\begin{bmatrix} y_1 \\ y_2 \\ \vdots \\ y_t \end{bmatrix} = \begin{bmatrix} x_1 & 0 & 0 & \dots & 0 \\ x_2 & x_1 & 0 & \dots & 0 \\ \vdots & \vdots & \vdots & \ddots & \vdots \\ x_t & x_{t-1} & x_{t-2} & \dots & x_n \end{bmatrix} \begin{bmatrix} h_1 \\ h_2 \\ \vdots \\ h_n \end{bmatrix},$$

where  $X$  is the input to the system, which is the corrected GCaMP fluorescence signal, and the length  $n$  used is 15 sec (from -5 sec to 10 sec),  $y$  is the output of the system, which is the hemodynamic signal, and  $h$  is the system's impulse function, the HRF. For the full time series, which includes 3000 samples at 5 Hz,  $X$  is a matrix of size 2975 x 75,  $y$  is a matrix of size 2975 x 1. Directly solving the linear system requires inverting a matrix that may be badly conditioned, so a regularization term is added and the solution is obtained, minimizing the cost function by setting the gradient of the cost function to zero, as described previously<sup>172</sup>, and is given by:

$$h = (X^T X + \lambda I)^{-1} X^T y.$$

The regularization term  $\lambda$  was chosen to be 0.1 through all the analysis. The deconvolution was performed on a pixel-by-pixel basis at each time point post-stroke.

### 5.3.7 Targeted photothrombosis

Focal cerebral ischemia was performed using an optimized photothrombosis method described previously<sup>96</sup>. A distal branch of the middle cerebral artery supplying the forelimb somatosensory region, determined through pre-stroke forelimb stimulation, was targeted for occlusion. A 520nm laser diode with axial and lateral parameters of 104 µm and 6 µm was tuned to a minimal post-objective power of 0.6 mW. These parameters were designed to occlude only the target vessel and prevent laser damage to the surrounding tissue, ensuring that the ischemia procedure was physiological in nature. Real-time changes to CBF were monitored through LSCI. Ten minutes of baseline CBF were obtained, following which the mouse was lightly anesthetized in order to inject Rose Bengal (100 µl, 15 mg/ml in saline) retroorbitally. The mouse was then immediately taken off isoflurane and allowed to recover, which was determined by a return of CBF to baseline and the mouse exhibiting natural behaviors such as whisking. Following recovery the green laser was turned on until the target vessel was occluded, as indicated by the target branch disappearing on LSCI. Once the target branch was occluded, the laser power was reduced to 0.5 mW for an additional two minutes and then turned off. If at any point the target branch started flowing again, the laser was turned back on until occlusion. Additionally, as described previously (Chapter 2), two collateral branches were also targeted to obtain a stable infarct. The procedure was followed for 1 hour from the initiation of photothrombosis.

### 5.3.8 *Behavioral testing*

The cylinder test was used in all mice to assess behavioral deficit in forelimb use over the course of 4 weeks following stroke. Two sessions of pre-stroke testing were obtained the week before stroke, induction to assess basal preference in forepaw use. Following photothrombotic stroke mice were tested at 2 days, 1 week, 2 weeks, and 4 weeks. Each testing session involved placing a mouse in a clear glass cylinder and videotaping its natural behavior from below for 15 minutes. Forelimb use was assessed by counting the number of times the mouse used each forelimb to make first contact with the cylinder wall during rears. Asymmetry in forelimb use after stroke was quantified as a percent change from baseline use of the contralateral (affected) forelimb. Change from baseline was used to compensate for the fact that some mice have a preference for one paw over the other even before a stroke.

### 5.3.9 *Data analysis and Statistics*

All data was analyzed offline using custom MATLAB scripts. Image analysis for SFDI, calcium fluorescence, and evoked and resting-state intrinsic optical signal imaging has been outlined in previous sections. The Dice similarity coefficient for area overlap in evoked responses and RSFC is calculated using the matlab function dice.m. The Dice coefficient is twice the ratio of the intersection of two binary images and the sum of the number of elements in each image, given by:

$$dice(A, B) = \frac{2 |A \cap B|}{|A| + |B|}$$

Goodness-of-fit correlation and significance for stimulus evoked response magnitudes of GCaMP and hemodynamics were made using a linear fit. All statistical analyses were made using MATLAB with *post hoc* comparisons using t-tests. A-two sample student's t-test was performed for comparing data points with pre-stroke data (Matlab function: ttest2).

## 5.4 Results

### 5.4.1 Wide-field fluorescence and intrinsic signal imaging can follow changes to calcium and hemodynamic activity after stroke

Neurovascular coupling has been studied extensively in healthy subjects in both humans and animal models. In rodents, wide-field fluorescence calcium and intrinsic optical hemodynamic signals have been imaged simultaneously to investigate the baseline relationships between neuronal activity and blood flow<sup>155,172</sup>. Imaging calcium dynamics via GCaMP6f has been used extensively over the last decade as a correlate and reliable metric of neuronal activity<sup>177</sup>. Here, we implemented these techniques to show that wide-field optical imaging can be used to investigate the differential effects of stroke on GCaMP calcium dynamics, used as a surrogate for neuronal activity, and cerebral blood volume assessed with changes to HbO and HbR. Figure 5.1a shows a simplified schematic of the imaging system and the experimental timeline. We first assessed alterations to evoked responses during sensory stimulation after stroke. Sensory stimulation using air-puff to the

forelimb is performed in a block-design manner (Figure 5.1b) and includes 5 sec of baseline, followed by 5 sec of 3 Hz stimulation, followed by 20 sec of rest before the next trial. Each trial is repeated 20 times in one session. Figure 5.1b shows the spatial maps and time course of one stimulation session in a healthy mouse. The raw GCaMP fluorescence signal was corrected for hemodynamic crosstalk using a modified attenuation estimation method prior to analysis (Figure 5.1b, Supplementary Figure 5.8). Unilateral photothrombotic stroke to the forelimb somatosensory cortex of the right hemisphere led to a significant suppression of the evoked calcium and hemodynamic sensory responses to air-puff stimulation of the contralateral (affected) forelimb within the affected hemisphere, while the responses in the unaffected hemisphere were preserved (Figure 5.1c,d). The largest suppression of response occurred at 2 days post-stroke with a slow return of response by 4 weeks, albeit suppressed compared to pre-stroke. At day 2 after stroke GCaMP showed a 70% reduction in response and total hemoglobin (HbT) and HbO showed a 100% and 45% reduction in response compared to pre-stroke (Supplementary Figure 5.9a). By 4 weeks after stroke the responses within the affected hemisphere had returned to 50% of their pre-stroke value. Forelimb air-puff stimulation of the unaffected forelimb did not have any significant alterations in the evoked responses of the contralateral (unaffected) hemisphere; however, the affected hemisphere showed suppressed responses (Figure 5.1e,f). Once suppressed, the affected hemisphere did not show recovery in its responses to ipsilateral (unaffected) forelimb stimulation for GCaMP and hemodynamics even at 4 weeks (Supplementary Figure 5.9b). Spatiotemporal maps of responses during baseline, stimulation, and recovery at each time point are shown in Supplementary Figure

5.10 for the same mouse shown in Figure 5.1c,e. Understanding the evolution of neuronal and hemodynamic responses simultaneously can aid in better interpretations of the alterations observed in the vascular fMRI signals after stroke. The results here show that wide-field fluorescence and intrinsic optical signal imaging post photothrombotic stroke are sensitive measures that allow the longitudinal monitoring of these neuronal and hemodynamic signals.

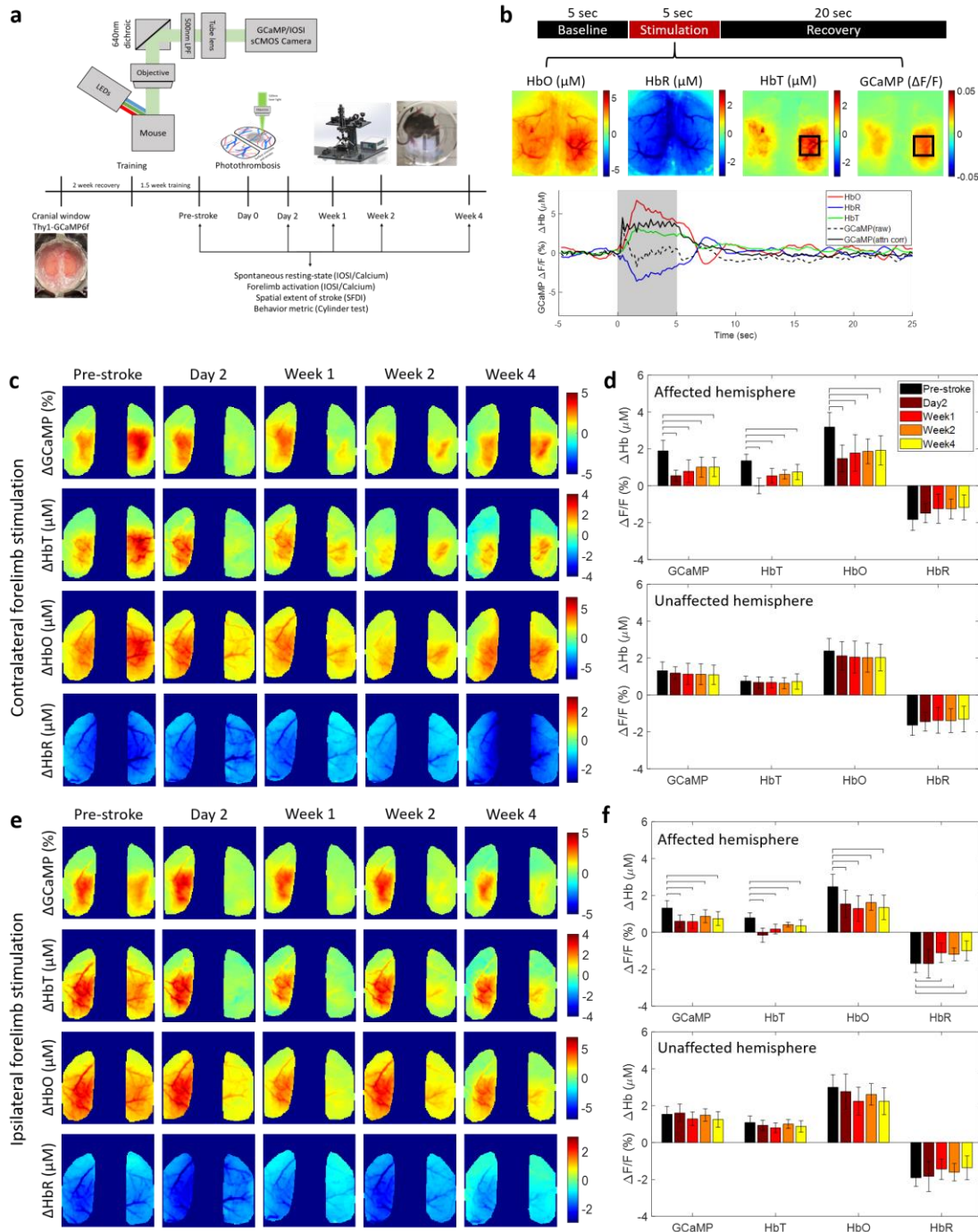


**Figure 5. 1: Simultaneous calcium and hemodynamic imaging post-stroke**

(a) Simplified imaging schematic and experimental timeline. (b) Top: Block design of each trial in a stimulation session, middle: trial averaged spatial maps of HbO, HbR, HbT, and corrected GCaMP, during 5 sec of air-puff stimulation to the left forelimb, bottom: trial averaged time course of each measurement, note that raw uncorrected GCaMP drops

immediately following the rise of the hemodynamic response and corrected GCaMP shows elevated responses through the full stimulation period. (c) Trial averaged spatial maps of calcium and hemodynamics showing magnitude of the response during 5 sec stimulation of the contralateral (affected) forelimb at each time point before and after stroke in one example mouse. (d) Response magnitudes during affected forelimb stimulation for all mice ( $n=12$ ) in the affected (top) and unaffected (bottom) hemispheres, histograms are mean  $\pm$  std. (e) Same as in (c) during stimulation of the ipsilateral (unaffected) forelimb. (f) Same as in (d) during stimulation of the ipsilateral (unaffected) forelimb. Bars in (d) and (f) indicate significance of  $p<0.05$ .

#### *5.4.2 Acute stroke alters the correlation between evoked calcium and hemodynamic responses*

We then examined whether aspects of the observed hemodynamic responses were correlated to the underlying calcium activity during sensory stimulation of the impaired forelimb. Figure 5.2a shows the trial-averaged mean and standard deviation of the time course of calcium, measured as a percent change in fluorescence (top row), and change in HbO and HbR, measured in  $\mu\text{M}$  (bottom row), averaged from all pixels within the affected hemisphere at pre-stroke, 1 week, and 4 weeks post-stroke. Spatial response maps at each time point were then thresholded at 75% of the peak response and all pixels that lie above that threshold were used for correlation analysis (Figure 5.2b). We first looked at the similarity in the response areas between the evoked calcium response and hemodynamic measures. Similarity was calculated using the Dice coefficient, which provides a measure of percent overlap between two images (Figure 5.2c). HbT and HbO showed high overlap (60%) with GCaMP before the stroke, indicating that GCaMP and hemodynamic responses were spatially localized, while HbR had a weaker spatial overlap with GCaMP (20%). While HbR did not show any significant changes to activation overlap post-stroke, HbT

and HbO showed a significant reduction in the spatial overlap with GCaMP across all time points after stroke, with a larger reduction in the acute time points of day 2 and week 1 compared to chronic time points. Similarity between GCaMP and hemodynamic response maps in the contralesional hemisphere did not show any significant alterations after stroke (Supplementary Figure 5.12a).

Next, we calculated the average magnitude of the response during 5 seconds of air-puff stimulation within all pixels above 75% of peak activation. We then correlated the magnitude of the GCaMP response to the magnitude of the HbO and HbR responses from each trial of a stimulation session. Figure 5.2d shows data pre- and post-stroke from one example mouse, each dot in the scatter plot represents data from one trial within a session of 20 trials. There was high correlation between the evoked responses of GCaMP and HbO as well as GCaMP and HbR prior to stroke, demonstrating good coupling between calcium activity and hemodynamics. There was a loss in correlation at 1 week after stroke, following which there was a reestablishment of correlation by week 4. This loss and reestablishment of correlation between response amplitudes was seen across the cohort of animals (Figure 5.2e). Both HbT and HbO show significant loss in correlation with respect to GCaMP in the acute phase, implying that calcium responses in acute stroke are not necessarily represented in the observed hemodynamic response. Additionally, the animals that continued to show loss in correlation at week 4 also had poor correlation in the acute phase (Supplementary Figure 5.11). Responses in the contralesional hemisphere continued to show similar trends of correlation between calcium and hemodynamics after stroke compared to before stroke (Supplementary Figure 5.12b).

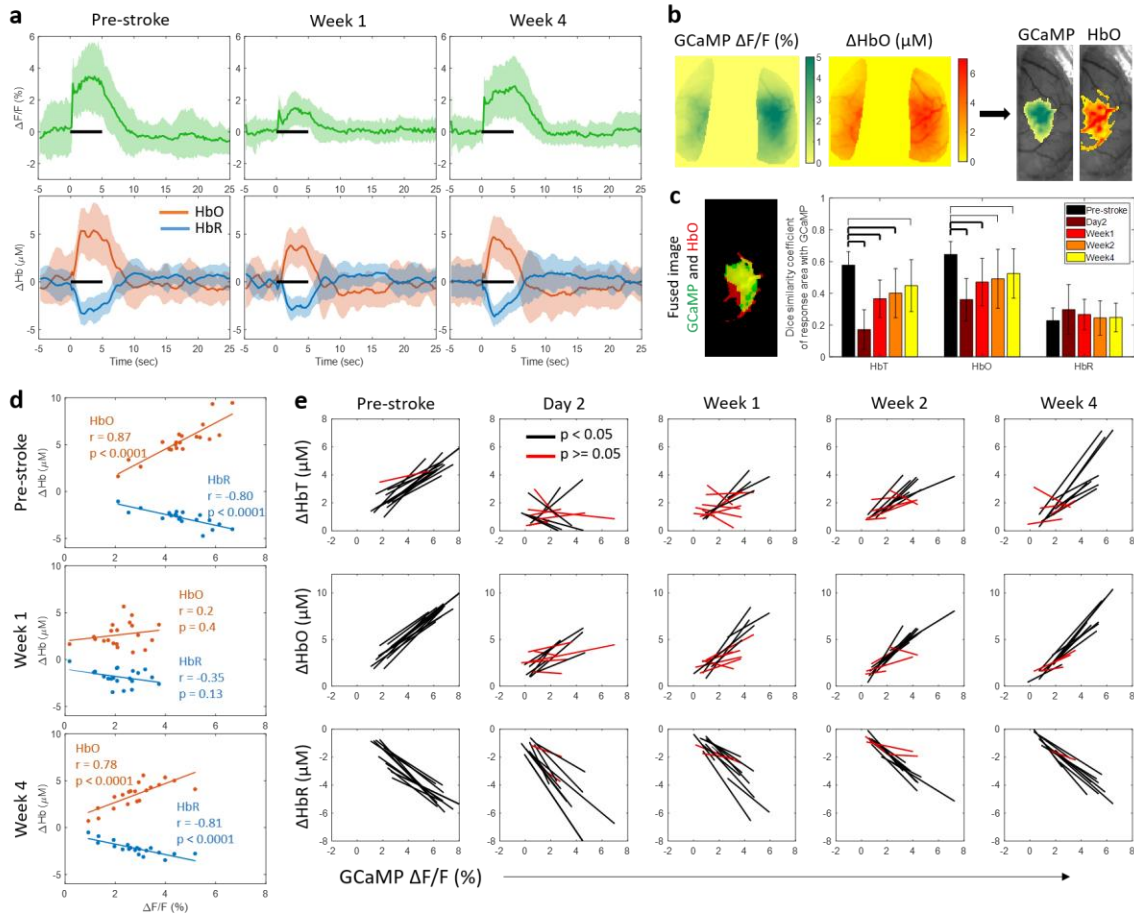


**Figure 5.2: Correlation between evoked calcium and hemodynamic responses**

(a) Trial-averaged timecourse showing mean ( $\pm$  std) of GCaMP (top) and HbO and HbR (bottom) of all pixels within the affected hemisphere at pre-stroke, 1 week, 4 weeks. Note the drop in response to stimulation (black bar) at week 1. (b) Threshold algorithm applied to GCaMP and Hb responses. (c) Overlap between response area of GCaMP and HbO, left: single trial fused image for reference, GCaMP is green, HbO is red, and overlap region is yellow, right: dice similarity coefficients across all mice ( $n=12$ ) and time points. Thick bars:  $p < 0.01$ , thin bars:  $p < 0.05$ . (d) Correlation of response magnitudes between GCaMP and HbO and HbR for one mouse at pre-stroke, week 1, and week 4. Inset numbers represent correlation value and significance of fit. (e) Correlation of calcium and hemodynamics across all mice ( $n=12$ ) over all time points, each line represents one mouse. Black lines represent significant correlation and red lines represent no significance.

*5.4.3 Acute stroke leads to neurovascular uncoupling within the peri-infarct that is restored in the chronic phase*

The next question we asked was whether neurovascular coupling was preserved across the acute and chronic phases of stroke recovery. To quantify neurovascular coupling we estimated a hemodynamic response function (HRF), which is the kernel that, when convolved with the GCaMP calcium signal, approximates the hemodynamic activity. Linear least-squares deconvolution was used to estimate the HRF as established previously in section 5.3.6<sup>172,194</sup>. First, to validate the method prior to stroke, we calculated the HRF for all pixels that responded to forelimb air-puff stimulation with HbT (Figure 5.3a, top). We observed the expected and characteristic shape of the HRF as reported previously. The same procedure applied to the stroke region, which includes the original forelimb, 2 days following stroke resulted in a distinct HRF shape, suggesting a disruption to neurovascular coupling (Figure 5.3a, bottom). Figure 5.3b shows the time course of four individual stimulation trials with the measured GCaMP signal overlaid with the measured and estimated HbT, obtained by convolving the GCaMP signal and the HRF kernel. Pre-stroke measured and estimated HbT showed good overlap (Figure 5.3b, top), while the measured and estimated HbT at day 2 (Figure 5.3b, bottom) showed poor overlap. Additionally, there was a lack of response to stimulation and we observed large oscillations in the measured hemodynamic signal at day 2. A Pearson's correlation coefficient was calculated between the measured and estimated HbT signal at each pixel for both hemispheres of the brain (Figure 5.3c) and we observed high correlation across the somatosensory cortex of both hemispheres before the stroke (Figure 5.3c, top). From this we can conclude that

hemodynamic activity was coupled to the calcium activity prior to stroke. Regions closer to motor cortex showed lower correlation compared to regions within sensory cortex. Higher correlation in the sensory cortex could be due to the increased cortical activity because of external stimuli driving both calcium and hemodynamic responses and strengthening neurovascular coupling. This hypothesis could be validated by comparing the HRF and correlation obtained during resting-state and sensory stimulation sessions. Prior work has shown that neural activity is more weakly correlated to hemodynamics during resting state and this can also be validated from our data (Supplementary Figure 5.13)<sup>195</sup>. Our resting-state data still shows a relatively high correlation, which could be due to natural behavior of the mouse, such as whisking and grooming, driving cortical activity. At day 2 after stroke there was a loss in correlation between the measured and predicted HbT, as indicated by drop in the Pearson's correlation coefficient (Figure 5.3c, bottom).

The same neurovascular coupling model was applied to calcium and hemodynamic data to estimate the HRF post-stroke. The post-stroke HRF was calculated for the stroke core, the peri-infarct region, which included all the pixels within 0.5 mm of the stroke core, and the contralesional forelimb region. The HRF was also calculated for HbO and HbR in addition to HbT. Figures 5.3d,f show the same reference mouse where the stroke core, peri-infarct, and contralesional forelimb are highlighted in black. We then followed the evolution of the HRF for each hemodynamic measure after stroke. Figure 5.3e shows the mean and standard deviation of the HRF for one example mouse. We observed a significant deviation in the HRF within the stroke core and peri-infarct in the acute phase of recovery. Following the acute phase, the chronic phase showed a recovery in the HRF. The

contralesional HRF remained largely unaffected by the stroke. Similar trends were observed across all animals (Figure 5.3g), where acute stroke resulted in deviation of the HRF in the core and peri-infarct, while the contralesional hemisphere was unaffected. In the chronic phase the HRF showed better recovery of the shape, with respect to pre-stroke HRF, in the peri-infarct. The HRF within the stroke core continued to show deviation in some animals.

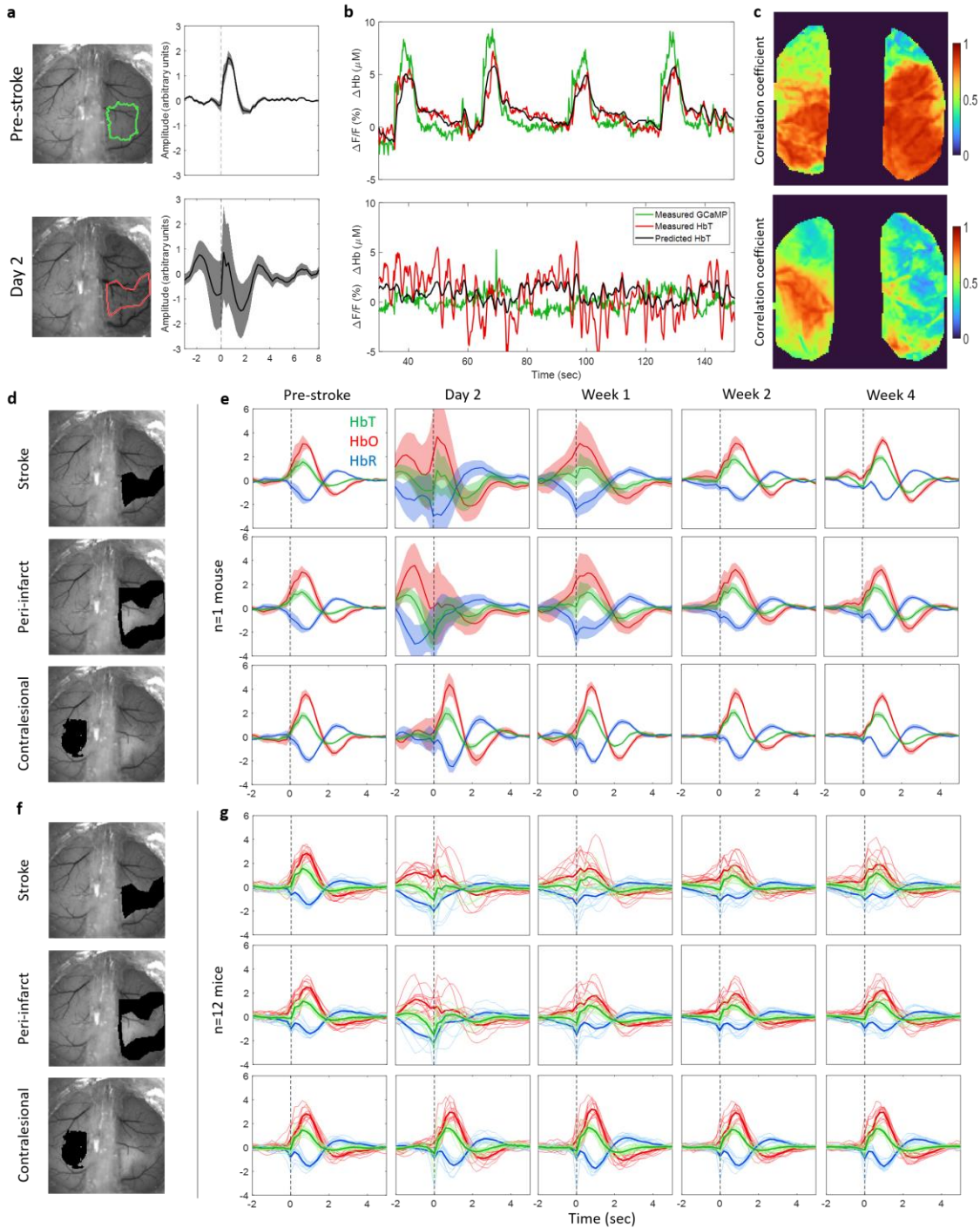


**Figure 5.3: Neurovascular coupling with linear least-squares deconvolution**  
 (a) Hemodynamic response function (HRF) before (top) and 2 days after stroke (bottom) in the forelimb and stroke regions outlined in green and red respectively. (b) Time course of 4 stimulation trials showing measured GCaMP signal overlaid with measured HbT and predicted HbT, obtained by convolving the GCaMP signal with the HRF kernel, at pre-

stroke and day 2 for the regions outlined in (a). (c) Pearson's correlation coefficient for measured HbT and predicted HbT for pre-stroke (top) and 2 days after stroke (bottom). (d) Regions used to extract HRF in (e) and (f). (e) HRF obtained by deconvolution model for HbT, HbO, and HbR, for one example mouse at each time point before and after stroke. Note the deviation in HRF compared to pre-stroke in the acute phase within the stroke and peri-infarct, and a return to pre-stroke HRF at week 4. (f) Same as in (e) for all mice ( $n=12$ ). Each line represents the HRF for one mouse.

Here, we describe deviation of the HRF in terms of the qualitative similarity of shape to the pre-stroke HRF. However, even if the shape of the HRF is different, it could still be used to accurately predict hemodynamics. Therefore, we next tested the ability of the HRF at each time point to predict hemodynamics. Figure 5.4a shows a pixel-by-pixel map of the Pearson's correlation coefficient for one example mouse for all three hemodynamic measures before and after stroke. We observed a clear drop in correlation coefficient within the affected hemisphere, specifically in day 2. Over the recovery period we observed some return of correlation between the measured and predicted hemodynamics. The correlation coefficient was quantified across all mice in the stroke core, peri-infarct, and contralateral forelimb region (Figure 5.4b). The stroke core showed a significant reduction in correlation coefficient across all time points compared to pre-stroke, implying that the hemodynamic response captured the underlying neuronal activity significantly poorly compared to pre-stroke. Additionally, this shows that the deviation in shape of the HRF was also associated with a lack of correlation between measured and predicted hemodynamics. There was also a significant decrease in the ability of the neurovascular coupling model to capture the hemodynamics from the measured GCaMP signal within the peri-infarct in the acute phase of day 2 and week 1. However, unlike the stroke core, the peri-infarct showed recovery in terms of reestablishing the correlation

between the measured and predicted hemodynamics in the chronic phase, which was associated with a return of HRF shape to pre-stroke.

From the shape of the HRF we can clearly see that the neurovascular coupling model is not behaving as expected. Most notably, we see that the HRF is not flat in negative time. We have provided more flexibility in our model by allowing it to use GCaMP events that have not happened yet to find the best fit. In the pre-stroke case this negative-time region is a flat line, indicating that future GCaMP events have no influence on the current hemodynamics, as expected. However, after stroke, specifically at day 2 and week 1, the HRF is no longer flat before zero. While it is physiologically not possible for future GCaMP events to influence current hemodynamics, this deviation in the HRF indicates that there are possibly additional dynamics that are not captured by the original model and the model is just trying to find the best fit with the given data. We can overcome this limitation and test deviation in neurovascular coupling by testing how well we are able to predict the post-stroke hemodynamics with the pre-stroke HRF, since we know that the pre-stroke HRF is behaving as expected. To test this we calculated the mean HRF for each mouse from pre-stroke data and convolved it with the post-stroke GCaMP timecourse and obtained the correlation with this predicted and measured hemodynamics (Figure 5.4c). Similar to before, there was a significant drop in correlation within the stroke and peri-infarct regions in the acute phase and a recovery within the peri-infarct in the chronic phase (Figure 5.4d). Unlike before, there was virtually no correlation between the measured and predicted HbT and small correlation in HbO at day 2. This suggests that the neurovascular coupling model described for healthy brains is not sufficient to describe post-stroke

neurovascular dynamics. The stroke core continued to show poor correlation even at week 4 but the peri-infarct had recovered.

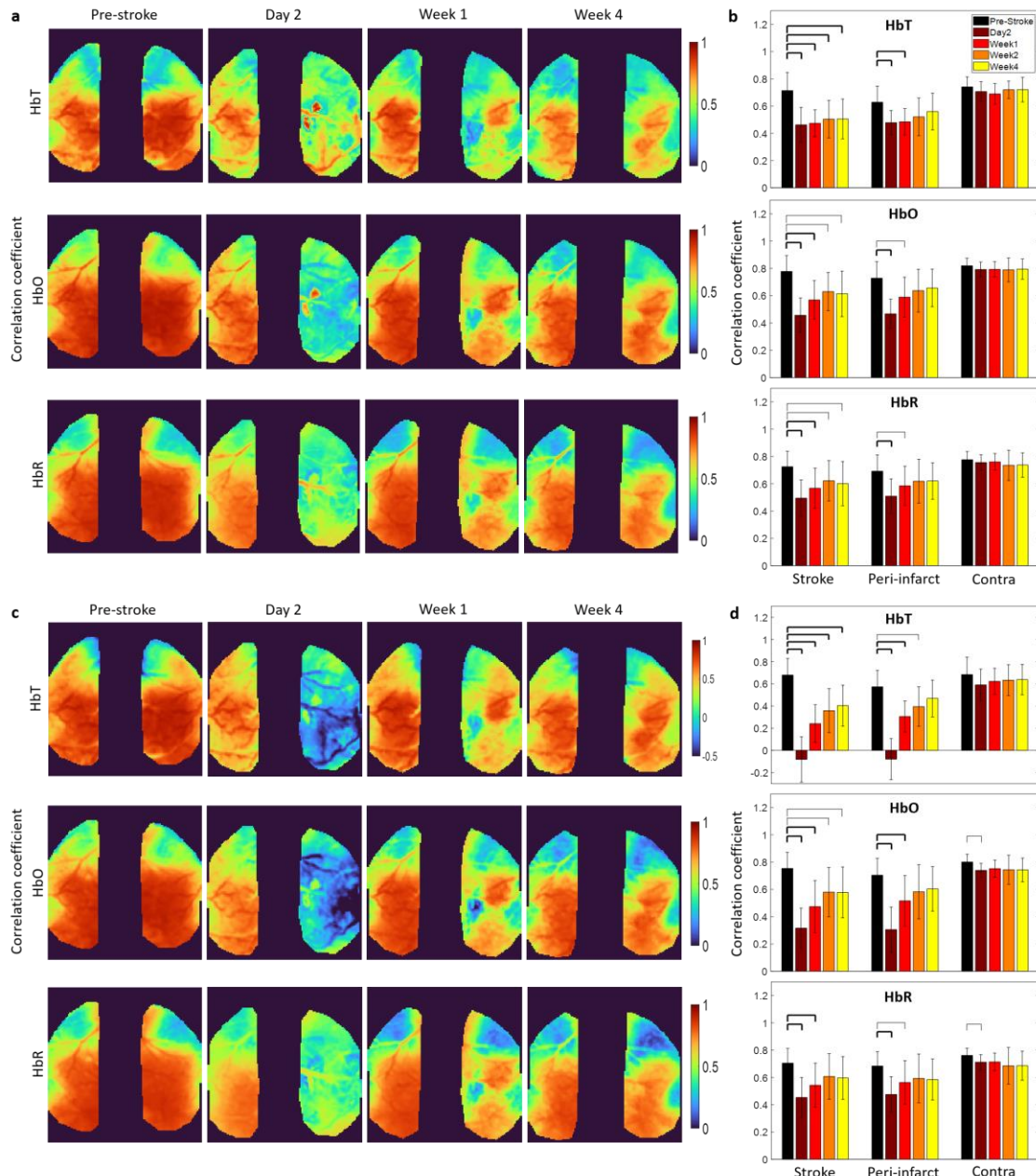


**Figure 5.4: Ability of the hemodynamic response function (HRF) to predict hemodynamics**

(a) Pixel-by-pixel Pearson's correlation coefficient between measured and predicted HbT (top), HbO (middle), and HbR (bottom). Predicted HbX is obtained by convolving the GCaMP signal at each time point with the HRF obtained for that specific time point and

pixel. (b) Pearson's correlation coefficient quantified across all mice within the stroke core, peri-infarct, and contralateral forelimb region. Thick bars:  $p < 0.01$ , thin bars:  $p < 0.05$ . (c) Pixel-by-pixel Pearson's correlation coefficient between measured and predicted HbT (top), HbO (middle), and HbR (bottom). Predicted HbX is obtained by convolving the GCaMP signal at each time point with a mean HRF obtained from pre-stroke data. (d) Pearson's correlation coefficient quantified across all mice within the stroke core, peri-infarct, and contralateral forelimb region. Thick bars:  $p < 0.01$ , thin bars:  $p < 0.05$ . Note the sustained reduction of correlation coefficient within the stroke core but recovery within the peri-infarct for HbT and HbO.

#### *5.4.4 Acute stroke leads to increases in global brain oscillation power*

Stroke is known to have a profound effect not only on the local network but also on the contralateral and subcortical networks of the brain. In our neurovascular coupling analysis we observed an increase in oscillatory dynamics in the hemodynamic signal. Through our wide-field imaging approach we can assess the effect of stroke on both hemispheres of the brain during resting state. To assess brain-wide variations in the signals, we first investigated the overall change to signal patterns. Figure 5.5a shows the resting-state time traces of GCaMP and HbO signals at pre-stroke and 2 days post-stroke within the ipsilesional peri-infarct (Figure 5.5a, top) and the contralateral forelimb regions (Figure 5.5a, bottom) that was filtered at 0.009-0.4Hz, which covers the low and high frequency hemodynamic signal ranges used in prior work. A feature of note here is the increase in amplitude of the HbO signal at day 2 in the ipsilesional hemisphere (light red line in Figure 5.5a top) compared to pre-stroke, but an increase in amplitude of both the HbO and GCaMP signal at day 2 within the contralateral hemisphere. We validated this increase in amplitude by calculating the variance in the overall signal (Figure 5.5b). GCaMP showed only minor alterations in variance while HbO showed a large increase in

the variance of its signal at day 2 which was resolved by week 4. We next asked whether this increase in the amplitude of the signal was an increase in the power of the signal across all frequencies or if it was specific to any particular frequency. To address this, we calculated the power spectrum of the GCaMP and hemodynamic signal within the affected and unaffected hemispheres (Figure 5.5c). There was an overall increase in power across all frequencies at 2 days after stroke in the HbO signal of the ipsilesional hemisphere. Moreover, there was a significant increase in power of the hemodynamic signal at 2 days and 1 week after stroke, specifically around 0.25 Hz within the ipsilesional hemisphere. The contralesional hemisphere on the other hand showed increased power at 0.25 Hz at day 2 after stroke in both GCaMP and hemodynamics. Figure 5.5d shows the area under the curve in the frequency range of 0.1-0.3 Hz, where the largest increase in power was observed. This increase in power at 0.25 Hz, which is typically higher than normal for hemodynamics, could be a result of increased vasomotion. Evidence from prior work in human laser doppler flowmetry and magnetoencephalography (MEG) has suggested that stroke-affected arterioles showed elevated power<sup>196,197</sup>.

We then asked if this increase in power of the GCaMP, in the contralesional hemisphere, and hemodynamic signal, in both hemispheres, was uniform across the hemispheres or specific to any distinct brain region. Figure 5.5e shows spatial maps of the average power for GCaMP and HbO for an example mouse. We clearly see increased power in GCaMP in the contralesional hemisphere and increased overall power in HbO at day 2 and week 1 compared to pre-stroke. Surprisingly, the increase in GCaMP power appeared specific to the contralesional forelimb region, while the power increase in HbO

appeared global. This was validated across all mice (Figure 5.5f), which showed that there was a significant increase in power only within the contralesional forelimb and not the rest of the contralesional hemisphere. The HbO signal, on the other hand, showed increases across all regions. There was also a decrease in the GCaMP signal within the ipsilesional forelimb region in the chronic phase, likely due to the death of neurons within that region.

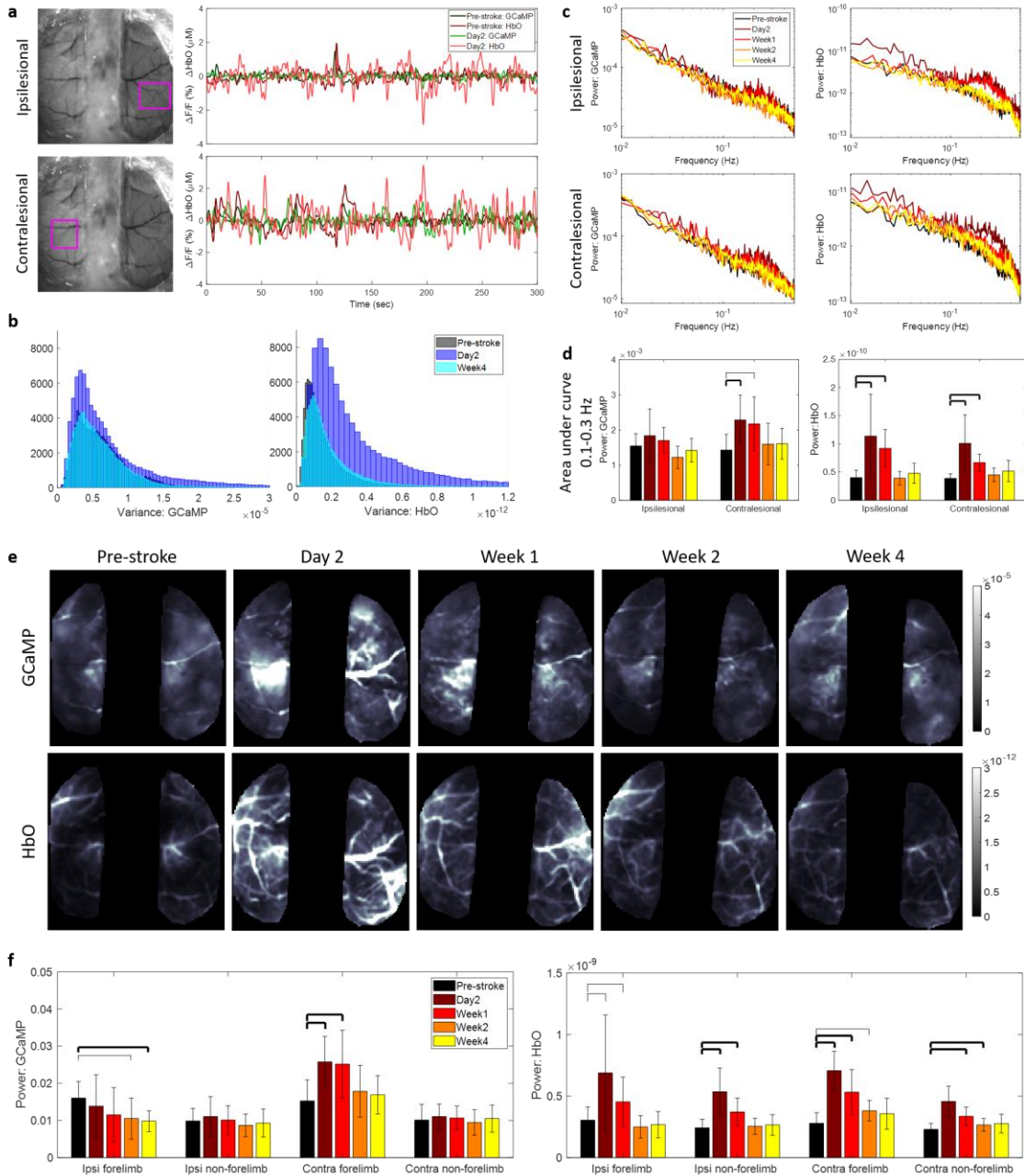


**Figure 5.5: Global brain oscillations following stroke**

(a) Raw time traces of filtered (0.009-0.4 Hz) calcium and hemodynamic signals before and 2 days after stroke within the ipsilesional (top) and contralesional (bottom) hemispheres in ROI marked with pink box. Note the increase in amplitude of HbO in both hemispheres at day 2 and increase in GCaMP amplitude only in the contralesional hemisphere. (b) Histogram of variance in the mean signal, after global signal regression, for GCaMP (left) and HbO (right) at pre-stroke, day 2, and week 4. (c) Frequency spectrum of the power of the GCaMP (left) and HbO (right) signal in the ipsilesional (top) and

contralesional (bottom) hemispheres. (d) Area under the curve within 0.1-0.3 Hz frequency band. Thick bars:  $p<0.01$ , thin bars:  $p<0.05$ . (e) Spatial maps of average power across 0.009-0.4 Hz frequency band for GCaMP (top) and HbO (bottom) at each time point. (f) Mean power assessed in each hemisphere within the forelimb and non-forelimb areas. Thick bars:  $p<0.01$ , thin bars:  $p<0.05$ .

#### *5.4.5 Photothrombotic stroke disrupts resting state interhemispheric functional connectivity only in the early acute phase*

Stroke has also been known to affect functional connectivity across large scale brain networks. To address the possibly differential effects of stroke on calcium and hemodynamic global brain dynamics we asked whether resting state functional connectivity (RSFC) showed similar dynamics during the recovery phase. Prior work in healthy animals has showed that at low (0.009-0.08 Hz) and high (0.08-0.4 Hz) frequency bands, which are typically used in BOLD-fMRI and functional connectivity IOSI studies, functional connectivity structures between GCaMP and HbO were in high agreement<sup>155</sup>. But as applications of hemodynamic RSFC are extended into the stroke field, it is important to understand not only the underlying physiology that those signals represent but also what aspects of connectivity are altered and sensitive measures for the stroke<sup>49,193</sup>.

To that end, we looked at various aspects of RSFC in the low and high frequency bands across GCaMP and HbO maps. First, we assessed connectivity of the ipsilesional forelimb area to the contralesional hemisphere (Figure 5.6a). In healthy pre-stroke animals, seed-based forelimb connectivity maps were consistently normal, while acute stroke showed alterations in forelimb connectivity to the contralesional hemisphere. Figure 5.6a(i) shows the forelimb connectivity maps for GCaMP at pre-stroke, day 2, and week 4 in the

low frequency band. We then quantified the differences between pre-stroke and post-stroke time points by calculating the proportional area of the cortex above correlation coefficients over a range of thresholds from 0 to 0.9 (Figure 5.6a(ii)). A slight decrease in connectivity was observed in the GCaMP map and a large decrease was observed in HbO at 2 days post-stroke (Figure 5.6a(ii), Supplementary Figure 5.14a). HbO continued to show reduced forelimb connectivity at all time points after stroke at specific thresholds (Supplementary Figure 5.14a); however, GCaMP appeared largely resolved at later time points. A Dice similarity index was calculated between the GCaMP and HbO maps across all thresholds, which showed a deviation in similarity only at day 2 after stroke, while maps were consistent at all other time points (Figure 5.6a(iii), Supplementary Figure 5.14a). A similar approach was used for calculating interhemispheric connectivity, global connectivity, and contralateral forelimb intrahemispheric connectivity as well as all measures in the higher frequency band. Trends across time points and thresholds for all measures were largely similar in both frequency bands. There was a significant drop in interhemispheric connectivity at 2 days in both GCaMP and HbO, which was resolved at later time points in GCaMP but continued to persist, to a lesser extent, in HbO until week 1 (Figure 5.6b,f). Surprisingly, there was a small but significant increase in global connectivity at day 2 in GCaMP (Figure 5.6c,g, Supplementary Figure 5.14c). Spontaneous recovery over four weeks resulted in reestablishment of global connectivity networks in both GCaMP and HbO. Since we observed increase in the calcium power within the contralateral hemisphere (Section 5.4.4), we also asked whether contralateral forelimb connectivity was altered. We observed a significant increase in contralateral forelimb connectivity

within the contralesional hemisphere at day 2 after stroke (Figure 5.6d,e). This suggests that increases in the power of the calcium signal within the contralesional forelimb were associated with an increase in its functional connectivity to other regions of the brain. The increase observed in the global connectivity index could be due to this increased connectivity of the contralesional forelimb.

From these data we extrapolate that connectivity of both the impaired and unimpaired forelimb and interhemispheric connectivity for both GCaMP and HbO were strong measures to indicate stroke, given our photothrombotic model, at day 2. Disruptions to interhemispheric connectivity persisted until week 1 after stroke but other metrics assessed were indistinguishable from pre-stroke. While global connectivity provides a concise method as a seed-independent approach of functional connectivity, in our case it was a weaker metric for following the stroke recovery process.

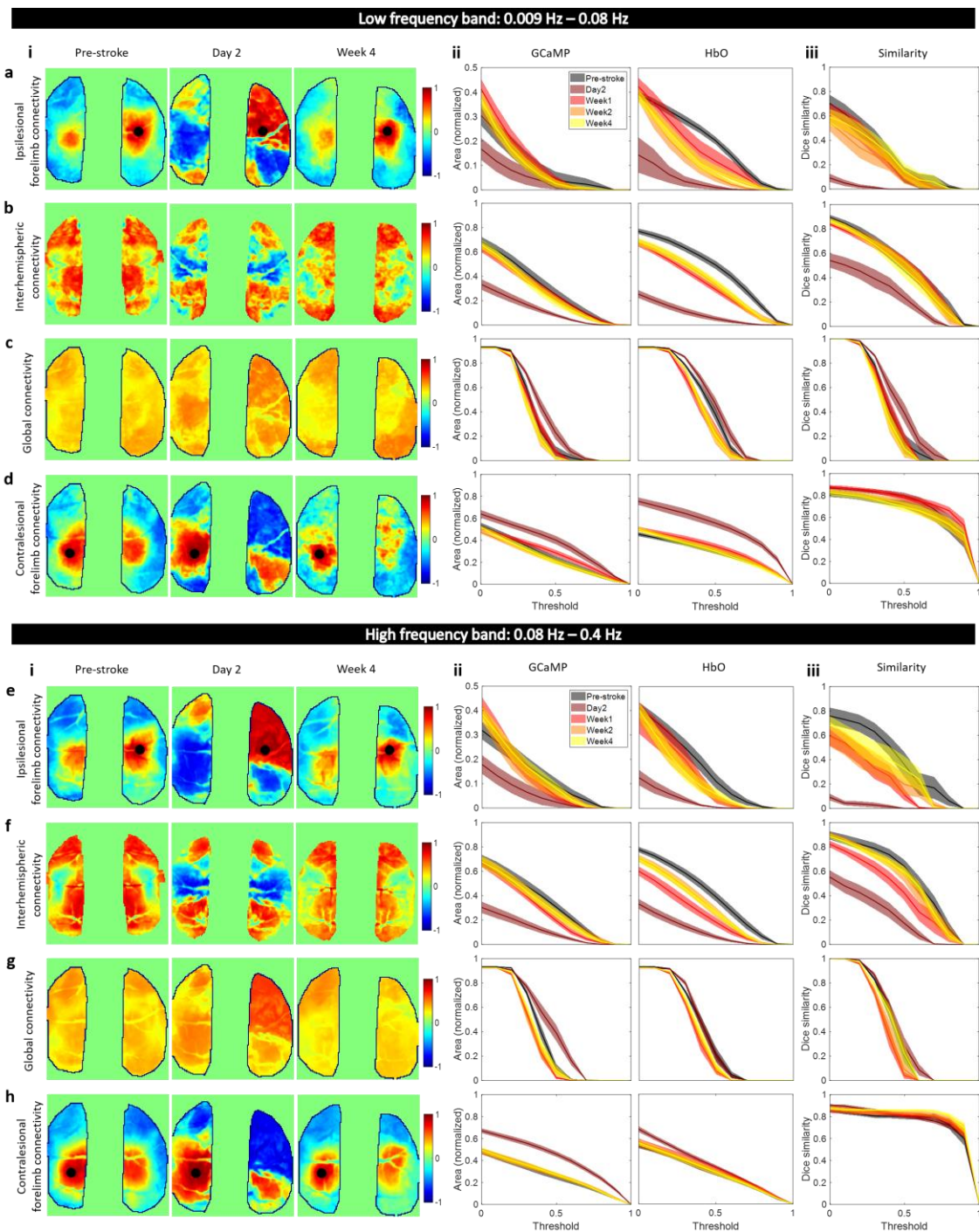


**Figure 5.6: Global brain network dynamics assessed with RSFC**

Spatial maps of ipsilesional forelimb connectivity (a(i),e(i)), interhemispheric connectivity (b(i),f(i)), global connectivity (c(i),g(i)), and contralateral forelimb connectivity (d,h) at pre-stroke, day 2, and week 4. Proportional area of cortex over threshold for GCaMP and HbO at each time

point for ipsilesional forelimb connectivity (a(ii),e(ii)), interhemispheric connectivity (b(ii),f(ii)), global connectivity (c(ii),g(ii)), and contralesional forelimb connectivity (d(ii),h(ii)) in the low frequency band (a,b,c,d) and in the high frequency band (e,f,g,h). Dice similarity coefficient for overlap between area covered by GCaMP and HbO for ipsilesional forelimb connectivity (a(iii),e(iii)), interhemispheric connectivity (b(iii),f(iii)), global connectivity (c(iii),g(iii)), and contralesional forelimb connectivity (d(iii),h(iii)) at all time points in the low frequency band (a,b,c,d) and the high frequency band (a,b,c,d).

#### *5.4.6 Correlating cortical metrics to long-term behavior outcomes*

To enable translation of the cortical measures investigated in this work to potentially clinically relevant outcomes, we measured forelimb performance through the cylinder asymmetry test before stroke and at each time point after stroke. Photothrombotic stroke to the forelimb somatosensory area led to deficits in the use of the impaired forelimb (Figure 5.7a). On average, mice used their impaired forelimb 50% less than baseline in the first week following stroke; however, over time with spontaneous recovery, mice showed a significant increase in the use of the impaired forelimb by week 4 compared to day 2 (Figure 5.7a). An important factor in human strokes that is often missed in animal models is the variability in the extent of damage and impairment caused by the stroke. The extent and location of the damage due to stroke, as well as the early spontaneous recovery mechanisms play a significant role in long-term outcomes<sup>5,188,198</sup>. A number of early biomarkers that might have potential as indicators of behavioral outcomes are under active investigation in both human patients and in animal studies<sup>199,200</sup>. While it would be ideal to introduce a controlled level of variability into animal models to study variable recovery and biomarkers for recovery, such a method of stroke induction that also meets all the other criteria for a physiological stroke, such as preventing the use of anesthesia during stroke

does not yet exist. Our optimized photothrombotic model introduces uncontrolled variability that mimics human variability to some extent and allows correlation of behavioral outcome to cortical biomarkers. The right panel of Figure 5.7a shows the extent of recovery in forelimb asymmetry for individual mice at week 4. In this section we outline how cortical measures obtained in all the previous sections correlate to these variable long-term behavioral outcomes.

First, since the cylinder test is sensitive to forelimb use, we tested whether the extent of forelimb area that was damaged due to stroke predicted behavioral outcomes. We calculated the percent overlap between the pre-stroke forelimb region and the stroke outline obtained from SFDI at 1 week after stroke (Figure 5.7b). There was a significant negative correlation, indicating that worse behavior outcomes correlated with a larger portion of the forelimb being damaged by the stroke. We next asked whether functionality in the surviving portion of the forelimb promoted behavior. Here, we calculated the magnitude of responses within the original forelimb region for GCaMP and hemodynamics at week 1. Both GCaMP and hemodynamics showed trends towards a positive correlation between response magnitude and better outcomes, with only the HbT showing a significant correlation (Figure 5.7b). Next we assessed the relationship between acute neurovascular coupling and behavior outcomes. This was calculated in two ways, the first with the correlation coefficients obtained from the magnitude of evoked responses between GCaMP and HbT at week 1 during forelimb stimulation (Figure 5.7c, data from Figure 5.2). The correlation coefficient of evoked responses significantly correlated with behavior. The second was with the correlation coefficients obtained from the neurovascular coupling

model between the measured and estimated HbT at week 1 (Figure 5.7d). This too showed a significant correlation with behavior implying that preserved or improved neurovascular coupling at week 1 might be indicative of better long-term recovery.

We performed similar calculations with the global brain metrics of power of the signal and interhemispheric connectivity from RSFC. Average power was calculated within the narrow frequency band (0.15–0.3Hz) for both GCaMP and hemodynamics and separated into ipsilesional and contralesional hemispheres. While GCaMP did not show any trends with behavior, acute hemodynamic oscillations showed strong positive trends with behavior outcomes (Figure 5.7e). Specifically, increased power in the HbT signal of the contralesional and ipsilesional hemispheres in the acute phase of stroke significantly correlated with behavior outcomes. Interhemispheric connectivity at week 1, or any other RSFC metric, did not show any correlations with long-term behavior outcomes, further implying that RSFC might not be a sensitive metric for targeted photothrombosis. Overall, we have identified a number of cortical metrics within the acute phase of stroke recovery that had the potential to delineate animals that show better spontaneous recovery from animals that had poorer recovery.

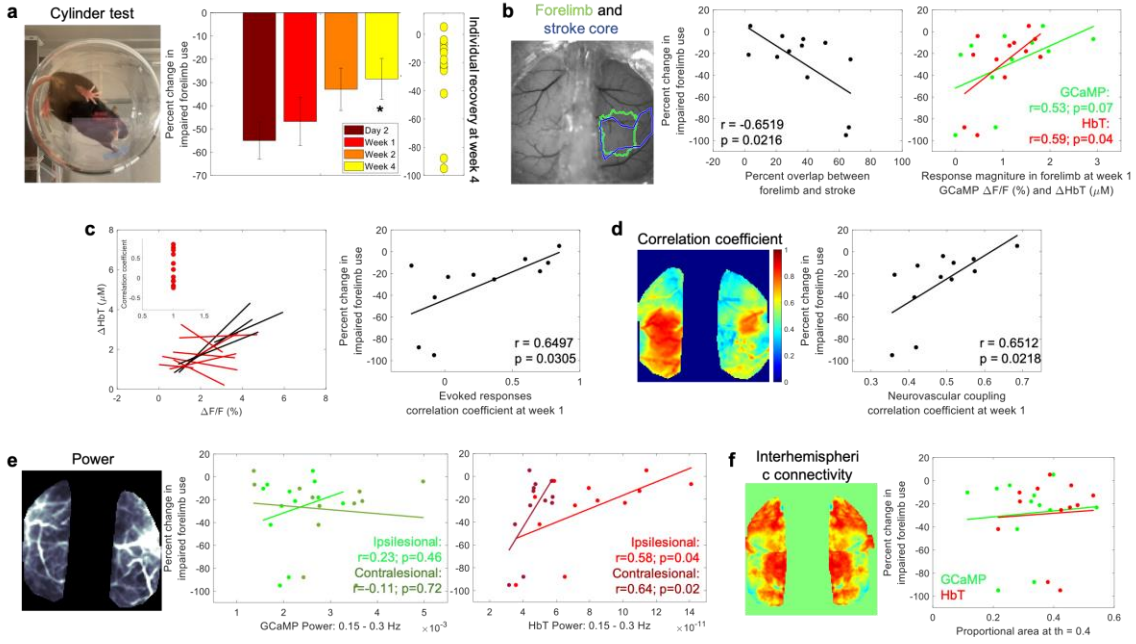


**Figure 5.7: Correlating cortical metrics to behavior outcomes**

(a) Forelimb asymmetry, assessed with the cylinder test, calculated as a change in impaired forelimb use from pre-stroke, right: recovery of individual mice at week 4. (b) Left: reference image showing outlines of pre-stroke forelimb region and stroke core at 1 week, middle: correlation between overlap of forelimb and stroke with forelimb asymmetry at week 4, right: correlation between response magnitude at week 1 for GCaMP and HbT with forelimb asymmetry at week 4. (c) Left: correlation of evoked responses of GCaMP and HbT, right: correlation between the correlation coefficient of evoked responses at week 1 and forelimb asymmetry at week 4. (d) Left: correlation coefficient between measured HbT and HbT predicted by convolving GCaMP and IRF, right: correlation between neurovascular coupling correlation coefficient at week 1 and forelimb asymmetry at week 4. (e) Correlation between power of GCaMP and HbT in frequency band 0.15-0.3 Hz in the ipsilesional and contralateral hemispheres and forelimb asymmetry at week 4. (f) Correlation between resting state interhemispheric connectivity and forelimb asymmetry at week 4.

## 5.5 Discussion

Despite the widespread use of functional neuroimaging for treating and monitoring patients in the acute and chronic phases of stroke recovery, the interpretations of these signals and their reliability as a neural correlates are still under active investigation. In this study, we used an animal model of stroke, optimized for high clinical relevance, to investigate the

relationships between neural activity, assessed with a fluorescent calcium indicator, and cerebral blood volume, assessed with changes in oxy- and deoxy-hemoglobin, during longitudinal stroke recovery. We showed that acute stroke leads to disruptions in neurovascular coupling, which is restored in the chronic phase. Neurovascular uncoupling was primarily experienced within the affected hemisphere, and early recoupling and recovery of cortical function within the preserved forelimb region and peri-infarct zone was an indicator of better recovery. Additionally, we showed that acute stroke leads to increases in global brain oscillations, which have distinct characteristics in GCaMP and hemodynamics.

This study has several implications for the interpretation of hemodynamic signals in terms of the underlying physiology both pre- and post-stroke. In the healthy brain, we showed that with simultaneous multi-modal imaging of calcium activity and hemodynamics we can track subtle differences in sensory evoked response dynamics on a trial-by-trial basis. This allowed us to correlate intra-animal changes to evoked responses across the cohort and at each time point after stroke. We correlated each animal's responses individually due to the variability in the extent of damage between animals introduced by our stroke model. This allowed us to track the changes of each animal individually; we found that there was a significant loss in correlation between evoked calcium and hemodynamic responses in the acute phase of day 2 and week 1. Correlation was reestablished in most animals by week 4, associated with spontaneous recovery and improved behavior. A small number of animals continued to show loss of correlation between evoked calcium and hemodynamic responses across both the acute and chronic

time points, and these animals were associated with poor behavior outcomes. There was also a significant positive trend between correlation of evoked responses, specifically between calcium and HbT, at week 1 and behavior outcomes at week 4 across all mice. Taken together with the significant correlation between early HbT response magnitudes within preserved forelimb and long-term behavior, this implies that early recovery of hemodynamic responses, HbT in particular, might be indicative of better outcomes.

While correlations of evoked calcium and hemodynamic response magnitudes allowed us to draw conclusions about the similarity of the two measures, it does not contain fine-grained quantitative information about their relationship. To quantitatively describe neurovascular coupling, we estimated hemodynamics from calcium activity using linear least-squares deconvolution as had been done previously<sup>172,183</sup>. Similar to previous reports, the measured calcium signal convolved with a calculated HRF kernel predicted the hemodynamic signal with high accuracy in healthy animals. There was a higher correlation within sensory regions of both hemispheres compared to more frontal or posterior regions, which could be due to sensory stimulation driving cortical activity within the somatosensory cortex and strengthening neurovascular coupling. The characteristic shape of the HRF was altered after acute stroke, which also corresponded to a significant decrease in the ability of the model to predict hemodynamics within the affected hemisphere. The correlation when using the pre-stroke HRF is significantly lower than the correlation when using the HRF from each post-stroke time point. This indicates that the model post-stroke is finding a best fit, which is not necessarily similar to the expected neurovascular coupling model. Using the expected neurovascular coupling model yielded significantly poorer

correlations. These results provide evidence suggesting that the neurovascular coupling model established in healthy animals is not representative of post-stroke acute phase dynamics and that the observed hemodynamic response is not an accurate representation of the underlying physiology, since the HRF was unable to predict hemodynamics accurately. However, it must also be noted that the model assumption of a linear relationship might not hold true after stroke, and the hemodynamic response might be better predicted with an altered non-linear model. Nevertheless, we see neurovascular recoupling, as measured by the linear model, in the chronic phase of recovery. We observed reestablishment of the expected HRF shape and the ability of the model to predict hemodynamics improved significantly, specifically in the peri-infarct. This suggests that functional neuroimaging might faithfully represent the underlying physiology in the chronic phase. Additionally, we found that early recovery of neurovascular coupling was associated with improved behavioral outcomes.

In addition to local changes to evoked responses and neurovascular coupling alterations within the affected hemisphere, stroke is known to have a profound impact on global cortical network dynamics such as contralateral and subcortical connectivity<sup>201</sup>. We found that there was an increase in overall power of the cortical signals in both calcium and blood volume in the acute phase, which was resolved in the chronic phase. The increase in power of the calcium signal appeared to be specific to the contralesional forelimb region, while the increase in hemodynamic power was global across all vessels and both hemispheres. A study conducted with laser doppler flowmetry showed increased oscillations within stroke affected arterioles and suggested increased vasomotion as the

cause<sup>197</sup>. Other studies have also showed increases in brain oscillations in stroke and traumatic brain injury<sup>37,196,202</sup>. Vasomotion, the oscillating tone of blood vessel independent of heart rate or breathing, is tightly regulated by various compartments of the neurovascular unit<sup>203,204</sup>. Vascular autoregulation is impaired after stroke and ionic imbalances in neuronal, astroglial, and endothelial cells could result in dysregulation of vasoactive molecules and ions and therefore vascular tone<sup>24,25</sup>. On the other hand, we also observed increases in power of GCaMP in the contralesional forelimb. Prior work has shown that stroke leads to increases in brain excitability and disruption of the interhemispheric inhibition through the corpus callosum<sup>205–207</sup>. This could reduce the inhibitory effects that the two hemispheres exert on each other, which could increase excitability within the contralesional hemisphere. There is also evidence of thalamic disinhibition within minutes of ischemic stroke that can unmask ipsilateral pathways<sup>208</sup>. The excitability of thalamocortical pathways contralateral to the stroke may be enhanced because of downregulation on interhemispheric thalamic inhibition. Surprisingly, we found that increased power in the hemodynamic signal in the contralesional hemisphere during the acute phase was correlated with improved behavior outcomes. Prior work has shown that stimulation of activity within the gamma frequency band improved cerebral blood flow, decreased infarct volume, and improved motor behavior, suggesting that modulation of cortical oscillatory dynamics may serve as a target for neuroprotection<sup>209</sup>. Other studies have also shown that increased brain oscillations and excitability promoted recovery in stroke as well as other neurological disorders and suggest their possible use as a biomarker for recovery<sup>37,205,206,210</sup>. A meta-analysis on activation data from over 50 neuroimaging

experiments have shown enhanced activity in the homotopic region of the contralesional hemisphere in the acute phase after stroke consistent with our finding<sup>33,34</sup>. This enhanced activity appears as spontaneous and synchronous neuronal activity and has been shown to be a signal for axonal sprouting and reorganization<sup>211</sup>. Taken together with this evidence, we could hypothesize that spontaneous increases in power that we observed in hemodynamic activity might play a role in promoting recovery mechanisms. These oscillations are possibly driven by underlying neuronal activity at frequencies higher than GCaMP, which we are unable to capture due to the slow calcium dynamics compared to neuronal activity.

A growing number of studies are now using RSFC to assess spatiotemporal correlations in spontaneous hemodynamic signals across different brain regions in healthy and diseased states. In the healthy brain, hemodynamic signals have been found to be bilaterally correlated and synchronized temporally in functionally distinct brain regions and represent the connectivity of underlying intrinsic neural fluctuations<sup>172,178,212</sup>. RSFC has also been used as a sensitive assay to monitor progression of stroke and hemorrhage with the assumption that the altered connectivity represents an altered neuronal state<sup>49,193</sup>. In this study we show that RSFC of spontaneous calcium activity and hemodynamics show similar trends after stroke, validating prior assumptions. Forelimb and interhemispheric connectivity were disrupted significantly in the very early acute phase and was resolved within week 1 in both calcium and hemodynamics. Moreover, we found that RSFC measures were not sensitive to behavioral outcome. This could be because global brain connectivity is more robust to small strokes caused by targeted photothrombosis to the

forelimb. A prior RSFC study also showed that somatosensory connectivity was not predictive of behavior, but that motor and retrosplenial cortices might be better predictors<sup>49</sup>. Due to our window preparation procedure and headbar design for multimodal optical access, our field of view was mainly limited to the somatosensory region and we were unable to fully capture connectivity to other brain regions. It is also possible that more sensitive analyses are needed for RSFC to serve as a metric for stroke outcome. We also tested whether increases in power of the calcium activity within the contralesional forepaw was associated with increased functional connectivity through RSFC. We found that intra-contralesional hemisphere connectivity was significantly increased at day 2. This suggests that increased excitability within the contralesional forepaw might result in its increased functional connectivity to surrounding regions as well as the ipsilesional peri-infarct, as seen from the spatial maps of connectivity. Further investigation is needed to understand the link between excitability and functional connectivity and its impact on recovery.

An important factor to note in our study is that we measure calcium dynamics from only excitatory cells. We know, from decades of prior work, that both excitatory and inhibitory cells have important and distinct roles to play in maintaining cortical balance<sup>213</sup>. Additionally, a number of other cell types, such as astrocytes and pericytes, as well as vasomodulators are involved in regulating blood flow to meet the metabolic demands of the brain<sup>18,19,22</sup>. We also know that these different cell types are impacted differently after stroke<sup>11,12,187</sup>. While we used mice with labelled excitatory neurons, the same imaging platform and experimental design can be used to investigate the contributions of other cell types, such as inhibitory cells and glia, to alterations in neurovascular coupling after stroke.

Additionally, calcium activity assessed with GCaMP6f has been validated to be a reliable measure of neural activity but it is not a direct measure. Fast neural dynamics or sub-threshold dynamics may be missed in calcium imaging, since the dynamics of calcium are much slower than action potentials or local field potentials. Although performing similar experiments while capturing local field potentials would allow us to assess neuronal activity directly and provide a higher temporal resolution, we do not believe that using GCaMP has affected our measures neurovascular coupling as all our experiments are performed at a temporal resolution higher than what is needed for hemodynamics assessment.

In summary, by simultaneously capturing changes to calcium activity and hemodynamics we have assessed various aspects of neurovascular coupling during the acute and chronic phases of stroke recovery. Our data suggests that acute stroke leads to neurovascular uncoupling, implying that functional neuroimaging might not be representative of the underlying activity and we need to use caution when interpreting the results. Neurovascular coupling is restored in the chronic phase, suggesting that functional neuroimaging is more faithfully representing the underlying neuronal activity chronically. Moreover, early recovery of neurovascular coupling and increased power of brain oscillations were predictors of better long-term behavioral outcomes.

## 5.6 Supplementary material

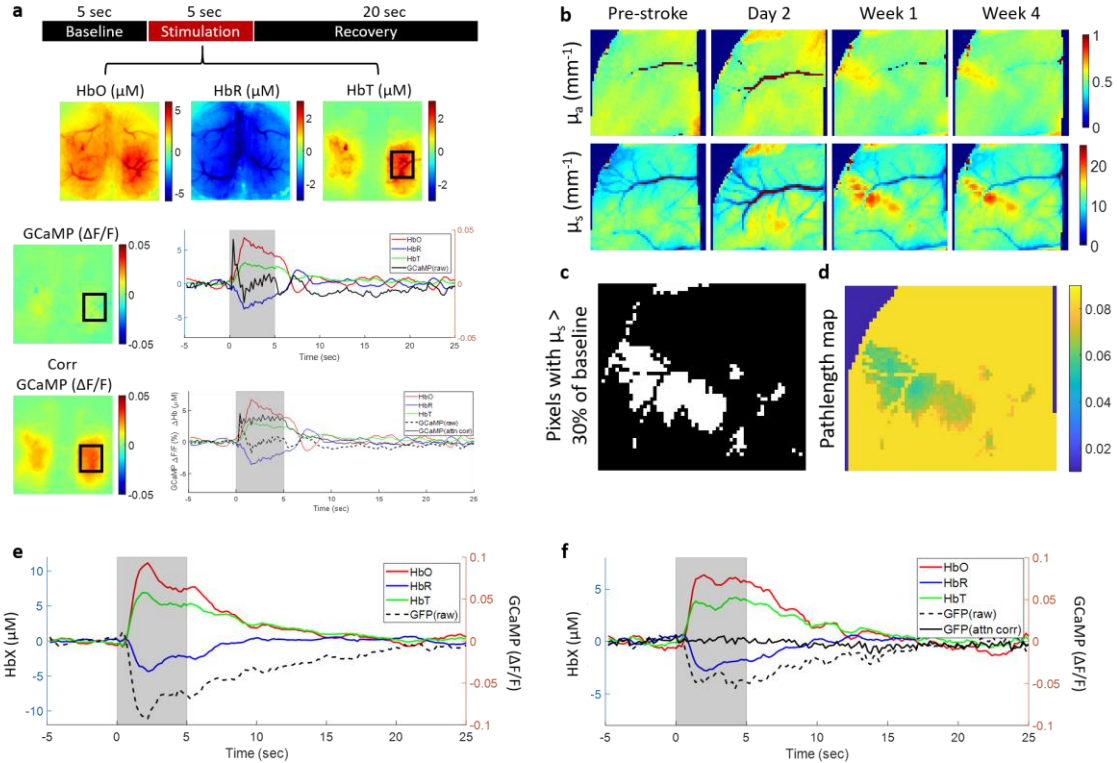


**Figure 5.8: Fluorescence correction for hemodynamic crosstalk**

(a) Top: Block design of single sensory stimulation trial and spatial hemodynamic response maps for HbO, HbR, and HbT. Middle: Raw GCaMP response map during 5 sec of sensory stimulation and time course of trial averaged data for GCaMP and hemodynamics from ROI marked in black box. Uncorrected GCaMP shows rise in fluorescence at the start of stimulation but begins to decrease with the rise of hemodynamic response. Bottom: Spatial map of GCaMP corrected for hemodynamic crosstalk. Note the appearance of response compared to uncorrected GCaMP in spatial map. Time course of corrected GCaMP overlaid with uncorrected GCaMP and hemodynamics. Note that GCaMP is now elevated for the full stimulation period. (b) Absorption and scattering coefficients obtained from SFDI before and after stroke and used in the correction algorithm in the form of pathlength factor. Stroke leads to increases in the scattering signal that needs to be accounted for accurate correction due to its effect on pathlength. (c) Binary maps of all pixels that have scattering coefficient greater than 30% of baseline scattering. The scattering and absorption coefficients from these pixels are used in the Monte Carlo simulation to obtain pathlength. (d) Spatial map of pathlength factors obtained from Monte Carlo simulations and used in the correction algorithm. (e,f) Validation of correction algorithm with cellular fluorescent marker GFP. (e) GFP signal overlaid with hemodynamics during 5sec of sensory stimulation. GFP drops in association with hemodynamic increase. (f) Correction applied to GFP signal during sensory stimulation. Corrected GFP is a flat line as expected since GFP fluorescence is not altered with neural activity or hemodynamics.

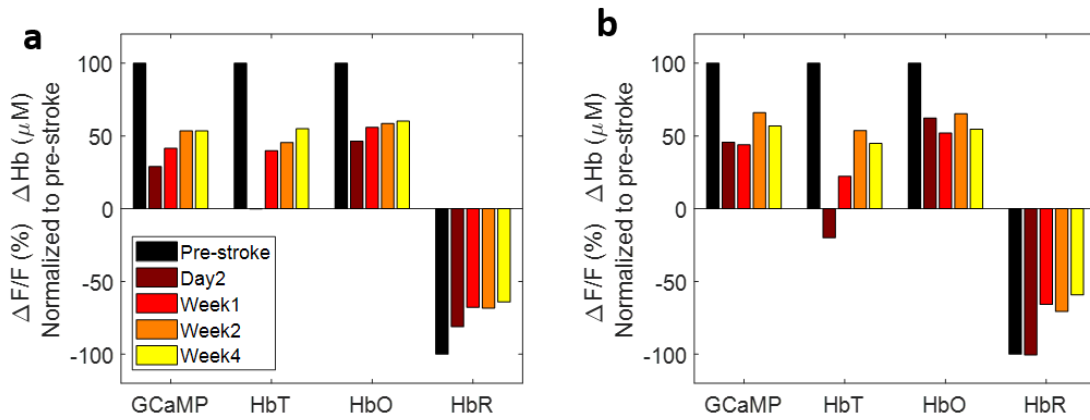


**Figure 5.9: Responses in the affected hemisphere normalized to pre-stroke**  
during stimulation of the impaired (a) and unimpaired (b) forelimb. HbT response is more sensitive to the stroke compared with HbO and HbR.

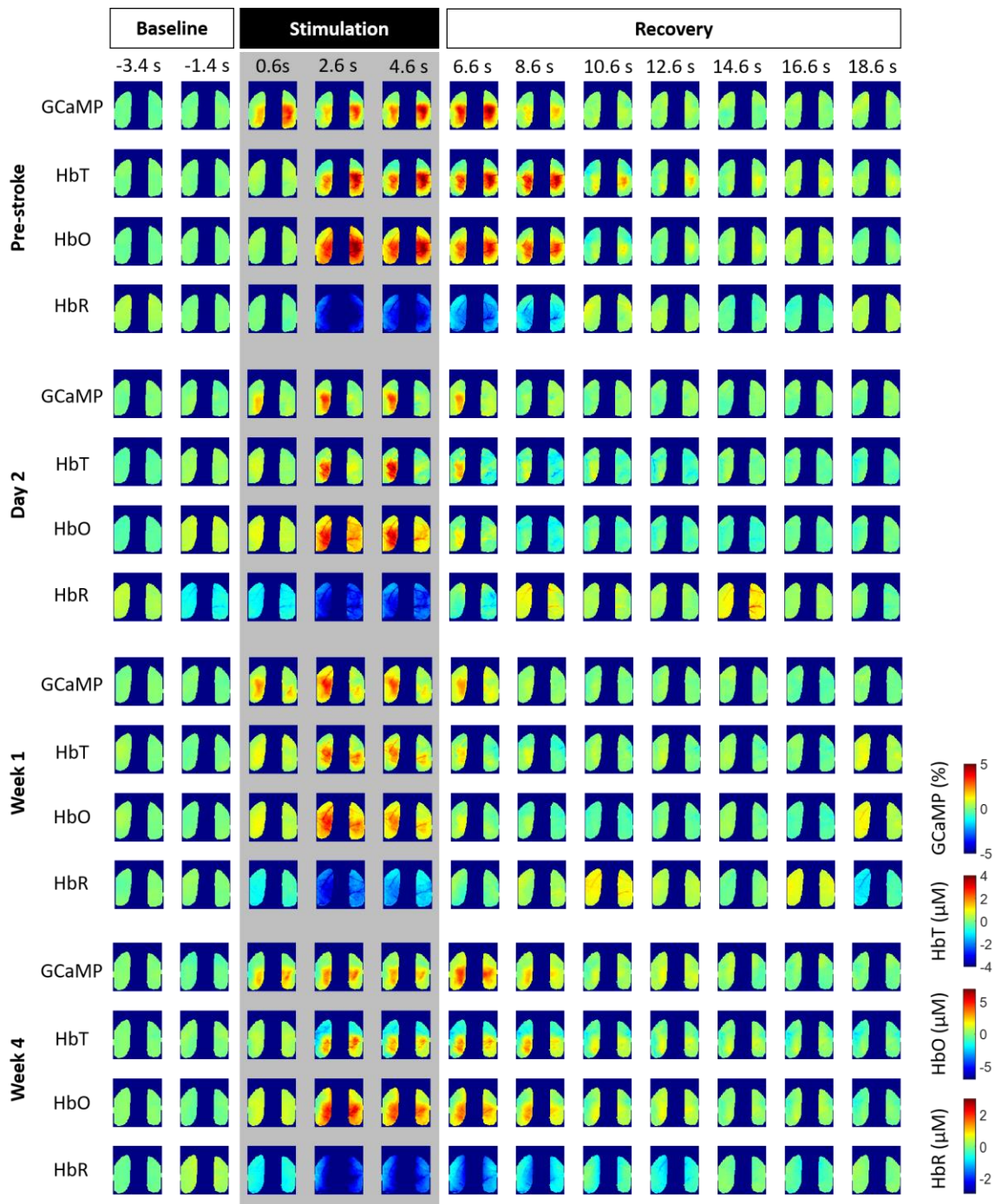


**Figure 5. 10: Spatial maps of GCaMP and hemodynamic responses over time during sensory stimulation**

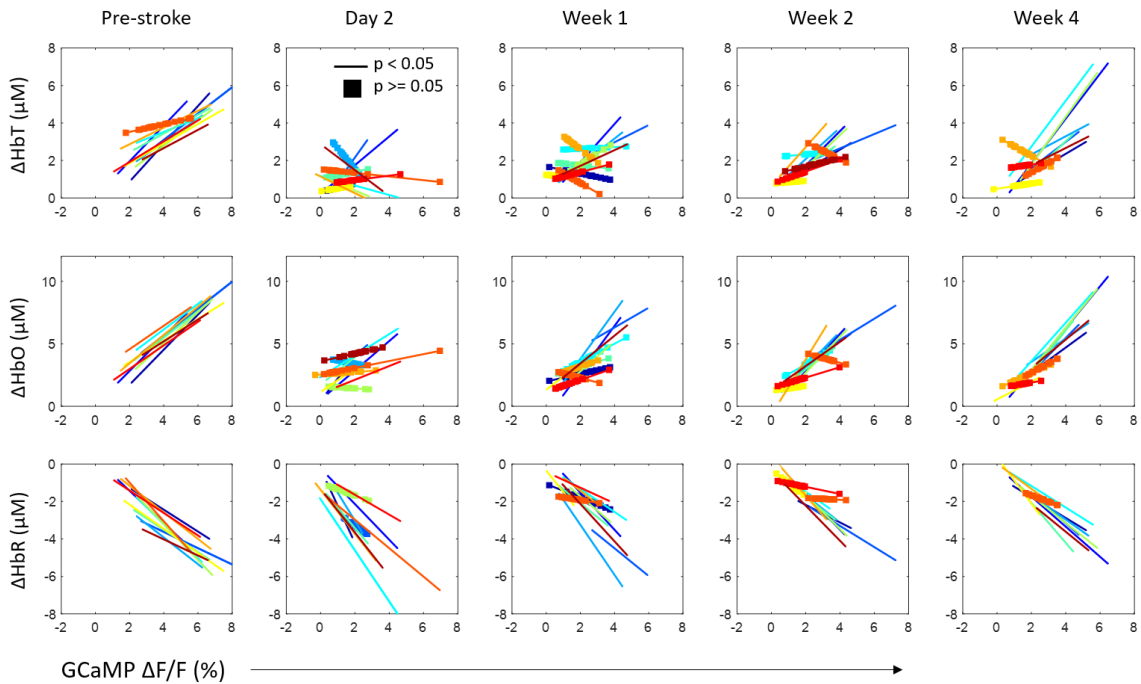


**Figure 5.11: Correlation of calcium and hemodynamic evoked responses to sensory stimulation of the affected forelimb color-coded by mouse**

Mice with significant correlation in response magnitudes of calcium and hemodynamics are shown as solid lines and mice whose responses were not correlated are shown with filled squares. Note that the animals that did not show correlation at week 4 after stroke also lacked correlation in the acute phase of stroke at week 1.

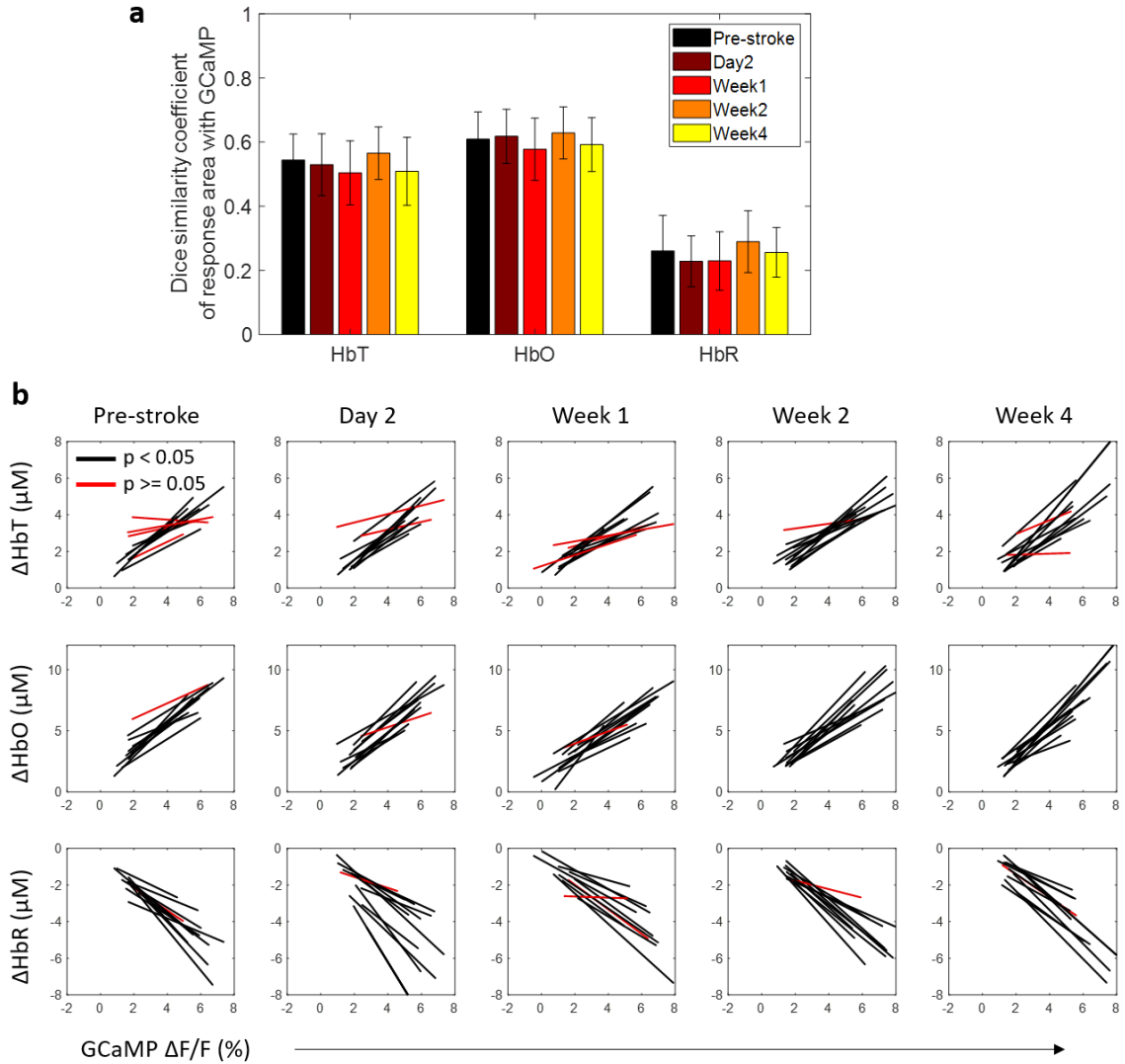


**Figure 5. 12: Responses within the unaffected hemisphere during stimulation of the unaffected forelimb**

(a) Dice similarity coefficient between GCaMP response areas with each hemodynamic measure. There was no change in similarity of response area after stroke. (b) Correlation of calcium and hemodynamic evoked responses in the unaffected forelimb to sensory stimulation of the unaffected forelimb.

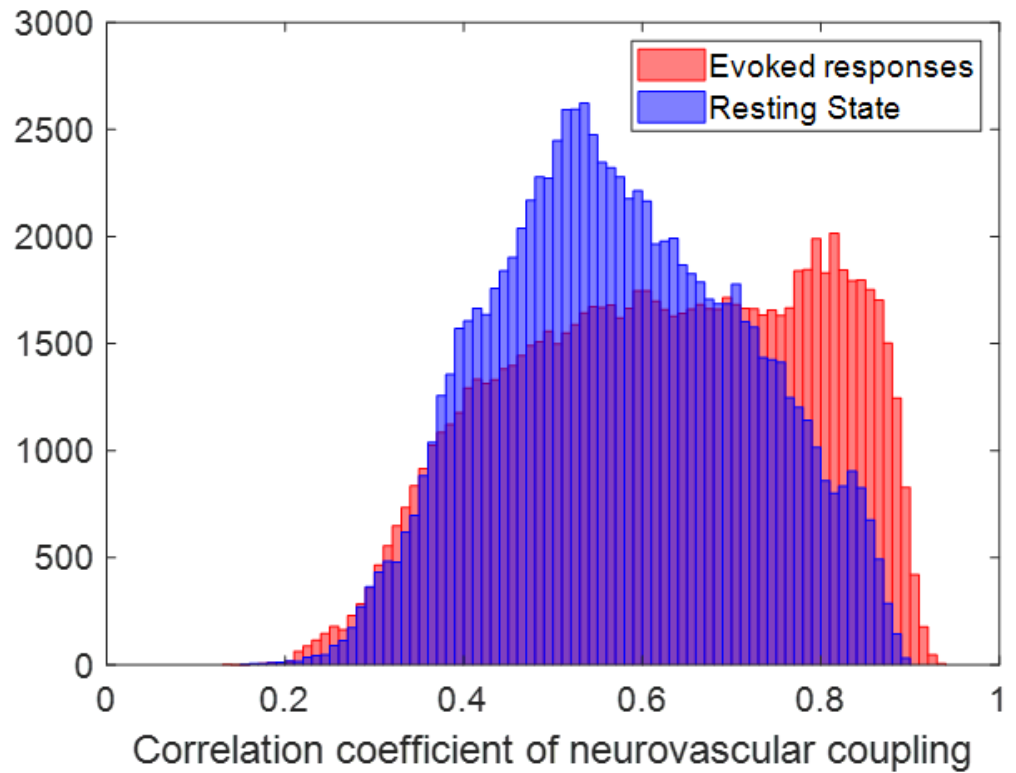


**Figure 5. 13:** Pearson's correlation coefficient of neurovascular coupling in healthy pre-stroke animals during sessions with evoked responses and resting-state sessions

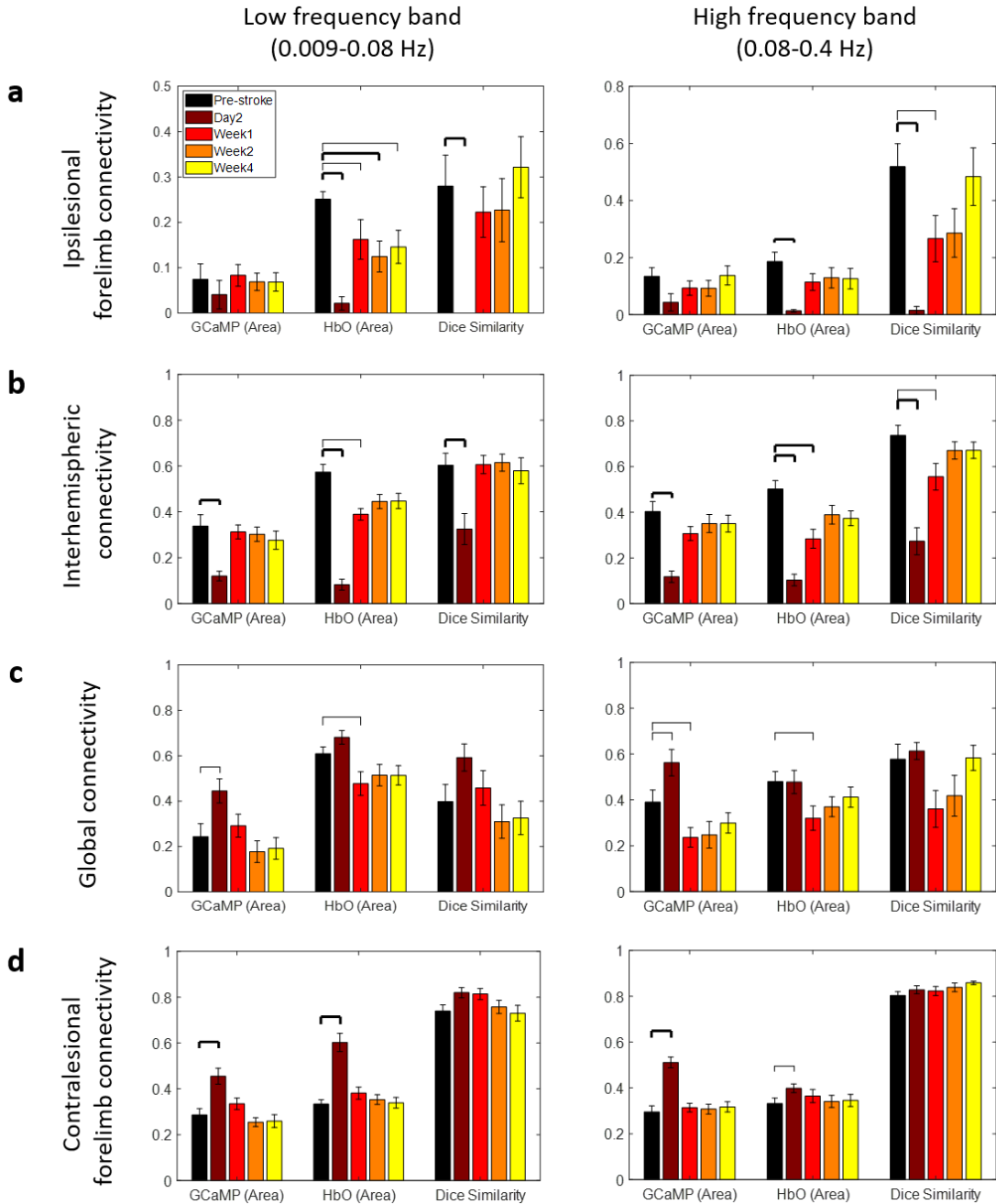


**Figure 5.14: RSFC proportional area and dice coefficient analysis at threshold of 0.4**

Each Figure shows the proportional area of GCaMP and HbO above the correlation coefficient equal to 0.4 and the dice similarity between the GCaMP and HbO at 0.4. (a) Ipsilesional forelimb homotopic connectivity, (b) Interhemispheric connectivity, (c) Global connectivity, (d) Contralateral forelimb connectivity, in the low frequency band (left) and the high frequency band (right)

## CHAPTER SIX – CONCLUSIONS AND FUTURE DIRECTIONS

### 6.1 Summary of dissertation

The work completed in this dissertation has implemented methods for longitudinally monitoring neurovascular stroke recovery and has used these methods to gain insights into the local and global neurovascular coupling alterations seen during stroke recovery. Specifically, we explore the relationships between neuronal calcium activity and hemodynamic changes on a brain-wide scale and address the implications these relationships have on the interpretation of human functional neuroimaging studies.

First, we implemented a mouse stroke model that has high clinical relevance and provides wide-field microscopic to macroscopic cortical access to study the structural and functional changes that occur during the longitudinal stroke recovery process. Pre-clinical animal models are used extensively to study stroke; however, the translational alignment of many such models to the nature of human strokes have been questioned in recent years. Specifically, the use of anesthetics during stroke induction can alter the true effect of the stroke. Additionally, the nature of the ischemic damage caused by many procedures varies in physiology and thus the consequences that result due to the stroke may not be established in a similar way to humans. To that end, we optimized a photothrombotic model in mice to induce strokes that more closely mimics the physiology of a human stroke. We perform the stroke in awake animals implanted with bilateral cranial windows and target a single vessel for occlusion, which produces structural, functional, and behavioral deficits that can be monitored longitudinally.

Next, we established wide-field optical methods for longitudinal monitoring of stroke progression and neurovascular coupling during stroke recovery. The spatial extent of the stroke core and its progression can be monitored optically by capturing changes to tissue scattering. We implemented SFDI, which obtains tissue absorption and scattering coefficients and can reliably identify the stroke core. We showed that SFDI can be used both in the acute and chronic phases of stroke to provide the spatial extent of the stroke core. The assessment of neurovascular coupling was performed by simultaneous imaging of neuronal and hemodynamic activity by combining fluorescence calcium imaging and intrinsic optical signal imaging. GCaMP was used as a marker for neuronal activity, which can be measured by capturing changes in its fluorescence activity; hemodynamic activity was monitored through changes in oxy- and deoxy-hemoglobin through multi-spectral imaging. Further, we established data processing pipelines for correcting fluorescence data for hemodynamic crosstalk. This is an essential step for removing hemodynamic confounds in the fluorescence signal and extracting accurate calcium dynamics. Additionally, changes in tissue optical properties post-stroke obtained from SFDI aided in the correction algorithm.

Finally, we assessed the progression of cortical activity following stroke and evaluated the relationships between neuronal and hemodynamic activity in the acute and chronic phases of recovery and their associations with behavioral outcomes. We looked at the effect of stroke on local cortical activity to an external stimulus as well as global changes to spontaneous activity and functional connectivity. Neuronal and hemodynamic responses to forelimb stimulation were significantly reduced in the acute phase with varied

levels of recovery in the chronic phase. The recovery of cortical responses and behavior were associated with the extent of forelimb region damaged by the stroke. Moreover, early recovery of responses within the affected forelimb was correlated with better long-term behavioral outcomes. Calcium and hemodynamic response magnitudes to sensory stimulation showed high correlation in healthy animals but lost correlation after stroke. The extent of recovery in correlation of responses was associated with better outcomes. Neurovascular coupling, assessed with the HRF and its ability to predict hemodynamics, was disrupted in the acute phase within the stroke core and the peri-infarct. The peri-infarct zone showed recoupling in the chronic phase and this recoupling was also associated with better behavioral outcomes. Stroke also had an impact on global brain oscillations. There was an increase in the power of the calcium signal specifically in the contralesional forelimb region, while hemodynamics showed a uniform increase in power across both hemispheres of the brain. The increased calcium power within the contralesional forelimb was associated with an increase in its functional connectivity assessed with RSFC. The increase in oscillatory power was transient and returned to normal in the chronic phase. Additionally, RSFC showed disruptions to forelimb homotopic connectivity and interhemispheric connectivity in the very acute phase but was largely resolved by week 1. Overall, we showed that stroke leads to neurovascular uncoupling in the acute phase and was restored in the chronic phase.

## **6.2 Significance for pre-clinical research and clinical translation**

This work has the potential to have significant impact across pre-clinical stroke research

as well as implications for human functional neuroimaging. The last decade has seen a push from the stroke research community to align pre-clinical to clinical stroke recovery to avoid the past failures in the lack of translational potential seen in therapeutic drugs<sup>82</sup>. One of the main issues is the non-physiological nature of many rodent stroke models. While photothrombosis is minimally invasive, allows longitudinal study, and can be performed in awake animals, it has been criticized for its ischemic mechanism, where all vascular elements within the region are occluded, and for its small peri-infarct zone where many biological processes associated with tissue repair occur, such as angiogenesis and neurogenesis. To overcome these disadvantages, we optimized the traditional photothrombosis protocol to occlude a single distal pial arteriole, as would be seen in humans, with minimum laser damage to the surrounding tissue, such that any resulting tissue damage would be due to the occlusion itself and not the laser. This optimization led to a larger expected peri-infarct zone where biological mechanisms associated with stroke recovery can be followed longitudinally. Other issues concerning translational potential are the time course of recovery and the biomarkers followed. We utilize chronic cranial window implants that maintain optical visibility up to six months following the implant surgery, which is sufficient to follow both the acute and chronic phases of recovery. Following the full time course of stroke recovery is essential for understanding long-term recovery mechanisms and the long-term effects of therapeutics. Additionally, the biomarkers we use for recovery include cerebral blood flow measures that are known to reflect measures obtained in functional neuroimaging studies used to follow stroke patients. Taken together, the combination of stroke model and imaging modalities used in this work

can aid in answering many open questions, regarding neural and vascular recovery mechanisms following stroke, with high clinical relevance.

Further, we use our established modalities to provide insights on the effect of stroke on neurovascular coupling, which might aid in better interpretation of functional neuroimaging studies. A big open question in stroke research is the accurate interpretation of functional neuroimaging since stroke affects the physiological parameters underlying these vascular signals, therefore complicating the interpretation of these results. We observed that the linear relationship that exists between neuronal activity and hemodynamics in healthy animals is altered after the stroke and the neurovascular coupling model is no longer able to accurately predict hemodynamics given the neuronal activity. This suggests that acute stroke leads to neurovascular uncoupling, as defined by the linear relationship, and that vascular signals obtained by functional neuroimaging might not be capturing the true underlying physiology. This opens the question as to the possibility of a non-linear relationship and the mechanisms involved in such a change. Although neurovascular coupling might be affected, which introduces uncertainty in interpretation of functional neuroimaging techniques, these methods are nonetheless valuable to monitor stroke progression. We have showed that early recovery in hemodynamic responses are indicative of improved neurovascular coupling and better behavioral outcomes regardless of underlying physiology. Therefore, neuroimaging can still be used to monitor acute recovery and gain insights on the benefits of acute therapies. Moreover, we showed that neurovascular coupling is reestablished in the chronic phase of stroke recovery, suggesting

that functional neuroimaging might be faithfully representing the underlying physiology chronically.

In addition to local neurovascular coupling alterations within the stroke affected hemisphere, we assessed changes to global brain oscillations and network connectivity. We showed that stroke leads to increases in brain oscillations in distinct patterns for neural activity compared to hemodynamics. Prior work has shown increases in neuronal excitability in the brain after stroke, especially in the contralesional homotopic region. Prior work has also shown increases in hemodynamic oscillations that suggest vasomotion as a result of hypoperfusion induced dysregulation of blood flow. However, the interaction and relationship between global neuronal and hemodynamic activity increases have not been investigated simultaneously. Further work is needed to understand the origins and implications of these phenomenon. We also assessed RSFC and found that interhemispheric connectivity is significantly impacted in the early acute phase of stroke. The trends between calcium activity and hemodynamics were similar across metrics. However, RSFC was not sensitive enough to capture the stroke at week 1 and beyond and did not show any associations with behavior. This could suggest that RSFC is less sensitive to the relatively smaller strokes produced by our photothrombosis model compared to studies where it was used to monitor stroke outcome.

### 6.3 Future directions

The work we have presented in this dissertation opens the possibility for a multitude of future directions and experiments that could address some of the questions raised. These future directions can be categorized into three main themes: 1) alignment with behavioral outcomes, 2) mechanisms involved in neurovascular uncoupling and recoupling, 3) therapeutic interventions.

The sensorimotor behavior outcome utilized in this work is the cylinder test that follows changes in forelimb use asymmetry in rodents. While this test has been used widely to follow stroke outcomes in spontaneous recovery, it also has a few disadvantages that can be improved upon. First, the test is not very sensitive to minor deficits and can overlook deficits caused by small strokes with photothrombosis. Additionally, the evaluation is performed manually, which can introduce subjective biases in the analysis. Finally, this test cannot be performed with simultaneous imaging that requires head-fixation. These drawbacks can be improved upon by designing a more sensitive sensorimotor test that can be performed while the animal is head fixed. This opens several possible questions that can be answered with regards to how behavior can shape cortical activity and reorganization or vice versa and how this can be used to improve recovery.

Another set of possible experiments is to explore the cellular mechanisms involved in neurovascular coupling. The neurovascular unit, which comprises the neurons, astrocytes, pericytes, and vasculature, are tightly coupled to regulate the metabolic demands of the brain. This work and others have shown that stroke has a significant effect

on neurovascular coupling as well as the neurovascular unit. Understanding the mechanisms of how the different compartments are affected by stroke and the role of these compartments in recovery can advance our understanding of stroke recovery. For instance, pericytes are known to have a number of essential functions that help maintain neurovascular coupling in the healthy brain. Pericytes have arbors that expand the outer surface of arterioles and express contractile proteins, which help in regulating blood flow. We hypothesize that stroke results in a loss of pericyte arborization and failure of the contractile machinery and this could be a contributing factor to neurovascular uncoupling. We further hypothesize that reestablishment of the pericyte arbors and contractile proteins aid in neurovascular recoupling. Another line of research targets the role of specific neuron types and how their activity shapes recovery. Stimulation of excitatory or inhibitory cell types might have different effects on neurovascular coupling recovery that can be addressed with our setup.

Finally, the goal of any stroke research is to eventually be used to help stroke patients regain their lost function by enhancing the stroke recovery process. Our work aligns with testing the effects of various treatments on neurovascular coupling. These treatments could be in the form of drug therapies that have specific molecular pathways they act on and promote recovery by acting on neurons, pericytes, or vessels. The time course and effect of these therapies on neurovascular coupling and outcomes can be monitored longitudinally. Treatments can also be in the form of various rehabilitative techniques. The role of early versus later rehabilitative interventions are being actively

investigated. Additionally, the involvement and use of the unimpaired hemisphere in recovery of affected hemisphere is being addressed.

Overall, in the work of this dissertation I hoped to address our understanding of neurovascular coupling not only to better interpret stroke functional neuroimaging studies but also to understand the mechanisms involved in the recovery process. Functional neuroimaging techniques such as fMRI and fNIRS have significant potential to advance our understanding of stroke recovery as well as provide insights into the benefits or disadvantages of various rehabilitative techniques that could enhance the recovery and outcomes. However, for the potential of functional neuroimaging to be fully realized, a more comprehensive understanding of neurovascular coupling is needed. I hope that this work motivates and aids in neurovascular stroke research.

## BIBLIOGRAPHY

1. Donnan, G. A. & Davis, S. M. Neuroimaging, the ischaemic penumbra, and selection of patients for acute stroke therapy. *The Lancet. Neurology.* **1**, 417–425 (2002).
2. Kidwell, C. S., Alger, J. R. & Saver, J. L. Beyond Mismatch: Evolving Paradigms in Imaging the Ischemic Penumbra With Multimodal Magnetic Resonance Imaging. *Stroke* **34**, 2729–2735 (2003).
3. Cramer, S. C. Repairing the human brain after stroke. II. Restorative therapies. *Annals of Neurology.* **63**, 549–560 (2008).
4. Cassidy, J. M. & Cramer, S. C. Spontaneous & Therapeutic-Induced Mechanisms of Functional Recovery After Stroke. *Translational Stroke Research.* **8**, 33–46 (2017).
5. Cramer, S. C. Repairing the human brain after stroke: I. Mechanisms of spontaneous recovery. *Annals of Neurology.* **63**, 272–287 (2008).
6. Calautti, C. & Baron, J. C. Functional neuroimaging studies of motor recovery after stroke in adults: A review. *Stroke* **34**, 1553–1566 (2003).
7. Johansen-berg, H. Functional imaging of stroke recovery: What have we learnt and where do we go from here? *International Journal of Stroke* **2**, 7–16 (2007).
8. Grefkes, C. & Fink, G. R. Reorganization of cerebral networks after stroke: New insights from neuroimaging with connectivity approaches. *Brain* **134**, 1264–1276 (2011).
9. Grefkes, C. & Ward, N. S. Cortical reorganization after stroke: How much and how functional? *Neuroscientist* **20**, 56–70 (2014).
10. Benjamin, E. J. *et al. Heart Disease and Stroke Statistics—2018 Update: A Report From the American Heart Association. Circulation* (2018). doi:10.1161/CIR.0000000000000558
11. Moskowitz, M. A., Lo, E. H. & Iadecola, C. The science of stroke: Mechanisms in search of treatments. *Neuron* **67**, 181–198 (2010).
12. Lo, E. H., Dalkara, T. & Moskowitz, M. A. Neurological diseases: Mechanisms, challenges and opportunities in stroke. *Nature Reviews. Neuroscience.* **4**, 399–414 (2003).

13. Iadecola, C. & Anrather, J. The immunology of stroke: From mechanisms to translation. *Nature Medicine*. **17**, 796–808 (2011).
14. Lo, E. H. A new penumbra: Transitioning from injury into repair after stroke. *Nature Medicine*. **14**, 497–500 (2008).
15. Carmichael, S. T. Plasticity of cortical projections after stroke. *Neuroscientist* **9**, 64–75 (2003).
16. Carmichael, S. T. Cellular and molecular mechanisms of neural repair after stroke: Making waves. *Annals of Neurology*. **59**, 735–742 (2006).
17. Murphy, T. H. & Corbett, D. Plasticity during stroke recovery: From synapse to behaviour. *Nature Reviews. Neuroscience*. **10**, 861–872 (2009).
18. Attwell, D. *et al.* Glial and neuronal control of brain blood flow. *Nature* **468**, 232–243 (2010).
19. Kleinfeld, D. *et al.* A guide to delineate the logic of neurovascular signaling in the brain. *Frontiers in Neuroenergetics* **3**, 1–9 (2011).
20. Buxton, R. B., Griffeth, V. E. M., Simon, A. B. & Moradi, F. Variability of the coupling of blood flow and oxygen metabolism responses in the brain: A problem for interpreting BOLD studies but potentially a new window on the underlying neural activity. *Frontiers in Neuroscience*. **8**, 1–6 (2014).
21. Cauli, B. Revisiting the role of neurons in neurovascular coupling. *Front. Neuroenergetics* **2**, 1–8 (2010).
22. Hamel, E. Perivascular nerves and the regulation of cerebrovascular tone. *Journal of Applied Physiology*. **100**, 1059–1064 (2006).
23. Lake, E. M. R., Bazzigaluppi, P. & Stefanovic, B. Functional magnetic resonance imaging in chronic ischaemic stroke. *Philosophical Transactions of the Royal Society of London. Series B, Biological Sciences*. **371**, 1–11 (2016).
24. Kunz, A. & Iadecola, C. Cerebral vascular dysregulation in the ischemic brain. *Handbook of Clinical Neurology*. **92**, 283–305 (2009).
25. Girouard, H. & Iadecola, C. Neurovascular coupling in the normal brain and in hypertension, stroke, and Alzheimer disease. *Journal of Applied Physiology*. **100(1)**, 328–335 (2012). <https://doi.org/10.1152/japplphysiol.00966.2005>
26. Marshall, R. S. *et al.* Evolution of cortical activation during recovery from corticospinal tract infarction. *Stroke* **31**, 656–661 (2000).

27. Johansen-Berg, H. *et al.* Correlation between motor improvements and altered fMRI activity after rehabilitative therapy. *Brain* **125**, 2731–2742 (2002).
28. Pineiro, R., Pendlebury, S., Johansen-Berg, H. & Matthews, P. M. Altered hemodynamic responses in patients after subcortical stroke measured by functional MRI. *Stroke* **33**, 103–109 (2002).
29. Krainik, A., Hund-Georgiadis, M., Zysset, S. & Von Cramon, D. Y. Regional impairment of cerebrovascular reactivity and BOLD signal in adults after stroke. *Stroke* **36**, 1146–1152 (2005).
30. Jones, T. A. Motor compensation and its effects on neural reorganization after stroke. *Nature Reviews. Neuroscience* **18**, 267–280 (2017).
31. Jones, T. A. & Adkins, D. L. Motor System Reorganization After Stroke: Stimulating and Training Toward Perfection. *Physiology* **30**, 358–370 (2015).
32. Calautti, C., Leroy, F., Guincestre, J. Y., Marié, R. M. & Baron, J. C. Sequential activation brain mapping after subcortical stroke: Changes in hemispheric balance and recovery. *Neuroreport* **12**, 3883–3886 (2001).
33. Rehme, A. K., Eickhoff, S. B., Wang, L. E., Fink, G. R. & Grefkes, C. Dynamic causal modeling of cortical activity from the acute to the chronic stage after stroke. *Neuroimage* **55**, 1147–1158 (2011).
34. Rehme, A. K., Eickhoff, S. B., Rottschy, C., Fink, G. R. & Grefkes, C. Activation likelihood estimation meta-analysis of motor-related neural activity after stroke. *Neuroimage* **59**, 2771–2782 (2012).
35. Tombari, D. *et al.* A longitudinal fMRI study: In recovering and then in clinically stable sub-cortical stroke patients. *Neuroimage* **23**, 827–839 (2004).
36. Calautti, C. *et al.* The neural substrates of impaired finger tapping regularity after stroke. *Neuroimage* **50**, 1–6 (2010).
37. Rabiller, G., He, J. W., Nishijima, Y., Wong, A. & Liu, J. Perturbation of brain oscillations after ischemic stroke: A potential biomarker for post-stroke function and therapy. *International Journal of Molecular Sciences*. **16**, 25605–25640 (2015).
38. Carter, A. R. *et al.* Upstream dysfunction of somatomotor functional connectivity after corticospinal damage in stroke. *Neurorehabilitation and Neural Repair* **26**, 7–19 (2012).

39. Wang, L. *et al.* Dynamic functional reorganization of the motor execution network after stroke. *Brain* **133**, 1224–1238 (2010).
40. Park, C. H. *et al.* Longitudinal changes of resting-state functional connectivity during motor recovery after stroke. *Stroke* **42**, 1357–1362 (2011).
41. Carter, A. R. *et al.* Resting interhemispheric functional magnetic resonance imaging connectivity predicts performance after stroke. *Annals of Neurology* **67**, 365–375 (2010).
42. Dijkhuizen, R. M. *et al.* Functional magnetic resonance imaging of reorganization in rat brain after stroke. *Proceedings of the National Academy of Sciences of the United States of America* **98**, 12766–71 (2001).
43. Dijkhuizen, R. M. *et al.* Correlation between brain reorganization, ischemic damage, and neurologic status after transient focal cerebral ischemia in rats: a functional magnetic resonance imaging study. *Journal of Neuroscience* **23**, 510–517 (2003).
44. Winship, I. R. & Murphy, T. H. In Vivo Calcium Imaging Reveals Functional Rewiring of Single Somatosensory Neurons after Stroke. *Journal of Neuroscience* **28**, 6592–6606 (2008).
45. Brown, C. E., Aminoltejari, K., Erb, H., Winship, I. R. & Murphy, T. H. In Vivo Voltage-Sensitive Dye Imaging in Adult Mice Reveals That Somatosensory Maps Lost to Stroke Are Replaced over Weeks by New Structural and Functional Circuits with Prolonged Modes of Activation within Both the Peri-Infarct Zone and Distant Sites. *Journal of Neuroscience* **29**, 1719–1734 (2009).
46. Kraft, A. W., Bauer, A. Q., Culver, J. P. & Lee, J. M. Sensory deprivation after focal ischemia in mice accelerates brain remapping and improves functional recovery through Arc-dependent synaptic plasticity. *Science Translational Medicine* **10**, 1–11 (2018).
47. Harrison, T. C., Silasi, G., Boyd, J. D. & Murphy, T. H. Displacement of sensory maps and disorganization of motor cortex after targeted stroke in mice. *Stroke* **44**, 2300–2306 (2013).
48. Chung, D. Y. *et al.* Subarachnoid hemorrhage leads to early and persistent functional connectivity and behavioral changes in mice. *bioRxiv* (2019). doi:10.1101/826891
49. Bauer, A. Q. *et al.* Optical imaging of disrupted functional connectivity following ischemic stroke in mice. *Neuroimage* **99**, 388–401 (2014).

50. Lauritzen, M. Reading vascular changes in brain imaging: Is dendritic calcium the key? *Nature Reviews Neuroscience*. **6**, 77–85 (2005).
51. Cauli, B. *et al.* Cortical GABA interneurons in neurovascular coupling: Relays for subcortical vasoactive pathways. *Journal of Neuroscience*. **24**, 8940–8949 (2004).
52. Petersen, C. C. H., Grinvald, A. & Sakmann, B. Spatiotemporal dynamics of sensory responses in layer 2/3 of rat barrel cortex measured in vivo by voltage-sensitive dye imaging combined with whole-cell voltage recordings and neuron reconstructions. *Journal of Neuroscience*. **23**, 1298–1309 (2003).
53. Schummers, J., Yu, H. & Sur, M. Tuned Responses of Astrocytes and Their Influence on Hemodynamic Signals in the Visual Cortex. *Science*. **320**, 1638 LP – 1643 (2008).
54. Wang, X. *et al.* Astrocytic Ca<sup>2+</sup> signaling evoked by sensory stimulation in vivo. *Nature Neuroscience*. **9**, 816–823 (2006).
55. Iadecola, C. Neurovascular regulation in the normal brain and in Alzheimer's disease. *Nature Reviews Neuroscience*. **5**, 347–360 (2004).
56. Leithner, C. *et al.* Pharmacological uncoupling of activation induced increases in CBF and CMRO<sub>2</sub>. *Journal of Cerebral Blood Flow and Metabolism*. **30**, 311–322 (2010).
57. Kitaura, H. *et al.* Roles of nitric oxide as a vasodilator in neurovascular coupling of mouse somatosensory cortex. *Neuroscience Research*. **59**, 160–171 (2007).
58. Niwa, K., Araki, E., Morham, S. G., Ross, M. E. & Iadecola, C. Cyclooxygenase-2 contributes to functional hyperemia in whisker-barrel cortex. *Journal of Neuroscience*. **20**, 763–770 (2000).
59. Logothetis, N. K., Pauls, J., Augath, M., Trinath, T. & Oeltermann, A. Neurophysiological investigation of the basis of the fMRI signal. *Nature* **412**, 150–157 (2001).
60. Olsen, T. S., Larsen, B., Herning, M., Skriver, E. B. & Lassen, N. A. Blood flow and vascular reactivity in collaterally perfused brain tissue. Evidence of an ischemic penumbra in patients with acute stroke. *Stroke* **14**, 332–341 (1983).
61. Aries, M. J. H., Elting, J. W., De Keyser, J., Kremer, B. P. H. & Vroomen, P. C. A. J. Cerebral autoregulation in stroke: A review of transcranial doppler studies. *Stroke* **41**, 2697–2704 (2010).

62. Shih, Y. Y. I. *et al.* Imaging neurovascular function and functional recovery after stroke in the rat striatum using forepaw stimulation. *Journal of Cerebral Blood Flow and Metabolism*. **34**, 1483–1492 (2014).
63. Sutherland, B. A. *et al.* Multi-modal assessment of neurovascular coupling during cerebral ischaemia and reperfusion using remote middle cerebral artery occlusion. *Journal of Cerebral Blood Flow and Metabolism*. **37**, 2494–2508 (2017).
64. Ueki, M., Linn, F. & Hossman, K. A. Functional activation of cerebral blood flow and metabolism before and after global ischemia of rat brain. *Journal of Cerebral Blood Flow and Metabolism*. **8**, 486–494 (1988).
65. Rossini, P. M. *et al.* Does cerebrovascular disease affect the coupling between neuronal activity and local haemodynamics? *Brain* **127**, 99–110 (2004).
66. Weber, R. *et al.* Early prediction of functional recovery after experimental stroke: Functional magnetic resonance imaging, electrophysiology, and behavioral testing in rats. *Journal of Neuroscience*. **28**, 1022–1029 (2008).
67. Xiong, Y., Mahmood, A. & Chopp, M. Animal models of traumatic brain injury. *Nature Reviews Neuroscience*. **14**, 128–142 (2013).
68. Bilkei-Gorzo, A. Genetic mouse models of brain ageing and Alzheimer's disease. *Pharmacology & Therapeutics*. **142**, 244–257 (2014).
69. Traystman, R. J. Animal models of focal and global cerebral ischemia. *ILAR Journal*. **44**, 85–95 (2003).
70. Chen, T. W. *et al.* Ultrasensitive fluorescent proteins for imaging neuronal activity. *Nature* **499**, 295–300 (2013).
71. Tye, K. M. & Deisseroth, K. Optogenetic investigation of neural circuits underlying brain disease in animal models. *Nature Reviews Neuroscience*. **13**, 251–266 (2012).
72. Schermelleh, L. *et al.* Super-resolution microscopy demystified. *Nature Cell Biology*. **21**, 72–84 (2019).
73. Lu, R. *et al.* Rapid mesoscale volumetric imaging of neural activity with synaptic resolution. *Nature Methods* **17**, 291–294 (2020).
74. Hillman, E. M. C. Optical brain imaging in vivo: techniques and applications from animal to man. *Journal of Biomedical Optics*. **12**, 051402 (2007).
75. Ma, Y. *et al.* Wide-field optical mapping of neural activity and brain haemodynamics: Considerations and novel approaches. *Philosophical*

- Transactions of the Royal Society of London. Series B, Biological Sciences.* **371**, (2016).
76. Sigler, A. & Murphy, T. H. In vivo 2-photon imaging of fine structure in the rodent brain: Before, during, and after stroke. *Stroke* **41**, (2010).
  77. Kazmi, S. M. S. *et al.* Three-dimensional mapping of oxygen tension in cortical arterioles before and after occlusion. *Biomedical Optics Express* **4**, 1061 (2013).
  78. Schrandt, C. J., Kazmi, S. S., Jones, T. A. & Dunn, A. K. Chronic Monitoring of Vascular Progression after Ischemic Stroke Using Multiexposure Speckle Imaging and Two-Photon Fluorescence Microscopy. *Journal of Cerebral Blood Flow and Metabolism*. **35**, 933–942 (2015).
  79. Erdener, S. E. *et al.* Dynamic capillary stalls in reperfused ischemic penumbra contribute to injury: A hyperacute role for neutrophils in persistent traffic jams. *Journal of Cerebral Blood Flow and Metabolism*. 0271678X20914179 (2020). doi:10.1177/0271678X20914179
  80. Lo, E. H. Experimental models, neurovascular mechanisms and translational issues in stroke research. *British Journal of Pharmacology*. **153**, 396–405 (2008).
  81. Zhang, Z. G. & Chopp, M. Neurorestorative therapies for stroke: underlying mechanisms and translation to the clinic. *The Lancet. Neurology*. **8**, 491–500 (2009).
  82. Corbett, D. *et al.* Enhancing the Alignment of the Preclinical and Clinical Stroke Recovery Research Pipeline: Consensus-Based Core Recommendations from the Stroke Recovery and Rehabilitation Roundtable Translational Working Group. *Neurorehabilitation and Neural Repair* **31**, 699–707 (2017).
  83. Sigler, A., Goroshkov, A. & Murphy, T. H. Hardware and methodology for targeting single brain arterioles for photothrombotic stroke on an upright microscope. *Journal of Neuroscience Methods* **170**, 35–44 (2008).
  84. Clark, T. A. *et al.* Artery targeted photothrombosis widens the vascular penumbra, instigates peri-infarct neovascularization and models forelimb impairments. *Scientific Reports*. **9**, 2323 (2019).
  85. Eger Edmond I., M. D. Isoflurane: A Review. *Anesthesiology*. **55**, 559–576 (1981).
  86. Slupe, A. M. & Kirsch, J. R. Effects of anesthesia on cerebral blood flow, metabolism, and neuroprotection. *Journal of Cerebral Blood Flow and Metabolism*. **38**, 2192—2208 (2018).

87. Kitano, H., Kirsch, J. R., Hurn, P. D. & Murphy, S. J. Inhalational anesthetics as neuroprotectants or chemical preconditioning agents in ischemic brain. *Journal of Cerebral Blood Flow and Metabolism*. **27**, 1108–1128 (2007).
88. Winship, I. R. & Murphy, T. H. Remapping the somatosensory cortex after stroke: Insight from imaging the synapse to network. *Neuroscientist* **15**, 507–524 (2009).
89. Lim, D. H., LeDue, J. M., Mohajerani, M. H. & Murphy, T. H. Optogenetic Mapping after Stroke Reveals Network-Wide Scaling of Functional Connections and Heterogeneous Recovery of the Peri-Infarct. *Journal of Neuroscience*. **34**, 16455–16466 (2014).
90. Koizumi, J., Yoshida, Y., Nakazawa, T. & Ooneda, G. Experimental studies of ischemic brain edema. *Nōsotchū (Japanese Journal of Stroke)* **8**, 1–8 (1986). <https://doi.org/10.3995/jstroke.8.1>
91. AU - Chiang, T., AU - Messing, R. O. & AU - Chou, W.-H. Mouse Model of Middle Cerebral Artery Occlusion. *JoVE: Journal of Visualized Experiments*. e2761 (2011). doi:10.3791/2761
92. Li, W., Nieman, M. & Sen Gupta, A. Ferric Chloride-induced Murine Thrombosis Models. *JoVE: Journal of Visualized Experiments*. 1–12 (2016). doi:10.3791/54479
93. Horie, N. *et al.* Mouse model of focal cerebral ischemia using endothelin-1. *Journal of Neuroscience Methods* **173**, 286–290 (2008).
94. Chen, Y. *et al.* A novel mouse model of thromboembolic stroke. *Journal of Neuroscience Methods* **256**, 203–211 (2015).
95. Watson, B. D., Dietrich, W. D., Busto, R., Wachtel, M. S. & Ginsberg, M. D. Induction of reproducible brain infarction by photochemically initiated thrombosis. *Annals of Neurology*. **17**, 497–504 (1985).
96. Sunil, S. *et al.* Awake chronic mouse model of targeted pial vessel occlusion via photothrombosis. *Neurophotonics* **7**, 1–18 (2020).
97. Carmichael, S. T. Rodent models of focal stroke: Size, mechanism, and purpose. *NeuroRX* **2**, 396–409 (2005).
98. Bacigaluppi, M., Comi, G. & Hermann, D. M. Animal models of ischemic stroke. Part two: modeling cerebral ischemia. *Open Neurology Journal*. **4**, 34–38 (2010).
99. Chiang, T., Messing, R. O. & Chou, W.-H. Mouse model of middle cerebral artery occlusion. *JoVE: Journal of Visualized Experiments*. 2761 (2011).

doi:10.3791/2761

100. McPherson, R. W., Kirsch, J. R., Tobin, J. R., Ghaly, R. F. & Traystman, R. J. Cerebral blood flow in primates is increased by isoflurane over time and is decreased by nitric oxide synthase inhibition. *Anesthesiology* **80**, 1320—1327 (1994).
101. Xie, L. A Novel Model of Transient Occlusion of the Middle Cerebral Artery in Awake Mice. *Journal of Nature and Science* **2**, 367–402 (2016).
102. Seto, A. *et al.* Induction of ischemic stroke in awake freely moving mice reveals that isoflurane anesthesia can mask the benefits of a neuroprotection therapy. *Frontiers in Neuroenergetics* **6**, 1–9 (2014).
103. Sullender, C. T. *et al.* Chronic imaging of cortical oxygen tension and blood flow after targeted vascular occlusion. *In press*.
104. Shih, A. Y. *et al.* The smallest stroke: Occlusion of one penetrating vessel leads to infarction and a cognitive deficit. *Nature Neuroscience* **16**, 55–63 (2013).
105. Balbi, M. *et al.* Targeted ischemic stroke induction and mesoscopic imaging assessment of blood flow and ischemic depolarization in awake mice. *Neurophotonics* **4**, 035001 (2017).
106. Postnov, D. D., Cheng, X., Erdener, S. E. & Boas, D. A. Choosing a laser for laser speckle contrast imaging. *Scientific Reports*. **9**, 1–6 (2019).
107. Postnov, D. D., Sosnovtseva, O. & Tuchin, V. V. Improved detectability of microcirculatory dynamics by laser speckle flowmetry. *Journal of Biophotonics* **8**, 790–794 (2015).
108. AU - Ponticorvo, A. & AU - Dunn, A. K. How to Build a Laser Speckle Contrast Imaging (LSCI) System to Monitor Blood Flow. *JoVE: Journal of Visualized Experiments*. e2004 (2010). doi:doi:10.3791/2004
109. Kim, T. H. *et al.* Long-Term Optical Access to an Estimated One Million Neurons in the Live Mouse Cortex. *Cell Reports*. **17**, 3385–3394 (2016).
110. Uhlirova, H. *et al.* Cell type specificity of neurovascular coupling in cerebral cortex. *eLife*. **5**, e14315 (2016). doi:10.7554/eLife.14315
111. Postnov, D. D., Erdener, S. E., Kilic, K. & Boas, D. A. Cardiac pulsatility mapping and vessel type identification using laser speckle contrast imaging. *Biomedical Optics Express* **9**, 6388 (2018).

112. Desjardins, M. *et al.* Awake Mouse Imaging: From Two-Photon Microscopy to Blood Oxygen–Level Dependent Functional Magnetic Resonance Imaging. *Biological Psychiatry. Cognitive Neuroscience and Neuroimagingng.* **4**(6), 533–542 (2019). doi:10.1016/j.bpsc.2018.12.002
113. Kohl, M. *et al.* Physical model for the spectroscopic analysis of cortical intrinsic optical signals. *Physics in Medicine and Biology.* **45**(12), 3749–3764 (2000). <https://doi.org/10.1088/0031-9155/45/12/317>
114. Silva, V. M., Corson, N., Elder, A. & Oberdörster, G. The rat ear vein model for investigating in vivo thrombogenicity of ultrafine particles (UFP). *Toxicological Sciences.* **85**, 983–989 (2005).
115. Labat-gest, V. & Tomasi, S. Photothrombotic Ischemia: A Minimally Invasive and Reproducible Photochemical Cortical Lesion Model for Mouse Stroke Studies. *JoVE: Journal of Visualized Experiments.* 3–8 (2013). doi:10.3791/50370
116. Schaffer, C. B. *et al.* Two-photon imaging of cortical surface microvessels reveals a robust redistribution in blood flow after vascular occlusion. *PLoS Biology.* **4**, 258–270 (2006).
117. Erdener, Ş. E. *et al.* Spatio-temporal dynamics of cerebral capillary segments with stalling red blood cells. *Journal of Cerebral Blood Flow and Metabolism.* **39**(5), 886–900 (2017). doi:10.1177/0271678X17743877
118. Schallert, T., Fleming, S. M., Leasure, J. L., Tillerson, J. L. & Bland, S. T. CNS plasticity and assessment of forelimb sensorimotor outcome in unilateral rat models of stroke, cortical ablation, parkinsonism and spinal cord injury. *Neuropharmacology* **39**, 777–787 (2000).
119. Shanina, E. V., Schallert, T., Witte, O. W. & Redecker, C. Behavioral recovery from unilateral photothrombotic infarcts of the forelimb sensorimotor cortex in rats: Role of the contralateral cortex. *Neuroscience* **139**, 1495–1506 (2006).
120. Boas, D. A. & Dunn, A. K. Laser speckle contrast imaging in biomedical optics. *Journal of Biomedical Optics.* **15**, 011109 (2010).
121. Lu, H. *et al.* Induction and imaging of photothrombotic stroke in conscious and freely moving rats. *Journal of Biomedical Optics.* **19**, 096013 (2014).
122. Shih, A. Y. *et al.* Optically induced occlusion of single blood vessels in rodent neocortex. *Cold Spring Harbor Protocols.* **2013**, 1153–1160 (2013).
123. Clarkson, A. N. *et al.* Multimodal examination of structural and functional remapping in the mouse photothrombotic stroke model. *Journal of Cerebral Blood*

- Flow and Metabolism.* **33**, 716–723 (2013).
124. Ponticorvo, A. & Dunn, A. K. Simultaneous imaging of oxygen tension and blood flow in animals using a digital micromirror device. *Optics Express* **18**, 8160 (2010).
  125. Parsons, M. W. *et al.* Diffusion- and perfusion-weighted MRI response to thrombolysis in stroke. *Annals of Neurology*. **51**, 28–37 (2002).
  126. Chalela, J. A. *et al.* Early MRI Findings in Patients Receiving Tissue Plasminogen Activator Predict Outcome: Insights into the Pathophysiology of Acute Stroke in the Thrombolysis Era. *Annals of Neurology*. **55**, 105–112 (2004).
  127. Chatterjee, S. Recombinant tissue plasminogen activator for acute ischemic stroke. *Cardiology Review*. **28**(4), (2012).
  128. Brown, C. E., Li, P., Boyd, J. D., Delaney, K. R. & Murphy, T. H. Extensive Turnover of Dendritic Spines and Vascular Remodeling in Cortical Tissues Recovering from Stroke. *Journal of Neuroscience*. **27**, 4101–4109 (2007).
  129. Dunn, A. K., Bolay, H., Moskowitz, M. A. & Boas, D. A. Dynamic Imaging of Cerebral Blood Flow Using Laser Speckle. *Journal of Cerebral Blood Flow and Metabolism*. 195–201 (2001). doi:10.1097/00004647-200103000-00002
  130. Ayata, C. *et al.* Laser Speckle Flowmetry for the Study of Cerebrovascular Physiology in Normal and Ischemic Mouse Cortex. *Journal of Cerebral Blood Flow and Metabolism*. **24**, 744–755 (2004).
  131. Wang, H., Magnain, C., Sakadžić, S., Fischl, B. & Boas, D. A. Characterizing the optical properties of human brain tissue with high numerical aperture optical coherence tomography. *Biomedical Optics Express* **8**, 5617 (2017).
  132. Tang, J., Erdener, S. E., Fu, B. & Boas, D. A. Capillary red blood cell velocimetry by phase-resolved optical coherence tomography. *Optics Letters*. **42**, 3976–3979 (2017).
  133. Tang, J. *et al.* Shear-induced diffusion of red blood cells measured with dynamic light scattering-optical coherence tomography. *Journal of Biophotonics* **11**, e201700070 (2018).
  134. Helmchen, F. & Denk, W. Deep tissue two-photon microscopy. *Nature Methods* **2**, 932–940 (2005).
  135. Blicher, J. U. *et al.* Visualization of altered neurovascular coupling in chronic stroke patients using multimodal functional MRI. *Journal of Cerebral Blood Flow*

- and Metabolism.* **32**, 2044–2054 (2012).
136. Dunn, A. K. Laser speckle contrast imaging of cerebral blood flow. *Annals of Biomedical Engineering.* **40**, 367–377 (2012).
  137. Parthasarathy, A. B., Kazmi, S. M. S. & Dunn, A. K. Quantitative imaging of ischemic stroke through thinned skull in mice with Multi Exposure Speckle Imaging. *Biomedical Optics Express* **1**, 246 (2010).
  138. Strong, A. J. *et al.* Evaluation of laser speckle flowmetry for imaging cortical perfusion in experimental stroke studies: Quantitation of perfusion and detection of peri-infarct depolarisations. *Journal of Cerebral Blood Flow and Metabolism.* **26**, 645–653 (2006).
  139. Türeyen, K., Vemuganti, R., Sailor, K. A. & Dempsey, R. J. Infarct volume quantification in mouse focal cerebral ischemia: A comparison of triphenyltetrazolium chloride and cresyl violet staining techniques. *Journal of Neuroscience Methods* **139**, 203–207 (2004).
  140. Neumann-Haefelin, T., Wenserski, F. & Siebler, M. Diffusion- and perfusion-weighted MRI. The DWI / PWI mismatch region in acute stroke. *Stroke* **30**(8), 1591–1597 (1999). <https://doi.org/10.1161/01.str.30.8.1591>
  141. Meng, X., Fisher, M., Shen, Q., Sotak, C. H. & Duong, T. Q. Characterizing the Diffusion/Perfusion Mismatch in Experimental Focal Cerebral Ischemia. *Annals of Neurology.* **55**, 207–212 (2004).
  142. Liang, D., Bhatta, S., Gerzanich, V. & Simard, J. M. Cytotoxic edema: mechanisms of pathological cell swelling. *Neurosurgical Focus* **22**, E2–E2 (2007).
  143. Somjen, G. G. Mechanisms of spreading depression and hypoxic spreading depression-like depolarization. *Physiological Reviews.* **81**, 1065–1096 (2001).
  144. Choi, W. J., Li, Y. & Wang, R. K. Monitoring acute stroke progression: Multi-parametric OCT imaging of cortical perfusion, flow, and tissue scattering in a mouse model of permanent focal ischemia. *IEEE Transactions on Medical Imaging* **38**, 1427–1437 (2019).
  145. Srinivasan, V. J. *et al.* Multiparametric, Longitudinal Optical Coherence Tomography Imaging Reveals Acute Injury and Chronic Recovery in Experimental Ischemic Stroke. *PLoS One* **8**, (2013).
  146. Cuccia, D. J., Bevilacqua, F., Durkin, A. J., Ayers, F. R. & Tromberg, B. J. Quantitation and mapping of tissue optical properties using modulated imaging. *Journal of Biomedical Optics.* **14**, 024012 (2009).

147. Gioux, S., Mazhar, A. & Cuccia, D. J. Spatial frequency domain imaging in 2019: principles, applications, and perspectives. *Journal of Biomedical Optics*. **24**, 1–18 (2019).
148. Abookasis, D. *et al.* Imaging cortical absorption, scattering, and hemodynamic response during ischemic stroke using spatially modulated near-infrared illumination. *Journal of Biomedical Optics*. **14**, 024033 (2009).
149. Applegate, M. B. *et al.* OpenSFDI: an open-source guide for constructing a spatial frequency domain imaging system. *Journal of Biomedical Optics*. **25**, 1 (2020).
150. Kim, T. H. *et al.* Long-Term Optical Access to an Estimated One Million Neurons in the Live Mouse Cortex. *Cell Reports*. **17**, 3385–3394 (2016).
151. Lin, A. J. *et al.* Visible spatial frequency domain imaging with a digital light microprojector. *Journal of Biomedical Optics*. **18**, 096007 (2013).
152. Boas, D. A., Culver, J. P., Stott, J. J. & Dunn, A. K. Three dimensional Monte Carlo code for photon migration through complex heterogeneous media including the adult human head. *Optics Express* **10**, 159 (2002).
153. Tabassum, S. *et al.* Feasibility of spatial frequency domain imaging (SFDI) for optically characterizing a preclinical oncology model. *Biomedical Optics Express* **7**, 4154 (2016).
154. Brendel, M. *et al.* Increase of TREM2 during aging of an Alzheimer's disease mouse model is paralleled by microglial activation and amyloidosis. *Frontiers in Aging Neuroscience*. **9**, 1–13 (2017).
155. Wright, P. W. *et al.* Functional connectivity structure of cortical calcium dynamics in anesthetized and awake mice. *PLoS One* **12**, 1–27 (2017).
156. Zou, K. H. *et al.* Statistical Validation of Image Segmentation Quality Based on a Spatial Overlap Index. *Academic Radiology*. **11**, 178–189 (2004).
157. Wilson, J. D., Bigelow, C. E., Calkins, D. J. & Foster, T. H. Light scattering from intact cells reports oxidative-stress-induced mitochondrial swelling. *Biophysical Journal*. **88**, 2929–2938 (2005).
158. Yao, X. C., Foust, A., Rector, D. M., Barrowes, B. & George, J. S. Cross-polarized reflected light measurement of fast optical responses associated with neural activation. *Biophysical Journal*. **88**, 4170–4177 (2005).
159. Beaulieu, C. *et al.* Longitudinal magnetic resonance imaging study of perfusion and diffusion in stroke: Evolution of lesion volume and correlation with clinical

- outcome. *Annals of Neurology*. **46**, 568–578 (1999).
160. Li, F. *et al.* Transient and permanent resolution of ischemic lesions on diffusion-weighted imaging after brief periods of focal ischemia in rats: Correlation with histopathology. *Stroke* **31**, 946–954 (2000).
  161. Ginsberg, M. D. Neuroprotection for ischemic stroke: Past, present and future. *Neuropharmacology* **55**, 363–389 (2008).
  162. Mostany, R. *et al.* Local Hemodynamics Dictate Long-Term Dendritic Plasticity in Peri-Infarct Cortex. *Journal of Neuroscience*. **30**, 14116–14126 (2010).
  163. Liu, F., Schafer, D. P. & McCullough, L. D. TTC, Fluoro-Jade B and NeuN staining confirm evolving phases of infarction induced by middle cerebral artery occlusion. *Journal of Neuroscience Methods* **179**, 1–8 (2009).
  164. Uno, H. *et al.* Detectability of ischemic lesions on diffusion-weighted imaging is biphasic after transient ischemic attack. *Journal of Stroke and Cerebrovascular Diseases*. **24**, 1059–1064 (2015).
  165. Minematsu, K., Li, L., Sotak, C. H., Davis, M. A. & Fisher, M. Reversible focal ischemic injury demonstrated by diffusion-weighted magnetic resonance imaging in rats. *Stroke* **23**, 1304–1310 (1992).
  166. Hayakawa, C. K., Karrobi, K., Pera, V., Roblyer, D. & Venugopalan, V. Optical sampling depth in the spatial frequency domain. *Journal of Biomedical Optics*. **24**, 1 (2018).
  167. Carter, A. R. *et al.* Resting interhemispheric fMRI connectivity predicts performance after stroke. *Annals of Neurology*. **67**, 365–375 (2010).  
<https://doi.org/10.1002/ana.21905>
  168. Corbetta, M. Functional connectivity and neurological recovery. *Developmental Psychobiology*. **54**, 239–253 (2012).
  169. Veldsman, M., Cumming, T. & Brodtmann, A. Beyond BOLD: Optimizing functional imaging in stroke populations. *Human Brain Mapping*. **36**, 1620–1636 (2015).
  170. Srinivasan, V. J. *et al.* Frontiers in optical imaging of cerebral blood flow and metabolism. *Journal of Cerebral Blood Flow & Metabolism*. **32**(7), 1259–1276 (2012). doi:10.1038/jcbfm.2011.195
  171. Kılıç, K. *et al.* Chronic Imaging of Mouse Brain: From Optical Systems to Functional Ultrasound. *Current Protocols in Neuroscience*. **93**, e98 (2020).

172. Ma, Y. *et al.* Resting-state hemodynamics are spatiotemporally coupled to synchronized and symmetric neural activity in excitatory neurons. *Proceedings of the National Academy of Sciences of the United States of America*. **113**, E8463–E8471 (2016).
173. Ma, Y. *et al.* Wide-field optical mapping of neural activity and brain haemodynamics: Considerations and novel approaches. *Philosophical Transactions of the Royal Society of London. B, Biological Sciences.* **371**(1705), 20150360 (2016). <https://doi.org/10.1098/rstb.2015.0360>
174. Valley, M. T. *et al.* Separation of hemodynamic signals from GCaMP fluorescence measured with wide-field imaging. *Journal of Neurophysiology*. **123**, 356–366 (2020).
175. Mayhew, J. *et al.* Spectroscopic analysis of changes in remitted illumination: The response to increased neural activity in brain. *Neuroimage* **10**, 304–326 (1999).
176. Dunn, A. K., Devor, A., Dale, A. M. & Boas, D. A. Spatial extent of oxygen metabolism and hemodynamic changes during functional activation of the rat somatosensory cortex. *Neuroimage* **27**, 279–290 (2005).
177. Dana, H. *et al.* Thy1-GCaMP6 transgenic mice for neuronal population imaging in vivo. *PLoS One* **9**, (2014).
178. Kura, S. *et al.* Intrinsic optical signal imaging of the blood volume changes is sufficient for mapping the resting state functional connectivity in the rodent cortex. *Journal of Neural Engineering*. **15**(3), 035003, (2018). <https://doi.org/10.1088/1741-2552/aaafe4>
179. Fang, Q. & Boas, D. A. Monte Carlo Simulation of Photon Migration in 3D Turbid Media Accelerated by Graphics Processing Units. *Optics Express* **17**, 20178 (2009).
180. Sunil, S. *et al.* NeuroImage : Clinical Stroke core revealed by tissue scattering using spatial frequency domain imaging. *NeuroImage. Clinical*. **29**, 102539 (2021).
181. Chen, J., Fang, Q. & Intes, X. Mesh-based Monte Carlo method in time-domain widefield fluorescence molecular tomography. *Journal of Biomedical Optics*. **17**, 1 (2012).
182. Gu, X. *et al.* Long-term optical imaging of neurovascular coupling in mouse cortex using GCaMP6f and intrinsic hemodynamic signals. *NeuroImage* **165**, 251–264 (2017).

183. Lake, E. M. R. *et al.* Simultaneous cortex-wide fluorescence Ca<sup>2+</sup> imaging and whole-brain fMRI. *Nature Methods* **17**, 1262–1271 (2020).
184. Gu, X. *et al.* Long-term optical imaging of neurovascular coupling in mouse cortex using GCaMP6f and intrinsic hemodynamic signals. *NeuroImage* **165**, 251–264 (2018).
185. Mayhew, J. *et al.* Spectroscopic analysis of neural activity in brain: Increased oxygen consumption following activation of barrel cortex. *NeuroImage* **12**, 664–675 (2000).
186. Martin, C., Martindale, J., Berwick, J. & Mayhew, J. Investigating neural-hemodynamic coupling and the hemodynamic response function in the awake rat. *NeuroImage*. **31**(1), 33–48 (2006). doi:10.1016/j.neuroimage.2006.02.021
187. Lo, E. H., Moskowitz, M. A. & Jacobs, T. P. Exciting, radical, suicidal: How brain cells die after stroke. *Stroke* **36**, 189–192 (2005).
188. Sharma, N. & Cohen, L. G. Recovery of motor function after stroke. *Developmental Psychobiology*. **54**, 254–262 (2012).
189. Moseley, M. MRI of stroke. *Imaging* **41**, 410–414 (2010).
190. Sommer, C. J. Ischemic stroke: experimental models and reality. *Acta Neuropathologica*. **133**, 245–261 (2017).
191. Wright, P. W. *et al.* Functional connectivity structure of cortical calcium dynamics in anesthetized and awake mice. *PLoS One* **12**, (2017).
192. Xie, H. *et al.* Differential effects of anesthetics on resting state functional connectivity in the mouse. *Journal of Cerebral Blood Flow and Metabolism*. **40**, 875–884 (2020).
193. Chung, D. Y. *et al.* Subarachnoid hemorrhage leads to early and persistent functional connectivity and behavioral changes in mice. *Journal of Cerebral Blood Flow and Metabolism*. **41**, 975–985 (2021).
194. Montgomery, M. K. *et al.* Glioma-Induced Alterations in Neuronal Activity and Neurovascular Coupling during Disease Progression. *Cell Reports*. **31**, 107500 (2020).
195. Winder, A. T., Echagarruga, C., Zhang, Q. & Drew, P. J. Weak correlations between hemodynamic signals and ongoing neural activity during the resting state. *Nature Neuroscience*. **20**, 1761–1769 (2017).

196. Laaksonen, K. *et al.* Alterations in Spontaneous Brain Oscillations during Stroke Recovery. *PLoS One* **8**, (2013).
197. Goltsov, A. *et al.* Bifurcation in blood oscillatory rhythms for patients with ischemic stroke: A small scale clinical trial using laser Doppler flowmetry and computational modeling of vasomotion. *Frontiers in Physiology*. **8**, 1–11 (2017).
198. Angels Font, M., Arboix, A. & Krupinski, J. Angiogenesis, Neurogenesis and Neuroplasticity in Ischemic Stroke. *Current Cardiology Reviews*. **6**, 238–244 (2010).
199. Boyd, L. A. *et al.* Biomarkers of stroke recovery: Consensus-based core recommendations from the Stroke Recovery and Rehabilitation Roundtable. *International Journal of Stroke* **12**, 480–493 (2017).
200. Stinear, C. M. Prediction of motor recovery after stroke: advances in biomarkers. *The Lancet. Neurology*. **16**, 826–836 (2017).
201. Grefkes, C. & Fink, G. R. Connectivity-based approaches in stroke and recovery of function. *The Lancet Neurology*. **13**, 206–216 (2014).
202. Huang, M. X. *et al.* Marked Increases in Resting-State MEG Gamma-Band Activity in Combat-Related Mild Traumatic Brain Injury. *Cerebral Cortex* **30**, 283–295 (2020).
203. Intaglietta, M. Arteriolar Vasomotion: Implications for Tissue Ischemia. *Blood Vessels*. **28(suppl 1)**, 1–7 (1991). <https://doi.org/10.1159/000158912>
204. Intaglietta, M. Vasomotion and flowmotion: physiological mechanisms and clinical evidence. *Vascular Medicine Review*. **1**, 101–112 (1990). <https://doi.org/10.1177%2F1358836X9000100202>
205. Carmichael, S. T. Brain excitability in stroke: The yin and yang of stroke progression. *Archives of Neurology*. **69**, 161–167 (2012).
206. Joy, M. T. & Carmichael, S. T. Encouraging an excitable brain state: mechanisms of brain repair in stroke. *Nature Reviews. Neuroscience*. **22**, 38–53 (2021).
207. Bütfisch, C. M., Netz, J., Weßling, M., Seitz, R. J. & Hömberg, V. Remote changes in cortical excitability after stroke. *Brain* **126**, 470–481 (2003).
208. Mohajerani, M. H., Aminoltejari, K. & Murphy, T. H. Targeted mini-strokes produce changes in interhemispheric sensory signal processing that are indicative of disinhibition within minutes. *Proceedings of the National Academy of Sciences of the United States of America*. **108**, E183–E191 (2011).

209. Balbi, M. *et al.* Gamma frequency activation of inhibitory neurons in the acute phase after stroke attenuates vascular and behavioral dysfunction. *Cell Reports*. **34**, 108696 (2021).
210. Adaikkan, C. *et al.* Gamma Entrainment Binds Higher-Order Brain Regions and Offers Neuroprotection. *Neuron* **102**, 929-943.e8 (2019).
211. Carmichael, S. T. & Chesselet, M. F. Synchronous neuronal activity is a signal for axonal sprouting after cortical lesions in the adult. *Journal of Neuroscience*. **22**, 6062–6070 (2002).
212. White, B. R. *et al.* Imaging of functional connectivity in the mouse brain. *PLoS One* **6**, (2011).
213. Isaacson, J. S. & Scanziani, M. How inhibition shapes cortical activity. *Neuron* **72**, 231–243 (2011).

## CURRICULUM VITAE

### **Smrithi Sunil**

Department of Biomedical Engineering

Phone: (617) 955-0635

[ssunil@bu.edu](mailto:ssunil@bu.edu)

### **Education**

#### **Boston University**

Boston, MA

PhD Candidate in Biomedical Engineering

Thesis: Wide-field optical imaging of neurovascular coupling during stroke recovery

Advisor: Dr. David Boas

#### **Boston University**

Boston, MA

M.S., Biomedical Engineering, May 2018

#### **Case Western Reserve University**

Cleveland, OH

B.S., Biomedical Engineering, May 2015

### **Research experience**

#### **Boston University**

Graduate Research Fellow, Dr. David Boas

November 2017 – Present

- Develop and implement optical systems for simultaneous monitoring of blood flow, hemodynamics, and neural activity
- Optimize and characterize an awake mouse photothrombosis stroke model
- Understand the underlying functional contributions of neural and vascular components responsible for stroke recovery

#### **Boston University**

Graduate Research Fellow, Dr. Jason Ritt

December 2015 – October 2017

- Understand the involvement of cortical sensory areas in active sensing motor outputs on short timescales
- Used a closed-loop real time feedback system that delivers optogenetic stimulation to either excitatory or inhibitory neurons in somatosensory cortex time-locked to whisker motions in order to understand active sensing mechanisms

### **Case Western Reserve University**

Undergraduate Research Assistant, Dr. Bolu Ajiboye

September 2014 – February 2015

- Performed electrophysiological recordings in humans to evaluate electric field potentials for EEGs
- Used the recorded field potentials to analyze hand grasp force applied by the patient while performing specific tasks

### **Case Western Reserve University**

Undergraduate Research Assistant, Dr. Jeffrey Capadona

March 2012 – August 2014

- Correlated neural electrode performance with the inflammatory response to intracortical microelectrodes
- Performed electrophysiological recordings in rodent models to evaluate single-spike action potentials and tissue impedance for implanted intracortical microelectrodes
- Characterized infiltrating blood derived cells in facilitating neuroinflammation using a bone marrow chimera model
- Evaluated the effects of resveratrol on reactive oxygen species in facilitating neuroinflammation at the brain-electrode interface

### **Case Western Reserve University**

Senior Design Team, Dr. Dustin Tyler

September 2011 – April 2012

- Developed an external stimulation technique to trigger swallowing for patients suffering from dysphagia
- Designed layout for sensors that were placed on the palate of the mouth

### **Publications**

- Sunil, S.\*, Zilpelwar, S.\*., Boas, D. A., Postnov, D. D. Guidelines for obtaining an absolute blood flow index with laser speckle contrast imaging. (*bioRxiv*)
- Kılıç, K., Desjardins, M., Tang, J., Thunemann, M., Sunil, S., Erdener, Ş. E., Postnov, D. D., Boas, D. A., & Devor, A. (2021). Chronic Cranial Windows for Long Term Multimodal Neurovascular Imaging in Mice. *Frontiers in Physiology*, 11.
- Sunil, S., Evren, S., Cheng, X., Kura, S., Tang, J., Jiang, J., Karrobi, K., Kılıç, K., Roblyer, D., & Boas, D. A. (2021). Stroke core revealed by tissue scattering using spatial frequency domain imaging. *NeuroImage: Clinical*, 29, 102539.
- Yang, J., Chen, I. A., Chang, S., Tang, J., Lee, B., Kılıç, K., Sunil, S., Wang, H., Varadarajan, D., Magnain, C. V, Chen, S.-C., Costantini, I., Pavone, F. S., Fischl, B., & Boas, D. A. (2020). Improving the characterization of *ex vivo* human brain optical properties using high numerical aperture optical coherence tomography by spatially constraining the confocal parameters. *Neurophotonics*, 7(4), 1–16.

- Kılıç, K., Tang, J., Erdener, S. E., Sunil, S., Giblin, J. T., Lee, B. S., Postnov, D. D., Chen, A., & Boas, D. A. (2020). Chronic Imaging of Mouse Brain: From Optical Systems to Functional Ultrasound. *Current Protocols in Neuroscience*, 93(1), e98.
- Sunil, S., Erdener, S. E., Lee, B. S., Postnov, D., Tang, J., Kura, S., Cheng, X., Chen, I. A., Boas, D. A., & Kılıç, K. (2020). Awake chronic mouse model of targeted pial vessel occlusion via photothrombosis. *Neurophotonics*, 7(1), 1–18.
- Tang, J., Erdener, S. E., Sunil, S., & Boas, D. A. (2019). Normalized field autocorrelation function-based optical coherence tomography three-dimensional angiography. *Journal of Biomedical Optics*, 24(3), 036005.
- Hermann, J. K., Lin, S., Soffer, A., Wong, C., Srivastava, V., Chang, J., Sunil, S., Sudhakar, S., Tomaszewski, W. H., Protasiewicz, G., Selkirk, S. M., Miller, R. H., & Capadona, J. R. (2018). The Role of Toll-Like Receptor 2 and 4 Innate Immunity Pathways in Intracortical Microelectrode-Induced Neuroinflammation. *Frontiers in Bioengineering and Biotechnology*, 6, 113.
- Freedman, D. S., Schroeder, J. B., Telian, G. I., Zhang, Z., Sunil, S., & Ritt, J. T. (2016). OptoZIF Drive: a 3D printed implant and assembly tool package for neural recording and optical stimulation in freely moving mice. *Journal of Neural Engineering*, 13(6), 066013.
- Ravikumar, M., Sunil, S., Black, J., Barkauskas, D. S., Haung, A. Y., Miller, R. H., Selkirk, S. M., & Capadona, J. R. (2014). The roles of blood-derived macrophages and resident microglia in the neuroinflammatory response to implanted Intracortical microelectrodes. *Biomaterials*, 35(28).
- Potter-Baker, K. A., Ravikumar, M., Burke, A. A., Meador, W. D., Householder, K. T., Buck, A. C., Sunil, S., Stewart, W. G., Anna, J. P., Tomaszewski, W. H., & Capadona, J. R. (2014). A comparison of neuroinflammation to implanted microelectrodes in rat and mouse models. *Biomaterials*, 35(22).
- Potter, K. A., Buck, A. C., Self, W. K., Callanan, M. E., Sunil, S., & Capadona, J. R. (2013). The effect of resveratrol on neurodegeneration and blood brain barrier stability surrounding intracortical microelectrodes. *Biomaterials*, 34(29).

## **Other activities**

### **Massachusetts Institute of Technology**

Catalyst Fellow  
January 2020 – Present

- An immersive program that accelerates and heightens the potential impact of biomedical research on health technology.
- Fellows collaborate with one another and with professionals in academia, healthcare, and industry to develop biomedical research projects that fulfill unmet healthcare needs.
- Spearheaded a team to explore and develop a proposal for a low-cost non-invasive hemoglobin monitor that can be deployed in low-resource settings in Africa and India to combat severe anemia and malaria.

## **Teaching experience**

### **Boston University**

Teaching Fellow, Control Systems in Biomedical Engineering

January – May 2018

- Served as Dr. Mary Dunlop's right-hand woman
- Conducted a weekly discussion section on topics covered in class and received highly positive student evaluations
- Led weekly office hours

### **Boston University**

Teaching Fellow, Control Systems in Biomedical Engineering

January – May 2017

- Conducted a weekly discussion section on topics covered in class and received highly positive student evaluations
- Helped create exams, homeworks, solutions, and grading rubrics
- Led weekly office hours

### **Case Western Reserve University**

Teaching Assistant, Biomedical Instrumentation

January – May 2015

- Assisted with the laboratory section of the biomedical instrumentation course
- Troubleshoot circuits and provided assistance to students during the lab
- Helped write protocols and solutions to the labs
- Graded lab reports for each lab section

### **Case Western Reserve University**

Teaching Assistant, Physiology and Biophysics I

August - December 2013

- Held weekly office hours for students
- Conducted review sessions before quizzes and exams
- Edited quizzes and exams for professors and graded course material

## **Professional associations and honors**

- Optical Society of America (January 2020 – Present)
- College of Engineering, Dean's Fellowship Award, Boston University
- Society for Neuroscience (May 2016 – Present)
- Outstanding Undergraduate TA Award, Biomedical Engineering Department, Case Western Reserve University (2014 Academic Year)
- Alpha Eta Mu Beta, Biomedical Engineering Honor Society (Fall 2014 – Present)
- 2014 Professional Integrity Workshop Travel Award (Biomedical Engineering Society Annual Meeting)

- Support of Undergraduate Research and Creative Endeavors Funding (May 2014 – August 2014)
- Dean's High Honors List (Spring 2012, Fall 2013)
- Biomedical Engineering Society (August 2012 – Present)

### **Presentations**

- Sunil, S., Erdener, S. E., Shah, S., Jiang, J., Boas, D. A. Wide-field optical imaging of neurovascular coupling during stroke recovery. OSA Biophotonics Congress; Oral Presentation; April 2021.
- Sunil, S., Erdener, S. E., Postnov, D., Tang, J., Kura, S., Cheng, X., Jiang, J., Kılıç, K., & Boas, D. A. Longitudinal evolution of neurovascular coupling during stroke recovery. SPIE Photonics West Conference; Oral Presentation; March 2021
- Sunil, S., Erdener, S. E., Lee, B. S., Postnov, D., Tang, J., Kura, S., Cheng, X., Kılıç, K., & Boas, D. A. The evolution of hemodynamics during stroke recovery: from early hours to subsequent weeks. OSA Biophotonics Congress; Oral Presentation; April 2020.
- Sunil, S., Erdener, S. E., Kılıç, K., Chen, I. A., Boas, D. A. Focal pial vessel occlusion via photothrombosis with simultaneous monitoring of blood flow in awake mice. SPIE Photonics West Conference; San Francisco, CA; Poster Presentation; February 2019.
- Sunil, S., Schroeder, J., Ritt, J. Phase dependent differences in excitatory and inhibitory modulation of somatosensory cortex during active touch. Society for Neuroscience Annual Conference; Washington, DC; Poster Presentation; November 2017.
- Sunil, S., Schroeder, J., Ritt, J. Active touch modulates cortical excitation and inhibition evoked by closed-loop optogenetic stimulation. Society for Neuroscience Annual Conference; San Diego, CA; Poster Presentation; November 2016.
- Sunil, S., Ravikumar, M., Black, J., Barkauskas, D., Huang, A., Miller, R., Selkirk, S., Capadona, J. The Roles of Blood-derived Macrophages and Resident Microglia in the Neuroinflammatory Response to Implanted Intracortical Microelectrodes. Biomedical Engineering Society (BMES) Annual Conference; San Antonio, TX; Poster Presentation; October 2014.
- Sunil, S., Ravikumar, M., Capadona, J. Characterization of Blood Brain Barrier Disruption at the Tissue-Electrode Interface. Biomedical Engineering Society (BMES) Annual Conference; Seattle, WA; Poster Presentation; September 2013.
- Sunil, S., Potter, K., Ravikumar, M., Householder, K., Simon, J., Capadona, J. Comparison of a rat and mouse model for evaluation of acute and chronic Neuroinflammation following device implantation in the brain. Biomedical Engineering Society (BMES) Annual Conference; Atlanta, GA; Poster Presentation; October 2012.

- Sunil, S., Potter, K., Buck, A., Self, W., Callanan, M., Capadona, J. Grape-Derived Antioxidants Prevent Neurodegeneration in the Brain after Medical Device Implantation: Application for the Development of Neuroprotective Biomimetic Polymers. PiNO, Cleveland, OH; Poster Presentation; June 2012.

ProQuest Number: 28717974

INFORMATION TO ALL USERS

The quality and completeness of this reproduction is dependent on the quality  
and completeness of the copy made available to ProQuest.



Distributed by ProQuest LLC (2021).

Copyright of the Dissertation is held by the Author unless otherwise noted.

This work may be used in accordance with the terms of the Creative Commons license  
or other rights statement, as indicated in the copyright statement or in the metadata  
associated with this work. Unless otherwise specified in the copyright statement  
or the metadata, all rights are reserved by the copyright holder.

This work is protected against unauthorized copying under Title 17,  
United States Code and other applicable copyright laws.

Microform Edition where available © ProQuest LLC. No reproduction or digitization  
of the Microform Edition is authorized without permission of ProQuest LLC.

ProQuest LLC  
789 East Eisenhower Parkway  
P.O. Box 1346  
Ann Arbor, MI 48106 - 1346 USA